NUMERICAL STUDY OF PROJECTILE SHAPE EFFECT ON THE BUMPER PERFORMANCE UNDER HYPERVELOCITY IMPACT

By

Patrick Domingo

A Thesis submitted to the Faculty of Graduate Studies of

The University of Manitoba

in partial fulfilment of the requirements of the degree of

MASTER OF SCIENCE

Department of Mechanical Engineering

University of Manitoba

Winnipeg

Abstract

Impacts in orbit from small micrometeoroids and small non-trackable orbital debris are generally unavoidable and pose a threat to spacecraft due to the high collision speeds exceeding 7 km/s. The design of spacecraft protection against micrometeoroids and orbital debris (MMOD) is generally based on experiments and models involving spherical projectiles. However, observations of collision fragments from ground-based satellite impact experiments have shown that orbital debris are non-spherical in shape. To adjust spacecraft protection to accommodate non-spherical projectiles, a relationship between spherical projectiles and their threat-equivalent non-spherical projectiles was established.

The threat-equivalent relationship was found through a numerical methodology developed to quantitatively compare the ability of spheres and cylinders with varying length-to-diameter ratios to cause failure in a rear wall behind the bumper, referred to as the projectile threat. The study employed the smoothed-particle hydrodynamics method and explicit finite element method in commercial software ANSYS Autodyn to simulate the hypervelocity impact at 7km/s of differently shaped projectiles on to an all-aluminum bumper and rear-wall configuration. The craters produced by the debris cloud of spheres and cylinders of various geometries were compared and used to establish relationships between the threat posed by each projectile. The study found that the threat posed by cylindrical projectiles was significantly influenced by the projectile geometry, with an increase in threat observed as the cylinder length-to-diameter (L/D) ratio was reduced below or increased beyond L/D=1. Furthermore, the threat of the projectile was found to significantly depend on the thickness of the bumper and the standoff distance between the shielding and the protected surface.

The established projectile threat relationship can be applied to assess the ability of the existing MMOD bumpers to withstand cylindrical projectiles by representing them with an equivalent sphere. This approach can help reduce uncertainty and improve the safety of spacecraft when dealing with non-spherical projectiles. Furthermore, the methodology developed in this study can be utilized to establish threat relationships between projectiles under different conditions, such as irregular shapes or different impact angles.

Acknowledgements

I want to give special thanks to Dr. Igor Telichev for providing me with his advice, experience, and his patience. Thanks to my colleagues in the ORDER group for the valuable discussions, especially Victor Babarinde for his help. Thank you to Dr. Anton Kuznetcov for his mentorship prior to the program.

Lastly, I want to thank my family for their perseverance through the various crises these past few years.

Table of Contents

List of Tables

Table of Figures

List of Acronyms

BLE – Ballistic limit equation

CD – Crater depth

FEM – Finite element method

FE – Finite elements

HVI – Hypervelocity impact

ISS – International space station

LEO – Low earth orbit

MMOD – Micrometeoroid and Orbital Debris

MSS – Multi-shock shield

RP – Rear plates

SPH – Smoothed-particle hydrodynamics

SWS – Stuffed Whipple shield

WS – Whipple shield

1. Introduction

1.1. Background

This section provides preliminary information regarding the state of micrometeroids and orbital debris, their danger to spacecraft, future projections on the increase in the danger, and a brief description on the limitation of the protection against such dangers. The information provided served as the motivation for the thesis.

1.1.1 Danger to spacecraft

Spacecraft in orbit around Earth, including satellites and the International Space Station (ISS), provide many uses to daily life. Some examples of these uses are communications, scientific research, or weather forecasting. However, these spacecraft are at risk of collisions with “space junk” or orbital debris. Orbital debris are a fast growing concern for the safety and reliability of space-based infrastructure that is expected to only be a larger issue in the future.

Orbital debris are waste or dysfunctional objects that orbit around Earth that are pieces of artificial man-made objects such as old rocket stages, satellites, or solid rocket exhaust. These debris orbit at high speeds averaging 9 km/s [1]. At these speeds, even particles smaller than 1 cm can damage or destroy spacecraft. For example, in 1983, a piece of hardened paint of approximately 0.2 mm impacted a window during the STS-7 NASA mission. This small piece of paint was able to produce a crater on the window 0.4 mm deep, which rendered the window unusable and had to be replaced [1]. Greater damage and even catastrophic failures are possible with larger sizes of debris. For example, an aluminum sphere of 1cm at the average hypervelocity speeds of debris contains a similar amount of energy as a hand-grenade, which is sufficient to cause catastrophic damage to unprotected spacecraft [2].

Over one million non-trackable space debris objects with a diameter larger than 1 cm are estimated to be in orbit and many millions more for smaller debris [3]. Currently, only debris with a characteristic size of 10cm or greater can be monitored and tracked reliably. The number of these objects are shown in Figure 1. Debris collisions in orbit, whether between debris and spacecraft or between debris, increases the number of debris therefore the risk to spacecraft can increase exponentially over time. The Fengyun-1C collision event in January 2007, indicated with a "1" in Figure 1, shows the potential for collisions to produce significant debris pollution of the orbital environment. The intentional collision was caused by an anti-satellite ballistic missile impacting Fengyun-1C satellite, which produced over 3000 trackable fragments greater than 10 cm and an estimated additional 150,000 debris larger than 1 cm [4] [5]. An additional complication in the mitigation of space debris is the tendency of the debris to disperse and change its orbits. Concentrated regions of debris can be actively avoided by spacecraft, but the dispersion of the orbits make this procedure more difficult to do and eventually risk of debris has to be evaluated from a probabilistic point of view [6].

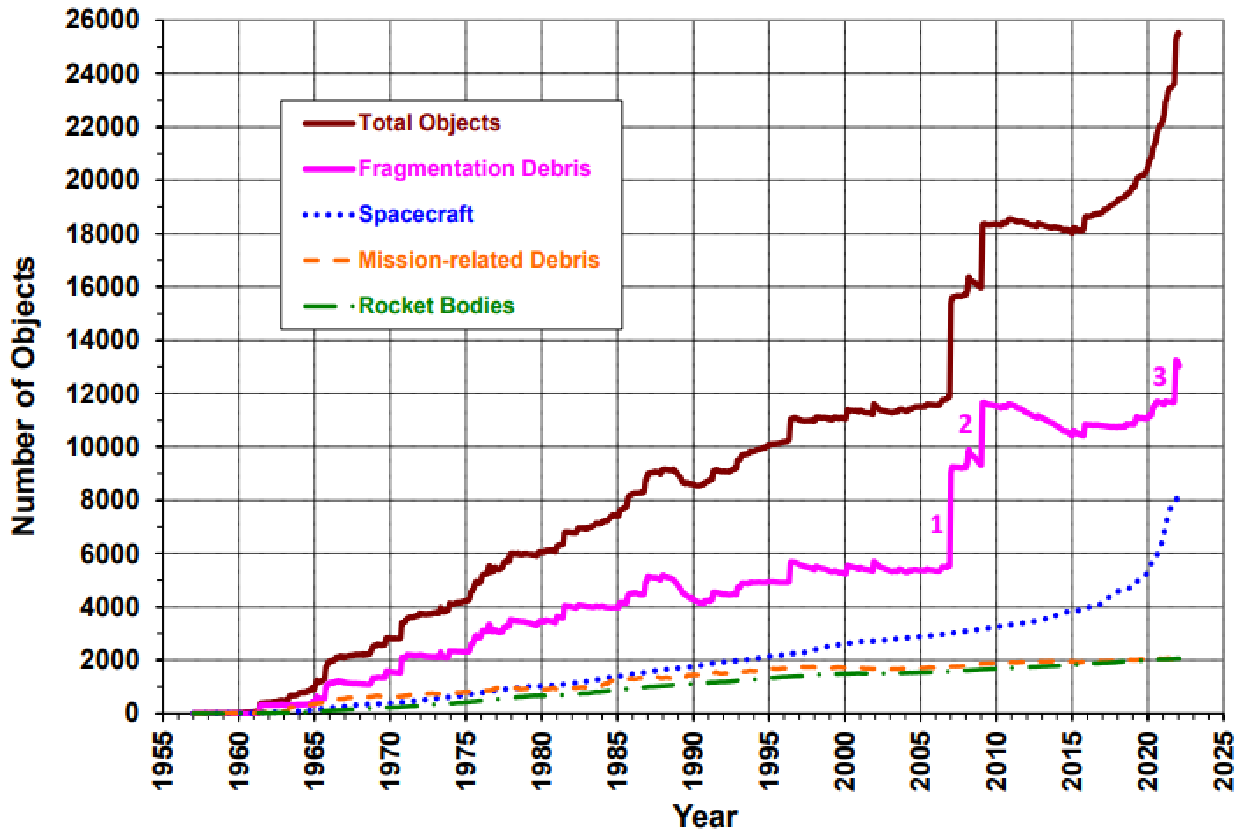

Figure 1. Growth of trackable debris greater than 10 cm [7]. Image from NASA.

One simulation performed by Liou et al. in [8] studied the growth of trackable debris in Low-Earth-Orbit (LEO) over the next 200 years based on empirical data. The study assumed a "no new launches" situation, which is an unrealistically optimistic situation where there would be no additions to existing debris. The results showed that, due to collisions between existing trackable debris, the total number of debris would continue to grow rapidly over the next 200 years and possibly more. Since the “no new launches” situation is unrealistic, the growth of the debris may eventually become unmanageable, making certain altitudes unsafe for spacecraft [2]. Other MMOD models have also confirmed that the current orbital debris environment has already passed the “tipping point,” where the current population is sufficiently large to continue to grow without further man-made contributions [4].

1.1.2 Types of debris

The man-made debris consist of artificial objects that were either released into orbit during space missions (intentionally or accidentally) or as a result of fragmentation of objects due to collisions or explosions, called breakup debris. Breakup debris, such as those caused by the Fengyun-1C collision constitute almost half of the total population as of 2008. In addition to man-made debris, collision threats to spacecraft also include naturally occurring small meteoroids or micrometeoroids. These micrometeoroids have velocities ranging from 11 km/s to 72 km/s, averaging at approximately 20km/s [1]. These velocities are much higher than for orbital debris but micrometeoroids are generally lower in density at approximately 1 g/cm^3, while orbital debris are generally assumed to be made of aluminum (2.8 g/cm^3). The combination of man-made and small natural debris is hereafter referred to as micrometeoroid and orbital debris (MMOD).

In the early years of space missions, the risks of micrometeoroids were considerably larger than for debris. However, as predicted by Kessler and Cour-Palais in 1977, the risks from man-made debris in LEO are now more significant [2] [9]. However, beyond LEO and especially beyond geosynchronous equatorial orbit (GEO 35,786 km altitude), micrometeoroids are the dominant source of risk to spacecraft.

The USA Department of Defense tracks debris in LEO greater than 5 cm using the U.S. Space Surveillance Network (SSN), which consists of a world-wide system of radar and optical sensors. For smaller sizes, NASA uses the Haystack, Haystack Auxiliary (HAX) and Goldstone radars to track debris as small as characteristic size of about 2mm at altitudes of the International Space

Station of approximately 400km [1] [4]. Generally, the smaller the fragment, the more difficult they are to track.

The size of tracked objects is estimated using "characteristic length," which is an average of the maximum length on three axes: length, width, and thickness. One area of uncertainty in the measurement of orbital debris is the characterization of shape of all tracked objects. According to an assessment to NASA's MMOD programs in 2011, there are insufficient studies involving the inclusion of debris shape into existing environmental debris models [4]. The lack of shape data and the use of single parameter "characteristic length" is problematic because these values are translated into same-diameter spheres during hypervelocity impact (HVI) testing. Furthermore, determining debris shapes are significant because different shapes are known to produce differing impact behaviour [10] [11].

1.1.3 MMOD Protection

The development and design of spacecraft shielding is based on the results from experimental HVI tests. The experimental HVI tests attempt to replicate the conditions of the space debris impact and gauge the specifications of the shielding necessary to prevent perforation of a particular size projectile. The HVI tests are costly, therefore, there are limitations on the number of and the manner in which the experiments can be performed. One such limitation is the use of spherical projectiles to represent the space debris impacting the shielding, which correspond to the characteristic size. The use of spherical projectiles provide uniformity between different experiments since accounting for other shapes is not practical due to the limited number of tests that can be run. However, the majority of space debris are not spherical [9]. Therefore, there is a disconnect between the conditions of experiments used for shielding design and the real conditions in Earth's orbit. However, this disconnect does not invalidate the many years of results of spherical HVI testing. Instead, there need only be a method to relate previous spherical results with non-spherical expectations.

1.2 Problem Statement

From the background provided in the previous section, the motivation of the thesis are summarized with the following points:

- MMOD are a persistent problem that will be present for the foreseeable future. There is a significant potential for the danger to increasingly worsen.
- A single parameter is used to describe size and shape of MMOD – the characteristic size. There is significant uncertainty in the shapes of MMOD in orbit.
- Protection of spacecraft are mainly based on experiment spheres, which are themselves based on characteristic size.
- There is a need to quantify and evaluate the effect of non-spherical MMOD on existing spacecraft protection.

1.3 Objective of Thesis

Based on the points outlined in the problem statement, the objective of thesis is to:

- Investigate the effect of non-spherical projectiles on HVI spacecraft protection, and
- develop a methodology to evaluate the threat of non-spherical projectiles on spacecraft protection.

1.4 Overview of Thesis

Section 1 (this section), provides a brief background into the state of orbital debris situation and serves as the motivation for the thesis and its objective. Section 2 includes information regarding the fundamentals of the physics of the hypervelocity impact and spacecraft shielding, as well as information about the literature involved with previous studies regarding MMOD and their shape. The following section 3 describes the methodology of the thesis work, describing how the information from the literature review was used to develop the numerical approach to reach thesis objectives. Section 4 includes the details of the material model used in the numerical models as well as the validation of the debris clouds produced in HVI. The following section 5 describes the development and the results of the crater depth numerical model, used to evaluate the threat of non-spherical MMOD. Section 6 describes the study performed on the effect of bumper thickness into the threat of the projectile, which was then used to improve the results of the crater depth model. Section 7 describes an alternative numerical model that was used for preliminary investigation into the evaluation of projectile threat. Lastly, section 8 summarizes the conclusions of the thesis.

2. **Literature Review**

This section provides information regarding the fundamental physics of HVI, the protection against MMOD, the characteristics of debris, and the effect of projectile shape in HVI.

2.1 Hypervelocity Impact

A projectile impacting a target at low velocities result in deformation governed by elastic behaviour. As the impact speed is increases, plastic behaviour can result in impact craters. As speed is increased beyond approximately 50 m/s, called the ballistic region, the main focus of study is generally the area two to three times projectile diameter around the impact location. As the impact velocity increases further than the ballistic region, eventually the stresses may exceed the strength of the projectile and cause the some breaking-up of the projectile or target. At much higher speeds above 3km/s, called hypervelocity, the stress waves generated are at least an order of magnitude above material limits and cause complete disintegration of the projectile and/or the local impact region of the target.

If the target of HVI has finite thickness, the stress waves are reflected by the free surfaces changing compressive waves into tensile waves. This phenomenon is illustrated in Figure 2, where the red and blue lines indicate the compression and rarefaction (tensile) waves, respectively. The superposition of the various stress waves can exceed local material limits and cause breaking and fragmentation in the target body. The early stages of impact behave in a fluid-like manner due to the high strain rates. In the hypervelocity range of 3 km/s to 7 km/s, the energy involved causes partial melting of the material in addition to the fragmentation. Beyond 7 km/s, there is generally enough energy in the impact for full fragmentation of the projectile and causes melting or vaporization of the material [1].

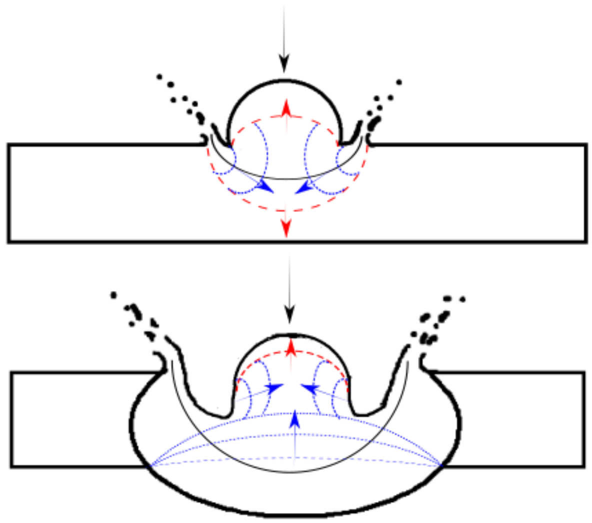

Figure 2. Visualization of HVI of spherical projectile onto flat target with finite thickness [12].

If the target body is sufficiently thin, the projectile in HVI can push through the thickness of the target, which is called perforation. The HVI process can also cause spallation, which is the detachment or ejection of material away from the target body. In a situation in which a projectile does not perforate a target of finite thickness, spallation can show as a detachment of material on the surface opposite of the impact.

Study of HVI is commonly performed with the goal of determining a particular body's ability to resist perforation through or penetration into the thickness of the body. Generally, empirical methods are used to describe hypervelocity impact behaviour. This is because the approach of analyzing HVI with analytical methods as is performed in low velocity impact is impractical for HVI.

2.2 HVI on Semi-infinitely Thick Wall

The effect of HVI on the target body depends on several factors. One primary factor is the thickness of the target body. When the thickness of the target is sufficiently large, the area of interest can be limited to the craters produced in the local region at the point of impact. At this point, the target is considered semi-infinitely thick and any HVI effects sufficiently far from the crater is negligible. There is considerable amount of study on the projectile and the crater produced on a semi-infinite plate after HVI. Of primary interest in these studies is the depth of the crater produced, which can give insight in the amount of projectile penetration in walls with finite thicknesses, limited by practical considerations.

The impact crater on semi-infinite bodies can change shape depending on the shape of the projectile. One of the significant results from tests involving the preliminary investigation of projectile shape is the increased penetrative ability of the elongated cylinder or “rod” projectile [2]. Due to the significance of rods, Tate developed a model based on a modified Bernoulli’s equations to estimate the depth of penetration onto semi-infinite targets [13]. One of the primary variables was the shape of the projectile, characterized by the length and diameter. These models were found to be in good agreement with experimental data. Generally, the penetration of the projectile increased as the projectile became more elongated, which was represented with increased length-to-diameter ratio [14].

A limitation of the Tate penetration models developed was that they were limited to velocities less than approximately 2 km/s. Modifications of the model and additional experiments extended the application of the model to approximately below 4 km/s. However, these velocities are still less than the expected velocities of orbital debris that average 9 km/s or micrometeoroids that average 20 km/s. For spacecraft, the direct applicability of such models is reduced further due to difficulties in achieving semi-infinite thickness in a practical environment. Advancements in spacecraft protection that account for thickness limitations are described later in section 2.4

2.3 Spacecraft HVI Protection Approach

To protect spacecraft against MMOD, there are three main approaches:

1. Passive: protection applied before launch;
2. Active: protective measured employed in orbit;
3. Operational: protection as a result of spacecraft arrangement and setup [4].

Collisions with small debris that are non-trackable cannot be avoided therefore spacecraft are implemented with protective shielding. This shielding is a type of passive MMOD protection. These shields mitigate the risk of damage onto the spacecraft but the requirements on the effectiveness of protective shielding increase with the growing risk of debris collisions. Each shielding configuration has a maximum size of debris called critical projectile diameter, d_c, that the shield can prevent failure from. To account for increasing debris threat, the shield effectiveness can be increased by increasing d_c.

Due to size and mass constraints of current spacecraft, it is not yet possible to use shields to protect against all debris sizes or to completely eliminate risk (0% probability of penetration) from MMOD. However, larger size debris can be mitigated using other active protection means such as collision warning and avoidance.

The risk level or reliability for the MMOD shielding is usually expressed in terms of the "probability of no penetration," shortened as PNP. Alternatively, risk of penetration or failure can also be expressed as $1 - PNP$. For example, the ISS has a minimum requirement of $PNP = 0.76$ over 10 years for shields of certain components [15]. The probability of no penetration is calculated using:

$$PNP = e^{-N} \quad \text{[Equation 1]}$$

and,

$$N = \sum_{i=1}^{n} (FAt)_i \quad \text{[Equation 2].}$$

N is the number of impacts that may cause failure and is the sum for each region i over all regions n of the spacecraft. The flux, F, is the number of debris of a particular size passing through area A over a set amount of time t.

For the International Space Station, shielding is a much more important requirement because it is a manned and long-lasting spacecraft. Additional risk measure of "Probability of no catastrophic failure" (PNCF) is required. ISS modules must comply with a PNCF≥0.95. The "R-factor" is the ratio of number of catastrophic debris impacts to number of non-catastrophic penetrating impacts [15]. PNCF is calculated using:

$$PNCF = PNP^{R} \quad \text{[Equation 3]}$$

With the increasing debris population, requirements in effectiveness of protective shielding also increase. Depending on the specifics of the mission or requirements of spacecraft, the increased effectiveness of the shielding can be either: to increase the minimum debris size for a specific PNP or to increase weight-efficiency at the same level of debris size protection [16].

2.4 Spacecraft Shielding

Monolithic walls are the simplest form of protection against MMO, however, due to practical considerations such as weight and size, other shielding designs were implemented. As described in the previous section 2.3, passive protection can only protect against MMOD up to a certain size, specific to the protective system employed. The shielding is considered to have failed if a projectile has perforated through into the critical region of the spacecraft, or if enough damage has been done to cause the primary wall spallation.

2.4.1 Whipple shield

One of the first spacecraft shielding designs proposed and developed was the Whipple Shield (WS). Created in the 1940s, the WS consists of placing a thin sacrificial plate, called "bumper," at a particular standoff distance from the rear critical or outer-most wall of the spacecraft. The WS is an example of single-function shielding, where the components of the shield serve only to provide MMOD protection. Other multi-functional shielding is described in Appendix section 10.

A schematic of the WS and the behaviour of an impacting projectile is shown in Figure 3. The purpose of the bumper is to cause fragmentation of the projectile into a "debris cloud" of much smaller particles. The standoff distance allows the cloud to disperse the kinetic energy over a larger area. Additionally, the lateral movement of the cloud provides time-delays in the arrival of the different cloud fragments [2]. The larger distribution in area, the smaller fragments, and the time-delayed nature of the fragments all contribute to the reduction in damage to the rear wall. Depending on the velocity, kinetic energy, pressure, and temperature, the debris cloud that consists of projectile and bumper particles may melt or vaporize, which further reduces the impact damage to the rear wall. The shielding is designed to stop only a specific maximum size of space debris and has a limited lifetime since the accumulation of debris collisions will eventually render the shielding ineffective. The right side of Figure 3 shows the debris cloud not perforating into the rear wall but providing sufficiently strong stress waves to create spallation.

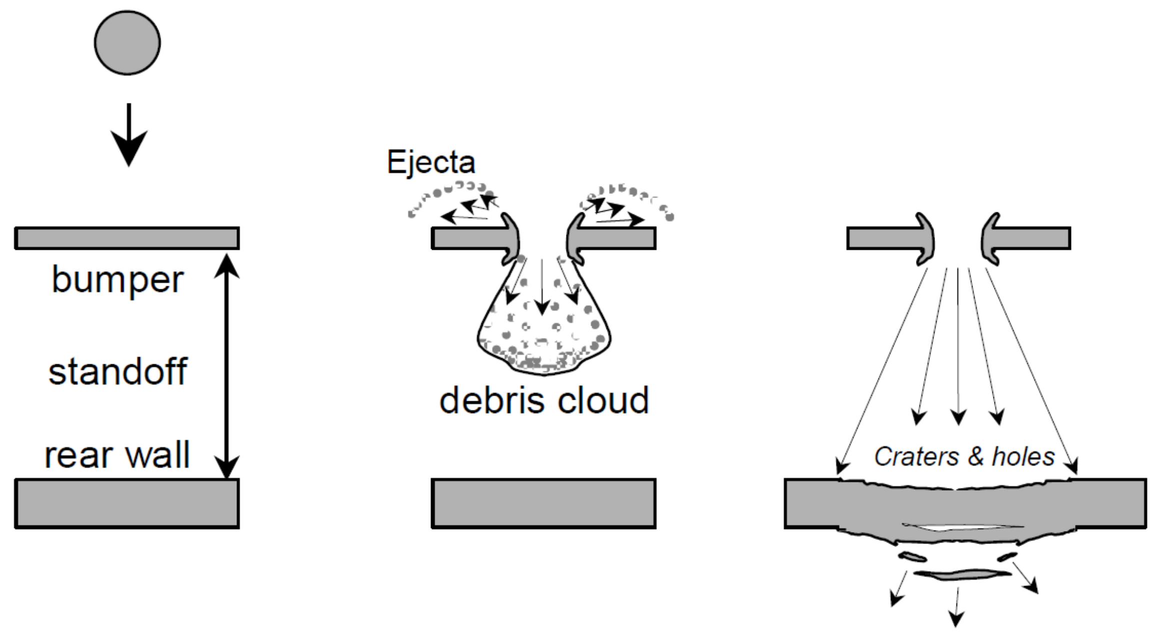

Figure 3. (Left) Basic Whipple shield; (middle) projectile penetration into bumper; (right) spallation in rear wall [1]. Image from NASA.

HVI tests and numerical modelling allows for creation of design equations for the shielding. These design equations can be used to determine minimum wall thicknesses for a given standoff. As an example, for the basic WS, the minimum required bumper thickness t_b and rear wall thickness t_w are found from:

$$t_b = \frac{c_b d \rho_p}{\rho_b} \quad \text{[Equation 4], and}$$

$$t_w = c_w d^{0.5} M^{\frac{1}{3}} (\rho_p \rho_b)^{\frac{1}{6}} \rho_w^{-1} (V cos(\theta)) S^{-\frac{3}{4}} \sigma_h'^{-\frac{1}{2}} \quad \text{[Equation 5] [1].}$$

The parameters to the empirical equations are provided in Table 1. For a given projectile of known material moving at a known speed, the minimum size of the two components of the WS can be estimated using Equation 4 and Equation 5.

Table 1. Whipple shield size equation parameters [1].

c_b	Bumper sizing equation coefficient (unitless)
c_w	Rear wall sizing equation coefficient ($cm^{-\frac{1}{3}}\sec g^{\frac{1}{3}}\ km^{-1}$)
d	Projectile diameter, cm
ρ_b	Bumper density, g/cm^3
ρ_p	Projectile density, g/cm^3
ρ_w	Rear wall density, g/cm^3
M	Projectile mass, g
S	Standoff spacing, cm
σ	Rear wall yield stress, ksi
σ'	Normalized rear wall yield strength (unitless)
θ	Impact angle, deg
V	Impact velocity, km/s

2.4.2 Ballistic limit equations

Ballistic limit equations (BLE) provide the projectile size threshold that determines failure of a particular shielding configuration. The BLE is determined through HVI testing and numerical modelling. These equations provide a convenient measure of the effectiveness of different shields. The BLE is a function of geometry, material properties, velocities, angle of impact, and the criteria or definition for failure.

Currently, experimental methods used to accelerate projectiles to hypervelocity speeds are insufficient to perform routine HVI tests at the average debris speeds (9-10km/s). For example, one of the most common and reliable accelerators is the light-gas gun (LGG), which can generally send a 2 grams of aluminum to approximately 7km/s [2]. While the more advanced LGG systems can achieve speeds of up to 10 km/s, these systems are generally not used on a regular basis for spacecraft shielding testing due to the high cost and complexity of the equipment involved. In characterizing effectiveness of shields with BLE, speeds above the limits of experimental methods have to be determined through modelling.

Comparison of the BLE developed for the WS with the BLE for a single monolithic wall of equivalent mass shows the significant protection improvement the WS offers. The comparison is displayed in Figure 4, where t_s is the thickness of the bumper. Projectile diameters above the curve for a particular projectile velocity will cause failure in the rear wall; no failure occurs for diameters below the BLE curve. Figure 4 also displays the importance and influence of the bumper thickness in shielding effectiveness. At low velocities (v < 3 km/s), the WS more closely resembles the monolithic shield because the projectile is poorly fragmented by the bumper. Between 3km/s and 7km/s, increased fragmentation of the projectile improves shielding performance. Additionally, increasing portions of the fragments can melt or vaporize as velocities increase [2].

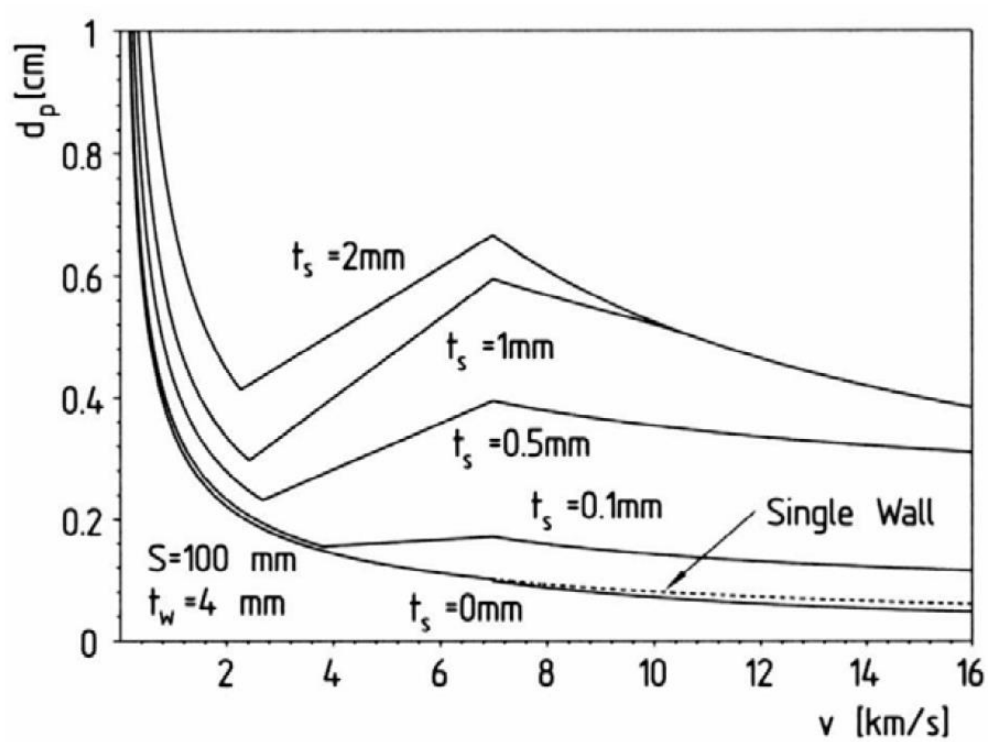

Figure 4. BLE comparison of WS and monolithic (single) wall of equivalent mass [1]. Image from NASA.

Since the development of WS, other more advanced shielding concepts were made to improve protection effectiveness. One specific area of improvement lies in increasing mass-efficiency of protection while constraining the standoff distance. Limitations to standoff are common because spacecraft usually have strict size and mass constraints. Two examples of advanced single-function

MMOD shielding are the Stuffed Whipple shield (SWS) and the Multi-Shock shield (MSS). Both advanced shielding incorporates intermediate elements between the bumper and rear walls that increase the protective effectiveness over the WS at the same standoff. Therefore, the SWS and MSS offer increased mass efficiency over the WS for stopping the same size projectile at a particular standoff. The schematic of the two new shielding concepts and their equivalent same-standoff WS comparison is shown in Figure 5. At these configurations, the masses of each shield type and the increase in the weight-efficiency with the advanced shielding types are shown in Table 2. Note that the standoff distances in this study correspond to the usual standoffs used for the ISS, which is between 10 and 30cm [15]. Additional information for other shielding designs is provided in Appendix section 10.

Table 2. Total masses for WS, SWS and MSS to protect against 1cm diameter Al projectile at 7km/s [1].

	Mass (kg)			
	WS, S=10cm	SWS, S=10cm	WS, S=30cm	MSS, S=30cm
Bumper:	1060	1620	980	910
Support:	320	490	300	270
Rear wall:	2420	940	1060	540
Total:	3800	3050	2340	1720

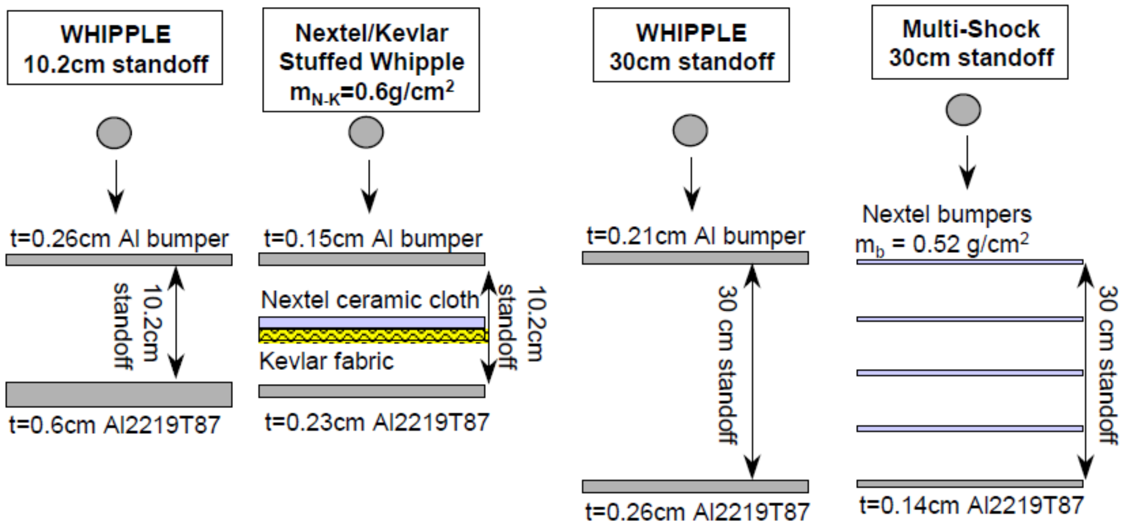

Figure 5. SWS and MSS concepts and their equivalent WS to protect against 1cm diameter Al projectile at 7km/s [1]. Image from NASA.

2.5 Distribution of fragments

As briefly described in section 1.1, debris that are tracked are sized using "characteristic length," which is simply the average of the three dimensions of the debris. Mass and characteristic length together provide a convenient estimation of the danger the debris poses to spacecraft. Furthermore, debris characteristic length easily translates into the diameter of spherical projectiles used in models and experiments.

To reduce the uncertainty in the shape distribution of the orbital debris in orbit, two specific experiments were considered. The first is the full-scale ground-based HVI tests on USA Transit navigation satellites performed by the USA Department of Defense in 1991-1992, called Satellite Orbital debris Characterization Impact Test (SOCIT). The fragments as a result of the impact were collected and characterized, leading to a large collection of fragments of less than a millimetre to tens of centimetres in length. A large portion of spacecraft stay in LEO, which are dominated by orbital debris rather than micrometeoroids. Furthermore, the majority of orbital debris consist of collision fragments [1]. Therefore, the SOCIT4 fragments provided a good estimation of the fragments in LEO. Analysis of the database of fragments by Krisko et al. in 2007 provided valuable insight into the material and shapes of the fragments [17].

The distribution of SOCIT4 fragment materials and shape from Krisko et al. are shown in Figure 6. The results show that the fragments are dominated by phenolic/plastic and aluminum material in the shapes of mainly "nugget," irregular, and flakes. The irregular category consists of the other categories of shapes but are deformed or bent in some manner. The number of aluminum fragments are less than that of plastic, but it is important to note that each individual aluminum fragment potentially poses a larger threat due to its higher density. The distribution of size and shape is shown in Figure 7. The analysis shows that most fragments are nuggets, which are ellipsoidal in shape. However, thin plate-like flakes constitute the majority of the largest sized fragments and, therefore, pose potentially larger danger individually.

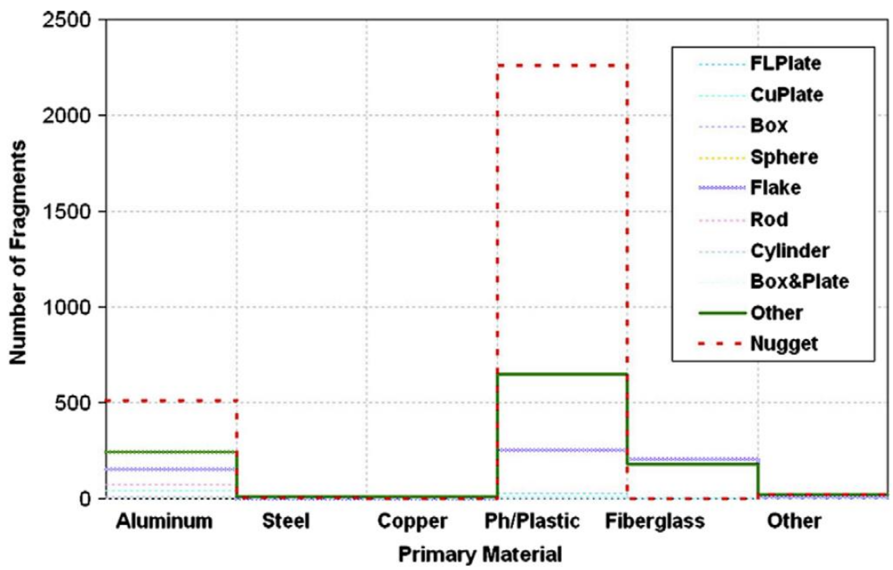

Figure 6. Distribution of SOCIT4 fragment material and shape [17].

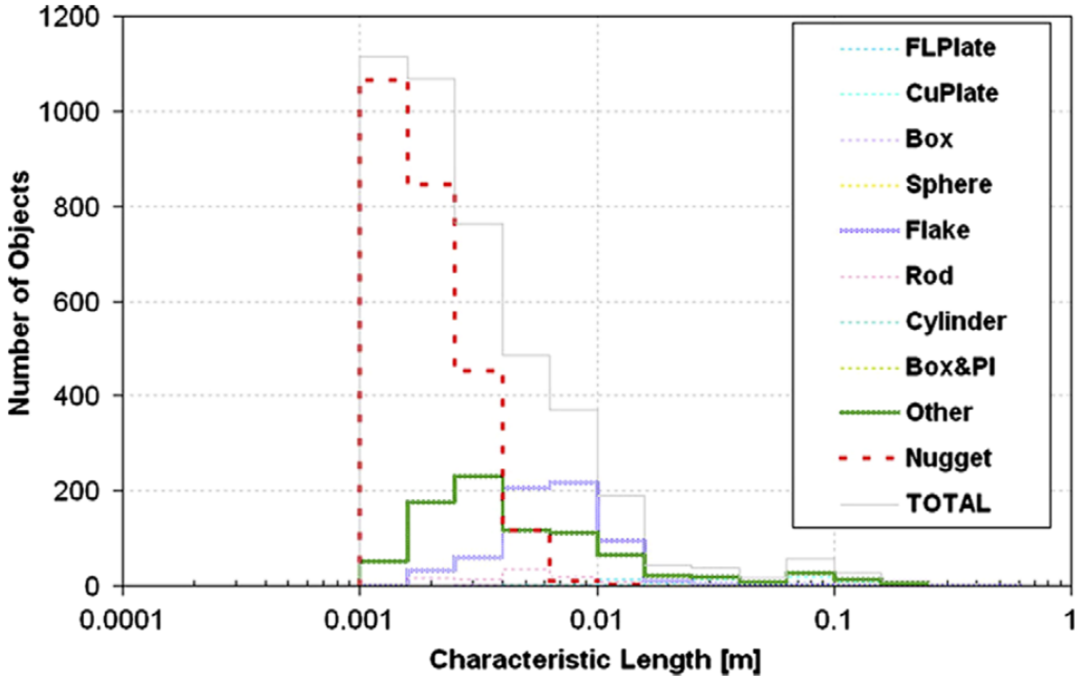

Figure 7. Distribution of SOCIT4 fragment size and shape [17].

The DebriSat project is a more recent attempt in providing insight into the distribution and characteristics of orbital debris. Similar to the SOCIT tests, the DebriSat satellite experienced HVI and the resulting fragments were collected. The DebriSat was created for the sole purpose of the experiment and was therefore designed to represent modern satellites more accurately. In contrast, the SOCIT satellite was an older design made in the 1960s. The distribution of size and shape for the DebriSat fragments are shown in Figure 8, obtained by Cowardin et al. Despite the differences between the SOCIT4 and DebriSat experiments, there is consistency in the conclusions regarding the prevalence of plate-like (flakes) and nugget (ellipsoidal) shaped fragments. However, the plate-like fragments were found to be more numerous than the nuggets and rod shapes were found to be of comparable number to nuggets.

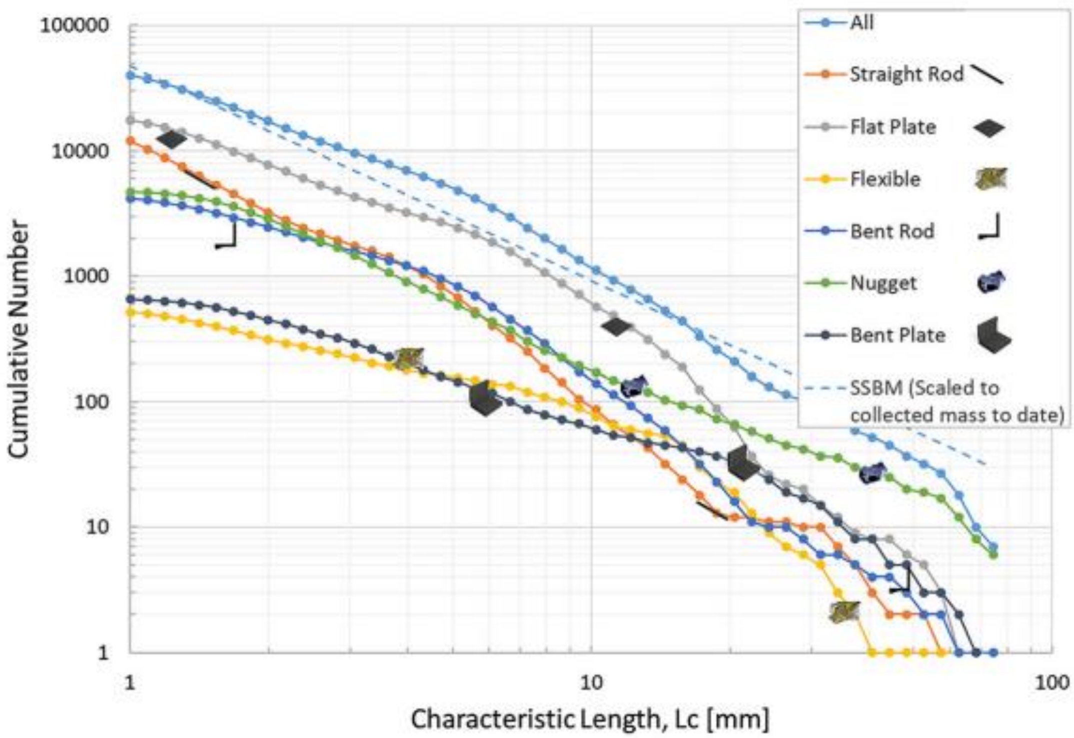

Figure 8. Distribution of DebriSat fragment size and shape [18].

2.6 Shape effect of projectiles in HVI

The development and design of spacecraft shielding is based on the results from experimental hypervelocity impact (HVI) tests and corresponding numerical simulations. The HVI tests attempt to replicate the conditions of the space debris impact and gauge the specifications of the shielding necessary to prevent perforation of a particular size projectile. The HVI tests are costly, therefore there are practical limitations on the frequency and manner they are performed. One such limitation is the use of spherical projectiles to represent the space debris impacting the shielding. Spherical projectiles provide uniformity between different experiments since accounting for other shapes is not practical due to the limited number of tests that can be performed. However, as described previously in section 2.2 regarding semi-infinite bodies, it is known that non-spherical shapes such as rods can significantly increase the damage done on the target body.

Outer bumpers on spacecraft protective shielding fragments projectiles into a debris cloud and reduces the damage of the impact on the rear (critical) wall of the shield. However, preliminary studies, such as performed by R. Morrison in [10] in 1972, have shown that non-spherical projectiles can alter the resulting debris cloud and increase the damage on the rear wall. The study performed in [10] compared cylinder with spherical projectiles on WS and found that the debris cloud for cylinders impacting normal to the bumper are more concentrated along the flight axis, producing a “spike” like shape toward the rear wall. Furthermore, the tip or front of the debris cloud moved an average of 14% faster than the initial projectile. The difference in debris cloud shape was attributed to the difference in shape of the shockwaves: cylindrical projectiles produced planar shockwaves near flight axis while sphere shockwaves are hemispherical. For this test, it was found that the mass of the cylinder must be reduced to a much lower value than the sphere in order to prevent perforation: the cylinder must be no more than 1/7th of sphere mass [10].

Further experimental study of the cylinder projectile in HVI was performed by Piekutowski [19] [11] [20]. In Piekutowski’s work, focus was made towards determining the shape and features of the debris cloud generated by differently shaped cylinders with different length-to-diameter ratio, as well as the debris clouds’ formation and propagation. However, it was clear from the results that the risk of perforation was increased over standard spherical projectiles. The experiments by Piekutowski provided a close look into the HVI of cylinder projectiles, however, observation of trends over a range of shapes was more difficult due to the costly nature of the method of study.

In more recent years, the primary method used for study has switched from experimental to computational. Increased computational resources has allowed for numerical simulations to be used to fill the gaps in physical experiments. As a result, the knowledgebase used for the design and development of spacecraft shielding (BLE) has become more robust. Study of non-spherical projectiles in HVI has also been made easier. In particular, the research work by S. Hiermaier and F. Schafer in 2001-2008 performed numerical simulations to test different ellipsoid shapes on spacecraft shielding [21]. These results have allowed the incorporation of different shapes of ellipsoids projectiles into the original BLE that are based on spherical projectiles [22]. The results allow the potential modification of shielding designs to account for non-spherical debris. However, a limitation of such works is the inability to easily adapt the results for different impact parameters.

2.7 Literature Review Conclusion

The passive protection used in spacecraft have limitations in quantity and quality of debris they can protect against. The spherical assumption used in the design of the spacecraft shielding introduced uncertainty in the performance of the spacecraft shielding. Analyses of satellite collision fragments showed that real orbital debris are largely non-spherical, consisting primarily of thin-plates, rods, nuggets and other irregular (eg. “bent”) shapes. Previous experimental and computational studies have shown significant differences in HVI behaviour depending on the shape of the projectile. Therefore, improving the understanding of the effects of non-spherical projectiles on to HVI shielding can increase the safety of spacecraft and reduce costs associated with the structure of the spacecraft.

3. **Methodology**

This section describes the approach taken to meet the thesis objectives previously outlined in section 1.3.

3.1 Evaluating Threat of Projectile in HVI

The traditional method to measure the performance of spacecraft shielding against a particular projectile is to perform ballistic limit tests. Generally, the performance of a spacecraft shielding system can be evaluated based on either its minimum weight or thickness needed to protect against a specific size of a projectile, or the maximum size of a projectile that the shielding system can stop. The reliable and straightforward approach to determine the ballistic limit is to perform a series of pass or fail HVI tests. This method is a trial-and-error approach. Since the objective requires the study of differently shaped projectiles, such a method demands an excessively large number of tests. While a numerical approach reduces cost requirements and provides versatility in adjusting input parameters, performing the many ballistic limit simulations still involve long time investments.

One of the main resource-intensive aspect of the process in determining the ballistic limit is the requirement of the pass or fail result. A failure corresponds to perforation of the projectile or spallation in the rear wall behind the bumper. The high cost of investigating the HVI under a single set of impact parameters (shape, velocity, bumper thickness, etc.) is a limitation of the previous studies described in section 2.6. Furthermore, the results of such studies can generally only be applied to scenarios with similar impact parameters.

There is a potential for expediting the determination of the ballistic limit by eliminating or reducing the required trial-and-error. The effectiveness of a shielding system is directly related to the threat posed by a particular projectile that the shielding is designed to mitigate. A higher threat level requires a higher-performance shielding system to ensure adequate protection.

By employing a quantifiable metric to assess the projectile's threat, a more comprehensive approach can be taken that eliminates the necessity for a pass-or-fail result and simplifies investigations into the effect of non-spherical projectiles on spacecraft MMOD protection.

3.2 Intermediary Metric

To assess the threat of projectiles impacting spacecraft shielding under various conditions, an intermediary metric was employed. This metric reflected the projectile's capacity to cause spallation or perforation in the target shielding. The measurement of this metric after a single test eliminated the need for multiple trials per projectile. In this way, a single test each was sufficient to develop a relative assessment among a collection of different projectiles under potentially different impact parameters.

Two distinct intermediary metrics were investigated as potential indicators of projectile threat. The first metric explored was the rear-plate metric, which was conceived as a simple way of measuring the threat of a projectile in a discrete manner. The rear-plate metric was the number of thin plates a projectile perforated through before stopping. A projectile that perforated through many thin rear plates was considered a higher threat than a projectile that perforated through fewer rear plates. Furthermore, two projectiles that perforated through the same number of rear plates were considered threat-equivalent. The use of a discrete number of plates provided a clear visual metric that was convenient to measure in a physical experimental setup.

The second intermediary metric investigated was the crater-depth metric, which was conceived based on literature on semi-infinite bodies previously described in section 2.2. One of the primary considerations in the study of HVI onto a semi-infinitely thick body was the depth of penetration of the projectile. The depth of this penetration was interpreted as a metric for the threat of a projectile. Therefore, a deeper crater was considered an indication of a higher threat projectile in terms of its capacity to perforate a thicker rear wall behind the bumper. The crater depth, as opposed to other aspects of a crater such as diameter or volume displaced, was considered more useful because it was known that the depth of the largest crater in a finite plate was related to the occurrence of spallation [1]. In dual or multi-plate shielding, the HVI fragmentation phenomenon introduces complexity in the downstream impact of the debris cloud and rear wall. However, it was assumed that the many craters produced by the projectile's debris cloud onto a semi-infinite plate can still be used to gauge the projectile's ability to perforate through a finite body. In the same way as with the rear-plates metric, two potentially different projectiles with the same crater depth were considered threat-equivalent. The crater depth metric was also a convenient visual metric that was continuous, in contrast to the discrete nature of the rear-plates metric.

The goal of the intermediary metric was to develop models that could provide relative assessments of differently shaped projectiles based on their ability to perforate the rear wall behind the bumper. The output for model was the number of rear plates perforated or the crater depth of the largest crater produced by the debris cloud, which was then assumed to represent the threat of the projectile. The intermediary metric was intended to reduce the number of trials required to make comparisons between different impact parameters. In addition, the evaluation of threat between spheres and non-spherical projectiles provided potential for the representation of non-spherical projectiles with a threat-equivalent sphere of a different size.

3.3 Numerical Tools

A numerical modelling approach was used to create the models that used rear-plates and crater-depths as metrics for the threat evaluation of differently shaped projectiles. Due to the expected large number of tests to be performed, a physical experimentation approach was deemed too costly. The numerical approach also increased the flexibility and simplicity of adjusting impact parameters, such as projectile shape. Lagrange explicit finite element method (FEM) was used to model larger portions of the shielding configuration that were not expected to experience any fragmentation behaviour, such as the semi-infinitely thick rear wall in the case of the crater-depth metric. Smoothed-particle hydrodynamics (SPH) method was used to model all the bodies that were expected to experience fragmentation or large amounts of deformation. The SPH method is a mesh-less method that discretizes the solid bodies into a collection of smaller nodes or particles. The SPH method was found to be advantageous due to its meshless nature, therefore avoiding some numerical issues and instabilities such as mesh-tangling as a result of large material deformation. The limitation of such a method was that it was more computationally expensive compared to the traditional explicit FEM. Furthermore, certain HVI situations caused noticeable issues with SPH, such as the tension instability, which caused unrealistic detachment of material under tensile stress. Therefore, SPH method was used mainly on projectiles, thin bumpers and the resulting debris clouds, which were difficult to model using explicit FEM.

All models and numerical simulations described in this thesis were created and performed using commercial software Ansys Autodyn version 2021 R2. This particular software was used due to its ability to define interactions such as collision and rigid-bonding between bodies modelled using SPH and FEM.

3.4 HVI Parameters and Thesis Scope

A numerical approach combined with the novel implementation of intermediary metrics improved the efficiency in obtaining the results. Due to the numerous variables involved in HVI, it was impractical to examine all of them. Consequently, the scope of the thesis was restricted to studying only projectile shape. All other variables were kept constant. The following section describes the various impact parameters chosen and provides the justification for the choices.

- Cylindrical shape projectile:

To represent different projectiles, cylinders of varying length-to-diameter (L/D) ratios were used. The results of the full-scale satellite collision experiments SOCIT4 and DebriSat showed that thin-plates ("flakes") were the most significant in terms of number and size of fragments. Rods and nugget-shaped fragments were less numerous but still of considerable quantity. The cylinder shape was able to represent these three most common shapes by varying the L/D ratio.

- Projectile characteristic size of 6 mm:

From the SOCIT4 fragment analysis shown in Figure 7 in section 2.6, the region between characteristic size 6 mm and 10 mm represented the largest fragments that were still of considerable quantity. Therefore, this range of fragments were the most common among the most dangerous of collection of fragments. Six millimetres was chosen due to the practical experimental considerations. Heavier and larger projectiles require increasingly more sophisticated equipment in order to achieve hypervelocity speeds.

- Aluminum 6061-T6 material:

Aluminum material was chosen as the only material in all simulations because it was the most common metal used in the structures of spacecraft. As a result, it was assumed that debris as a result of collisions would also be of aluminum material. SOCIT4 results from Figure 6 in section 2.5 showed that aluminum was second in terms of quantity among the fragments. However, since aluminum is denser than plastic, the individual threat of an aluminum fragment is higher than that of a less dense fragment of equal size.

- Impact velocity 7 km/s:

Generally, 7 km/s was chosen because it is the current standard for MMOD impact testing, and many space agencies, including CSA, NASA, and ESA use this speed in their testing protocols. This allows for consistency and comparability of results between different tests and facilities. The energy of the impact at this speed is sufficient to cause full melting or vaporization of the material upon HVI. Melted and vaporized fragments in the debris cloud pose less danger to the spacecraft. Numerical simulations are typically used to complement physical tests, and using the same impact speed in simulations allows for direct comparison between the simulated and physical results and validation of the numerical models.

4. Material Model

This section describes the material model used to dictate material behaviour in hypervelocity. An appropriate material model was significant because the material behaves distinctly different in HVI compared to normal every-day conditions. Furthermore, the investigation into the HVI projectile shape effects on spacecraft shielding required the material behaviour to be as close as possible to the real behaviour. This section provides a summary of the details of the material model as well as the model validation based on literature data obtained from the debris cloud produced as a result of HVI.

4.1 Summary of Material Model

All materials in the both the semi-infinite crater depth model and the rear-plates model, including the projectile, bumper, and rear wall, consist of Aluminum 6061-T6. The material model for the aluminium was obtained from the work of Corbett in 2006 [23]. Corbett developed the numerical material model in Autodyn software to measure the diameters of the holes produced on thin plates under HVI at various elevated temperatures and velocities, including 7 km/s. The numerical results was successfully validated using physical experimental results. The details of the material model are listed in Table 3.

It is important to note that the material model was developed using spherical projectiles. Due to the complexity of the material behaviour of HVI, the applicability of the material model above for cylindrical projectiles was not guaranteed. Furthermore, the validation of the material model was not extended to the debris cloud produced from HVI with a bumper. Therefore, a separate study was performed by comparing the numerical results using the above material model with experimental data using cylindrical projectiles, described in the following section.

The material model also included element erosion. Element erosion is a non-physical numerical technique that removes or disables finite elements upon reaching a specific set of conditions, generally strain. Element erosion is not representative of any physical phenomenon and was included into the material model simply to avoid excessive mesh distortions or mesh tangling. Such mesh distortions could cause problems in the running of the simulations, the least of which include reduction the explicit FEM timestep significantly thereby increasing the computational costs to impractical levels. The erosion has no effect on parts defined with SPH method.

The erosion included in the aluminum material model was defined using geometric strain of 1.0. This erosion factor was obtained from Cherniaev in 2016, which was calibrated with an experimental HVI ballistic limit test for aluminum materials [24]. A physical experiment was replicated in simulation, where the rear wall was defined using FEM. The erosion factor was adjusted until a good agreement was reached with the ballistic limit of the particular shielding configuration.

Table 3. Aluminum 6061-T6 material model.

Mie-Gruneisen equation of state	
Gruneisen coefficient	1.97
C1, m/s	$5.24 * 10^3$
S1	1.4
Reference Temperature, K	293
Specific heat, J/kgK	885
Johnson-Cook strength model	
Shear modulus, kPa	$2.6 * 10^7$
Yield strength, kPa	$3.24 * 10^5$
Hardening constant, kPa	$1.14 * 10^5$
Hardening exponent	0.42
Strain rate constant	0.002
Thermal softening exponent	1.34
Melting temperature, K	925
Reference strain rate, 1/s	1
Strain rate correction	1st order
Johnson-Cook failure model	
D1	-0.77
D2	1.45
D3	-0.47
D5	1.6
Melting temperature, K	925
Reference strain rate, 1/s	1

4.2 Debris Cloud Validation

A study on the validity of the behaviour of the material model described previously in HVI for cylindrical projectiles was performed. This study was performed to check if the material model would provide realistic HVI behaviour for cylindrical projectiles. Special focus was given toward the debris clouds generated as a result of HVI of cylindrical projectiles with thin plates. As described previously in literature review section 2.6, the debris cloud produced represented the threat of the projectile onto the spacecraft shielding, which was dependent on the shape of the projectile and the manner of impact. Therefore, the debris clouds produced by the aluminum material model were compared with experimental data from Piekutowski in 1987, which also featured aluminum cylindrical projectiles impacting thin aluminum plates at approximately 7 km/s [11].

The configuration of the experiment consisted mainly of an aluminum 2024-T4 cylindrical projectile and a thin aluminum 6061-T6 bumper. The material model of the Al2024-T4 was similar to Al6061-T6 and was obtained from Kay in 2003 [25]. However, as shown later in section 6, the most significant fragments with regards to the threat on spacecraft shielding are generally located at the leading edge of the debris cloud, which consists mainly of fragments originating in the bumper.

The physical experiment was replicated in simulation using SPH method in Ansys Autodyn software, where the dimensions, velocities and manner of impact were made the same as in the experiment. The cylindrical projectile had a diameter and length of 7.72 mm, similar to the characteristic size of 6 mm chosen in section 3.4. The bumper was 2.03 mm thick. The procedure used for the numerical convergence of the results is described later in section 5.3. Figure 9, Figure 10, and Figure 11 shows the visual comparison of the debris clouds generated at different inclination angles and slightly different velocities[1]. In the left side of the figures, the green-colored material corresponded to the bumper and the dark-blue-colored material corresponded to the projectile. The impact velocities are close to the constant velocity of 7 km/s chosen previously in section 3.4. Qualitatively, the material model has good agreement with the experimental results. The material model properly displayed the main features of the cylinder debris cloud: main body, inner cone, and front cone, all displaying the corresponding cloud distortion as a result of the projectile inclination.

[1] Permission for reuse of experimental figures obtained from CCC’s RightsLink® on Mar. 8, 2023.

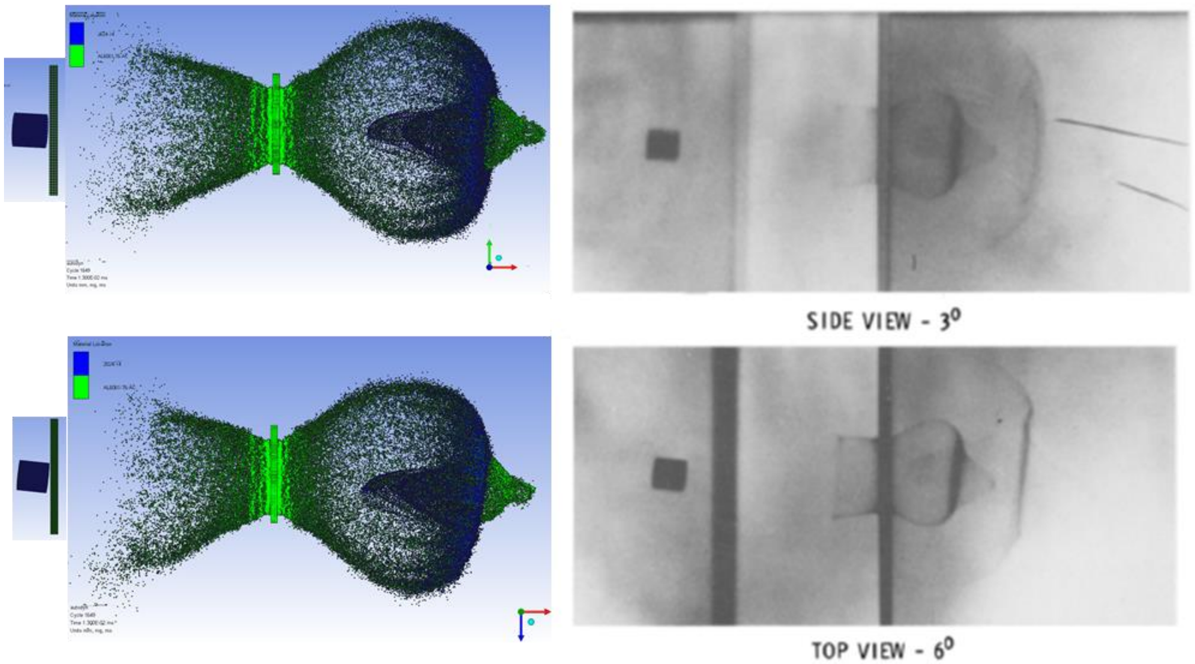

Figure 9. Visual comparison of debris cloud Autodyn simulation (left) and physical experiment (right) of 7.72 mm diameter cylinder at 6.48 km/s and 7 degrees inclination [11].

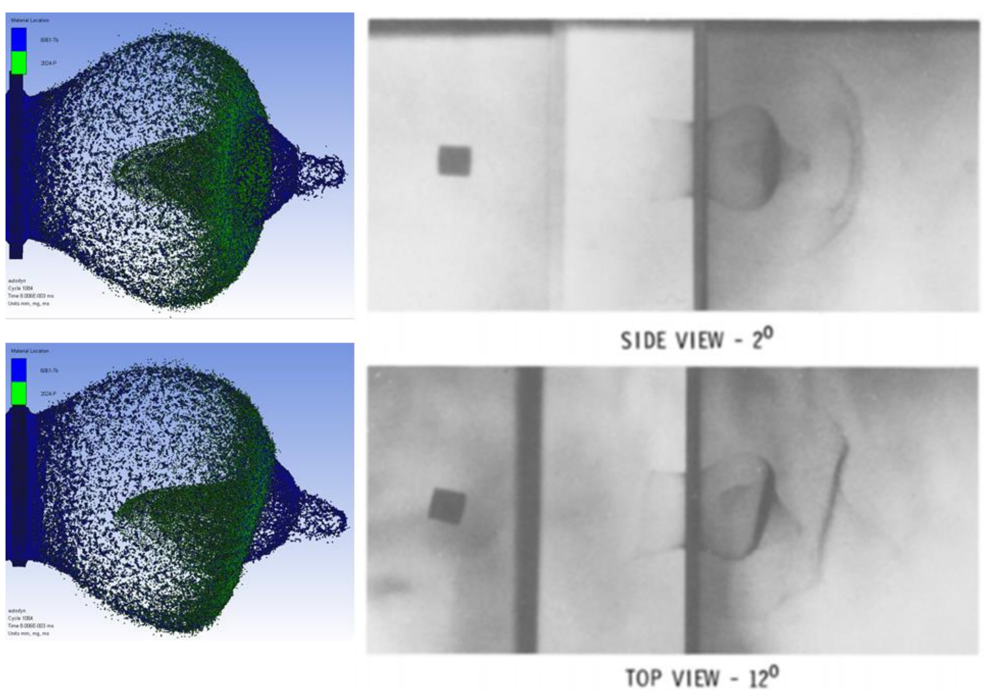

Figure 10. Debris cloud from Autodyn simulation (left) and physical experiment (right) of 7.72 mm diameter cylinder at 6.30 km/s and 12 degrees inclination [11].

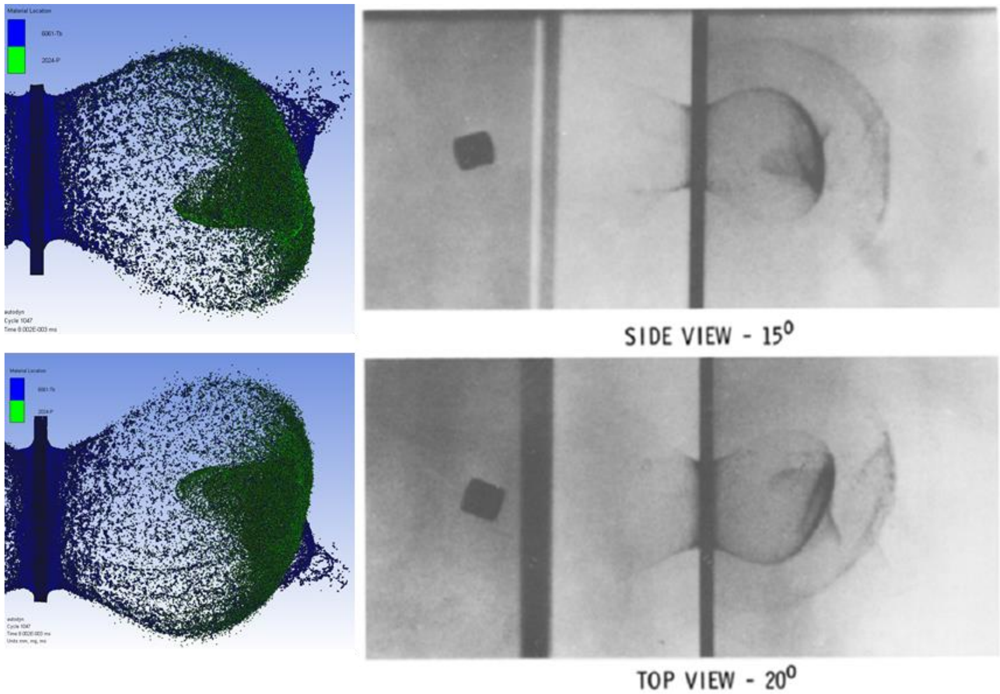

Figure 11. Debris cloud from Autodyn simulation (left) and physical experiment (right) of 7.72 mm diameter cylinder at 6.39 km/s and 25 degrees inclination [11].

One of the most important aspects of the debris cloud is the velocity of the leading edge, which corresponds to the frontal portion of the front cone of the cloud for cylindrical projectiles. The front cone of the cylinder debris cloud is particularly important due to its contribution into the damage caused by the cloud as a whole. The importance of these most dangerous fragments are described in more detail in section 6. Table 4 lists the normal leading edge velocities between the material model and the experiment. The material model was found to have less than 5% relative error near normal impact (zero inclination). The relative error in material model was found to increase with increasing inclination, with an error of 10.7% at 25 degrees. For normal impact involving cylinders, the material model was found to be sufficiently validated.

Table 4. Comparison of normal leading edge velocity for material model and physical experiment [11].

Inclination (deg)	Impact velocity (km/s)	Experimental leading edge velocity (km/s)	Numerical leading edge velocity (km/s)	Relative error (%)
7	6.48	6.7	6.6	1.49
12	6.30	6.4	6.7	4.69
25	6.39	5.6	6.2	10.7

5. Crater Depth Metric Analysis[2]

This section contains the description of the developed numerical model and the results of the numerical analysis using crater depth as the intermediary metric. The model was used to investigate and compare the threat of differently shaped projectiles.

5.1 General Geometry

The SPC model was configured in a way similar to the Whipple shield, simply consisting of a bumper and a rear wall. However, the rear wall was replaced by a semi-infinitely thick plate. The rear wall was made semi-infinite in order to measure the crater depths produced by the cylinder projectiles' fragments. In this model, the crater depth was considered as the representation of the threat of the projectile with regards to the projectile's ability to perforate through a finite rear wall. More detail regarding the intermediary metric chosen was previously described in section 3.

A schematic of the numerical model is shown in Figure 12, where S is the standoff distance, t is the thickness of the bumper, L is the length of the cylindrical projectile and D is its diameter. The projectile impacts the bumper normal to the surface. Table 5 lists the various characteristics of the

[2] Some parts of this section are modified excerpts from "NUMERICAL STUDY OF THE EFFECTS OF ORBITAL DEBRIS SHAPE AND OBLIQUITY ON ITS PERFORATION ABILITY," by Patrick Domingo and Igor Telichev, for the 8th European Conference on Space Debris in April 2021.

model. The mass of the cylindrical projectiles are each equal to the mass of a 6 millimeter spherical projectile of the same aluminum material and their dimensions are listed in Table 6.

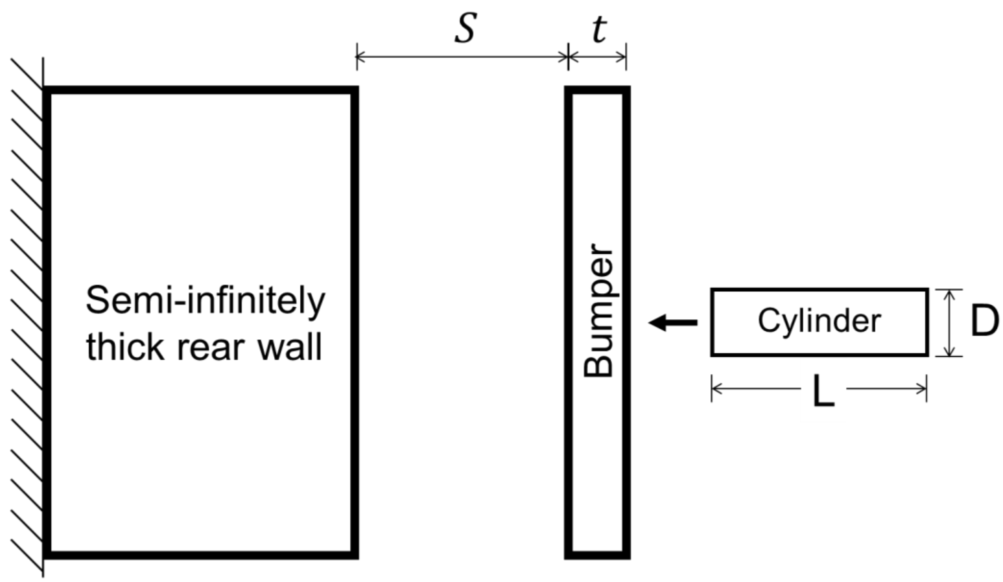

Figure 12. General schematic of crater-depth numerical model (not to scale).

Table 5. Crater-depth model model parameters.

Standoff S, mm	15, 100, 150
Bumper thickness t, mm	1.5
L/D	1/3, 2/3, 3/3, … 6/3
Impact velocity, km/s	7
Projectile mass, g	0.3057

Table 6. Dimensions of the cylindrical projectiles with mass of 0.3057 g.

L/D	L (mm)	D (mm)
1/3	2.52	7.56
2/3	4.00	6.00
1	5.24	5.24
4/3	6.35	4.76
5/3	7.37	4.42
6/3	8.32	4.16

Different standoff distances were investigated due to the surprising differences found in the preliminary results. Described in more detail in the following chapters, the results showed that the output of the model was sensitive to standoff distance. Furthermore, in the investigation of craters produced by cylindrical projectiles, the thickness of the bumper was kept constant at t =1.5mm, which corresponded to the minimum thickness to cause full fragmentation in a 6mm spherical projectile at 7km/s [1]. For a projectile and bumper of the same material at the current standoff distances, the minimum bumper thickness is simply a quarter of the sphere diameter [26]. The effect of the bumper thickness on the primary results was investigated separately, described later in section 6.

In the models used for S=15 mm and S=100 mm, a rigid body was placed between the bumper and the semi-infinite rear wall. The rigid body contained a hole in its center coinciding with the axis of the velocity of the projectile, allowing only a portion of the debris cloud to pass on to contact with the semi-infinite rear wall.

5.2 Model Configuration

Three slightly different variants of the model were developed depending on the standoff distance. The differences consist mainly of the inclusion of a rigid body between the bumper and the semi-infinite rear wall and the method (SPH or FEM) used to define the semi-infinite rear wall. All three variants included symmetry along two planes.

5.2.1 S=15mm and S=100mm

For S=15 mm and S=100 mm, almost all the parts were modelled using the SPH method due to the fragmentation of the projectile and the large deformations at the crater of the rear wall. Especially at S=15 mm, the standoff distance is small enough such that the crater produced is expected to be significantly large, therefore involving large material deformation. A cross-section side-view and oblique view of the model is shown in Figure 13 and Figure 14, respectively. These figures show only the S=15 mm variant of the model, however, the S=100 mm model variant was nearly identical with an increase in the standoff distance. Due to the high computational cost of using the SPH method, the computational domain was reduced to the minimum required to maintain consistent results, including the total size of the rear wall and the radial size of the bumper.

The portion of the rear wall modelled using SPH was chosen to be of sufficient size to encompass the central largest crater produced by the debris cloud.

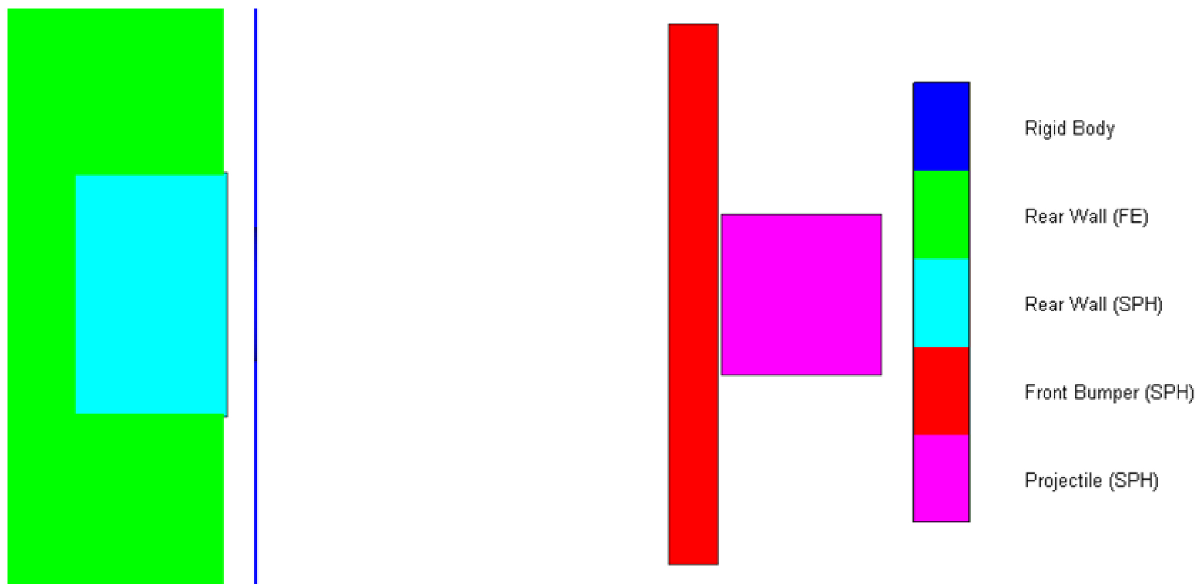

Figure 13. Cross-section side-view of model for S=15 mm.

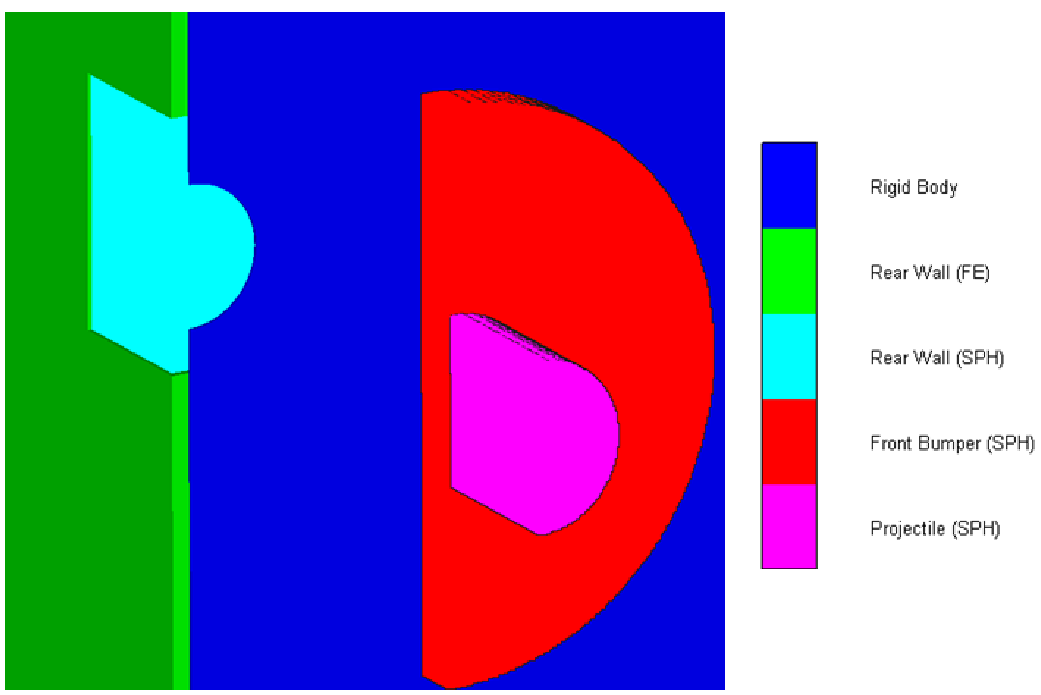

Figure 14. Cross-section oblique-view of model S=15 mm.

To model the rest of the semi-infinite plate, finite elements (FE) were used in combination with the smaller SPH portion. The FE were rigidly joined to the SPH nodes along the surface boundary between the SPH and FE in the rear wall. The two parts therefore behaved as a single body representing the rear wall. The geometric sizes of both the FE and SPH portions of the rear wall were chosen such that they were just large enough to have negligible influence on the crater produced by the debris cloud.

Since the output desired from the model was the depth of the semi-infinite plate crater, it was assumed that only the largest crater was necessary to model. Therefore, only the largest crater produced by the debris cloud determined the pass or fail conclusion for the projectile onto spacecraft shielding. Furthermore, it was assumed that the peripheral fragments would have negligible influence on the central crater. This assumption was considered reasonable because the central portion of the debris cloud for normal impact contained the fragments with the largest momentum, found from the fragment analyses described later in section 6. A rigid body was placed between the front bumper and the rear wall to allow only passage and impact from the central portion of the debris cloud. The opening in the rigid body was centered along the velocity vector of the projectile. By introducing the rigid body, the computational requirements of the model were reduced significantly.

The specific sizes of the various parts are listed in Table 7.

5.2.2 S=150mm

From the numerous simulations performed in the three different standoff distances, it was observed that the computational requirements increased with increasing standoff distance. The reason for this increased cost is due to the spread of the debris cloud as it propagated through the standoff distance. The debris cloud spreads out over time, potentially reducing the localized damage on the rear wall, which was the original intention in the use of the bumper. However, the spread of the cloud also increased the resolution required to define the individual features and fragments of the debris cloud.

As a result of the increased computational cost, the model described in the previous subsection was altered. The primary change was the switch from using SPH in the rear wall to using entirely

FEM. In the S=15 mm and S=100 mm cases, a small portion of the rear wall was defined with SPH in order to more accurately define the largest central crater. At S=150 mm, it was assumed that the damage and the craters were small enough such that the contact interaction between SPH debris cloud and the FE rear wall sufficiently modelled the cratering process.

With only FE, an erosion factor described previously in section 4, was used to ensure no numerical issues were encountered in the cratering process of the HVI. It was assumed that the erosion factor would be suitable for use in HVI against a semi-infinite plate in addition to the finite plate that the erosion factor was calibrated for.

Table 7. Sizes of the various parts of crater depth model.

Standoff (mm)	Projectile	Part sizes (mm)			
		Bumper	Rear Wall (SPH)	Rear Wall (FEM)	Rigid Body Opening Radius
15	cylinder	1.5 thick; 8 radius	10x6x6	30x30x30	3.1
	sphere		11x7x7		3.3
100	cylinder		5x5x5	40x40x40	4.0
	sphere		4x5.5x5.5		4.5
150	all		-	50x50x50	-

5.2.3 Mesh, Connections, Contact and Boundary Conditions

The finite element size and size of the SPH particles for the three variants of the crater depth model are listed in Table 8. The SPH particle size and finite element size were numerically converged and the procedure used is described later in section 5.3.1. At each standoff distance, all SPH parts had uniform particle size. For the S=15 and S=100mm variants, the element size of the FEM portion of the rear wall was of minimal importance because the primary concern was the crater produced on the SPH-portion of the rear wall. The FEM rear wall elements near the SPH portion were required to have an element size that was a multiple of the SPH particle size so that the inner (SPH) and outer (FEM) rear wall parts were properly fitted together. As shown in Figure 15, the mesh density for the finite elements decreased the further away they were from the central region of the rear wall. In the case of the S=150 mm variant, where the rear wall consisted entirely of finite elements, the elements were smallest near the central region. However, the high central element density region extended to a size of 10x20x20 mm, whereas the high element density for S=15 and S=100mm extended only slightly beyond the SPH portion of the rear wall.

Table 8. Element size and SPH particle size for the crater depth models.

Standoff	Projectile	SPH Particle Size (mm)	Total Number of SPH Nodes (approx.)	Finite Element Size (mm)	Total Number of Elements (approx.)
15	cylinders	0.065	2 million	0.195	300 thousand
	spheres		2.8 million		
100	cylinders	0.06	1.1 million	0.12	2 million
	spheres		1 million		
150	all	0.055	800 thousand	0.25	2.6 million

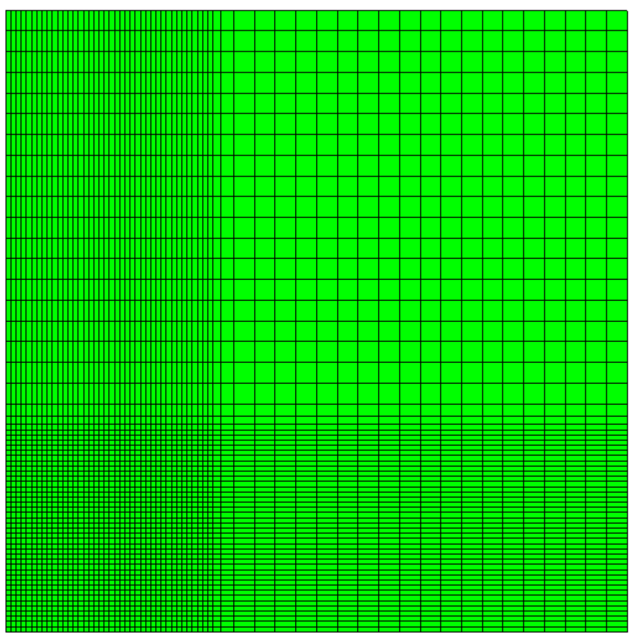

Figure 15. Finite element sizes on one-quarter of the contact surface of the rear wall, where bottom left corner represents the center of the rear wall. The SPH portion at the center was hidden.

For the S=15 and S=100 mm variants, the outer surface nodes of the SPH rear wall were rigidly bonded to the inner surface of the FEM rear wall. To prevent unrealistic behaviour due to a rigid connection, the SPH-FEM bonding was placed sufficiently far away from the expected location of the large crater. Furthermore, the rigid body prevented peripheral cloud fragments from interacting with the outer surface nodes of the SPH body.

For the S=15 and S=100 mm variants, there was no contact defined between SPH debris cloud and the FEM rear wall, only between the debris cloud and the SPH-portion of the rear wall. For S=150, contact was defined between the FEM rear wall and the debris cloud. Contact was defined with Autodyn external gap method, which created contact zones around the surface of the bodies that provided a normal force proportional to the depth of penetration into the contact zone. The timestep of the simulation was restricted such that the fast-moving cloud fragments required several cycles propagating inside the contact zone. The size of the contact zone (the "gap") was chosen sufficiently small such that there was consistency in the primary crater depth output.

The boundary conditions for the model consist only of the zero-velocity condition for the finite element nodes at the rear surface of the semi-infinite plate. The initial conditions of the system consist of only the projectile in motion moving normal to the bumper at 7 km/s with all other parts at rest.

5.3 Model Verification

This subsection describes the procedure used to determine the convergence of the crater depth model. Achieving convergence of numerical results was important in ensuring that the results obtained from the model were not misleading as a result of numerical errors.

5.3.1 Numerical Convergence

The primary results of the simulations were the craters produced on the semi-infinite plate, therefore the depth of the craters were used as the metric for the numerical model's convergence. The numerically converged output was found by incrementally increasing the number of SPH nodes or finite elements in the various parts of the numerical model. Convergence was determined after the primary output has remained within 10% relative difference with the previous iteration three times in succession. At each step, the error in the conservation of energy was kept within 10% of the initial system energy. An example of the crater depth convergence is shown in Figure 16 for impacting a 6mm sphere at S=15mm. Similar conclusions were made by converging cylinder L/D=1, therefore it was assumed that results from all other cylinder shapes were equally converged. The same procedure was used to determine the numerical convergence for the finite elements of the rear wall for the S=150 mm variant of the crater depth model. The SPH particle size and finite element size were converged separately.

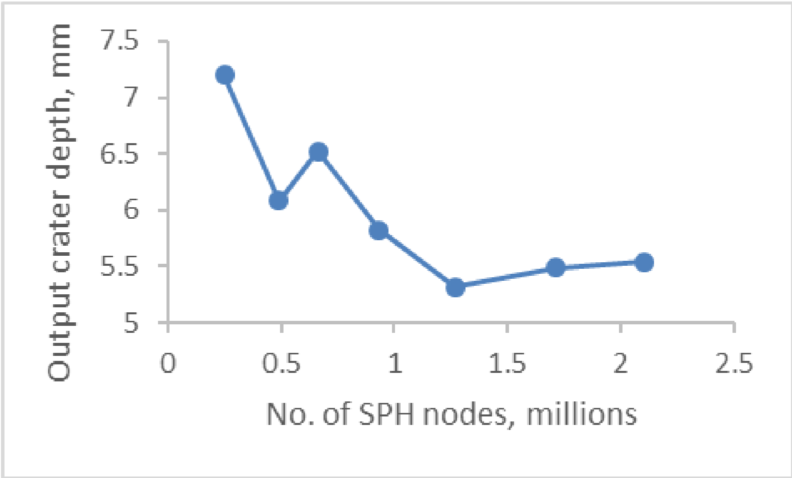

Figure 16. Convergence of output as number of SPH nodes increased for 6 mm sphere impacting crater-depth model at S=15 mm.

The geometric size of the FE and SPH portions of the rear wall were determined in a trial and error process. The crater depth produced by a specific projectile was measured as the geometry of the rear wall was incrementally changed. The trial and error procedure was performed until consistency in the crater depth was reached. This procedure was repeated to determine various other geometries of the parts of the crater depth model listed previously in Table 7 in section 5.2, such as rigid body opening size or the minimum acceptable bumper radius.

5.3.2 Convergence Limitation

A limitation in the convergence procedure described previously in section 5.3.1 was the large number of tests that was required for a single projectile shape, such as the 6 mm diameter sphere and the L/D=1 “nugget” cylinder. However, the results outlined later in section 5.4 show that there were considerable differences in the debris cloud depending on the shape of the projectile. Therefore, it was possible that convergence requirements changed as a result of simply changing the shape of the cylinder projectile, with all other parameters kept the same. In addition, it was previously discovered that increasing standoff distances also increased computational requirements, therefore, the convergence requirements changed yet again. Due to time constraints, it was not possible to perform convergence studies on all the various projectiles shapes at every standoff distance considered. Convergence study was limited to a single projectile shape at every standoff distance. In this way, a base minimum requirement for the mesh and SPH particle size was determined for the three standoff distances.

In the situations where obtaining the convergence was considered impractical due to time constraints, it was assumed that sufficient visual resolution in the critical regions of the debris cloud would lead to consistent crater depth output. Achieving sufficient visual resolution entailed that the shape of the debris cloud at the critical region contained enough detail such that additional increase in number of SPH particles did not cause significant visual change. In this situation, the critical region of the debris cloud corresponded to the portion of the cloud that had the largest contribution into the largest crater produced on the semi-infinite rear wall. The critical region of the debris cloud contained the “representative fragment,” which is described later in section 6. The visual shape of the debris cloud of SPH particles was difficult to quantify, therefore, there was a degree of user interpretation with regards to whether the debris cloud’s critical region was sufficiently resolved. For example, a quarter of the debris cloud frontal cone of a L/D=5/3 cylinder right before HVI with rear wall is shown in Figure 17, illustrating the change in the visual resolution of the frontal cone as the number of SPH particles are increased. In this case, there was a significant change in visual resolution moving from 185 thousand SPH particles to 465 thousand. However, increasing the number of SPH from 465 thousand to 850 thousand, there is less change in the shape or visual resolution of the frontal cone. In the case shown in Figure 17, the region between 465 and 850 thousand SPH particles would be considered to have sufficient visual resolution.

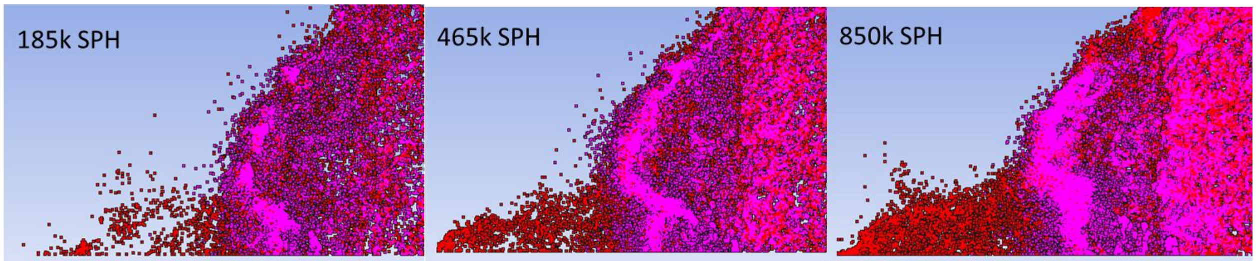

Figure 17. The change in resolution of debris cloud with increasing number of SPH particles, image taken right before HVI with rear wall. Material in red consist of bumper material and material in pink is projectile material.

For each projectile shape, the simulation was set at the minimum converged requirement for the specific standoff distance. The debris cloud was then observed visually to ensure that the critical region of the debris cloud had sufficient visual resolution. Other alternative techniques in checking the apparent convergence of debris cloud was developed involving the study of fragment momentum, described later in section 6.

5.3.3 Rigid Body

Since the output desired from the model was the depth of the semi-infinite plate crater, it was assumed that only the largest crater was necessary to model. Therefore, only the largest crater produced by the debris cloud determined the pass or fail conclusion for the projectile onto spacecraft shielding. In the crater depth models for S=15 mm and S=100 mm, a rigid body was placed between the front bumper and the rear wall to allow only passage and impact from the central portion of the debris cloud. The opening in the rigid body was centered along the velocity vector of the projectile. The rigid body reduced the computational requirements of the model significantly.

The size of the rigid body opening was minimized such that the geometry of the other parts in the model could also be reduced further. Of particular importance was the reduction in size of the SPH portion of the rear wall, which contained the majority of the SPH nodes. However, the opening in the rigid body still required to be large enough to contain the debris cloud fragments that had significant influence on the main crater. Using a trial and error procedure, the crater produced by a specific projectile's debris cloud was measured as the opening size was increased. This procedure was repeated until consistency in crater depth was reached. For these trials, the crater was measured at a specific simulation time before the crater had fully formed. This was done because only the consistency of the crater depth value was required.

The ideal rigid body opening size was found to depend on the features of the debris cloud. Figure 18 shows an example of the variation in crater depth produced by a L/D=1 cylindrical projectile's debris cloud as the opening size was increased. In the case of cylindrical projectiles, the trials showed that the largest crater depth in the rear wall depended mainly on fragments contained in what is known as the front cone of the debris cloud. The front cone of the debris cloud produced by a L/D=1 cylinder is shown in Figure 19, which corresponds to the rigid body opening size of approximately 3 mm in Figure 18.

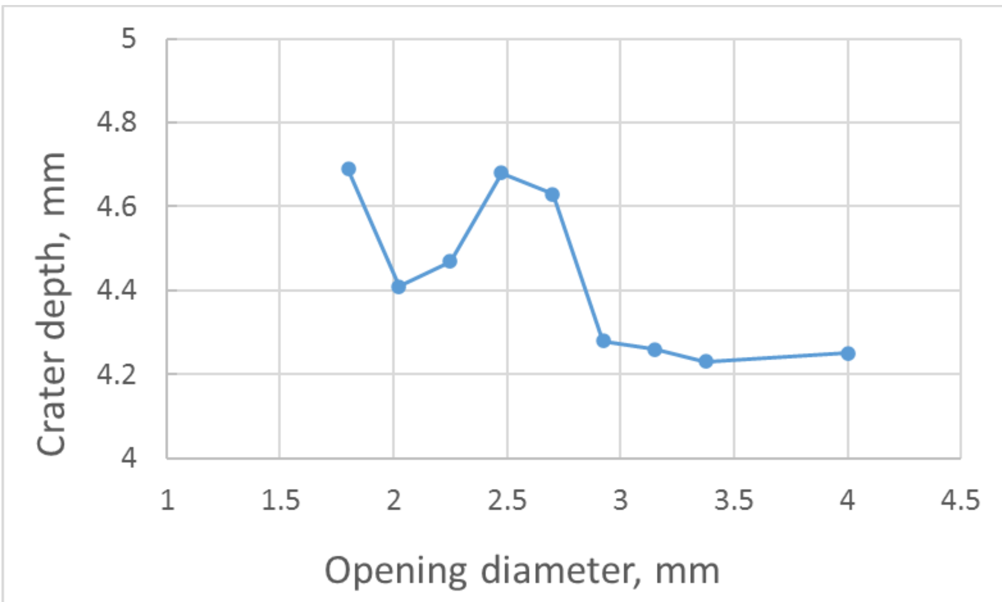

Figure 18. Crater depth produced by L/D=1cylinder debris cloud as rigid body opening was increased.

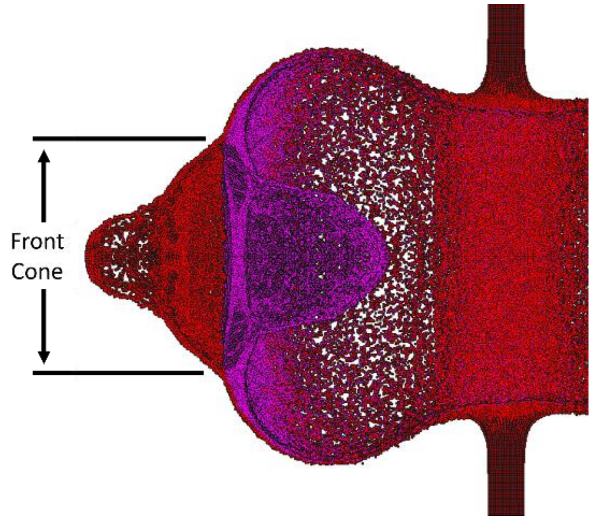

Figure 19. Example debris cloud model of L/D=1 cylinder after impacting bumper at 7km/s.

5.4 Results

This subsection describes the debris clouds generated by the differently shaped cylinders and the results of the output of the crater depth model.

5.4.1 Debris cloud

The shape of the debris cloud was known, based on literature, to depend on the shape of the projectile. An example of the debris clouds for the cylindrical projectiles: L/D=1/3 thin-plate ("flake"), L/D=1 "nugget," L/D=5/3 "straight rod," and a 6 mm sphere impacting at 7 km/s are shown in Figure 20. The crater depth models were run using two planes of symmetry, therefore each of the four debris cloud images consist of a mirrored pair. The figures show that the leading edge, that is, the fastest fragments in the debris clouds are contained in the central axis in the motion of the cloud. For the thin-plate and nugget shaped projectiles, the fastest fragments are also the most massive. In a few cases, such as the sphere debris cloud, the most massive fragments are slightly off-centre from the central axis. Analysis of the fragments is shown later in section 6 as part of the bumper thickness study.

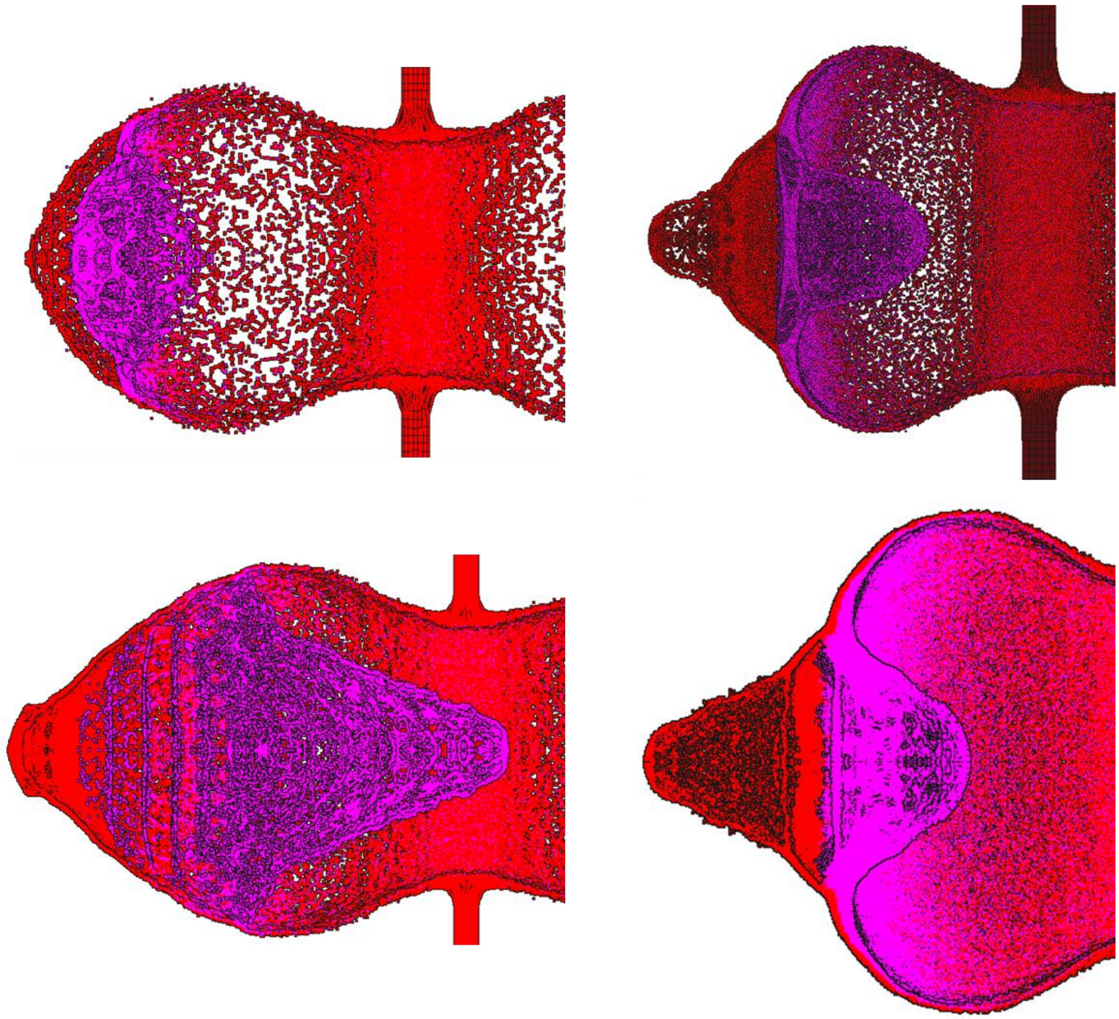

Figure 20. Examples of debris cloud for 6 mm sphere (top left), L/D=1 (top right), L/D=1/3 (bottom left) and L/D=5/3 (bottom right) after impacting bumper at 7km/s. Material in red consist of the bumper and material in pink consist of the projectile.

Past a certain point in L/D, rod-like cylinder projectiles retained a portion of its original unfragmented body after normal impact with the bumper at 7km/s. A clear example of the unfragmented portion is shown in Figure 21 for L/D=3. Further analysis showed that the geometry of the projectile prevents the stress waves from fully reaching the rear portion of the material. In this situation, the unfragmented portion poses a significant risk to the rear wall. Additional tests revealed that increasing the thickness of the bumper reduced the size unfragmented portion. It is believed that, despite further increasing the thickness of the bumper, there can exist a projectile sufficiently slender (high L/D) such that the rear portion can remain unfragmented. However, future study is still required to quantify the relationship between the bumper and high L/D rod-like cylinders. For consistency, the crater depth model used a constant bumper thickness for all projectiles. Therefore, rod-like cylinders that produced large unfragmented projectiles were excluded from the crater depth models.

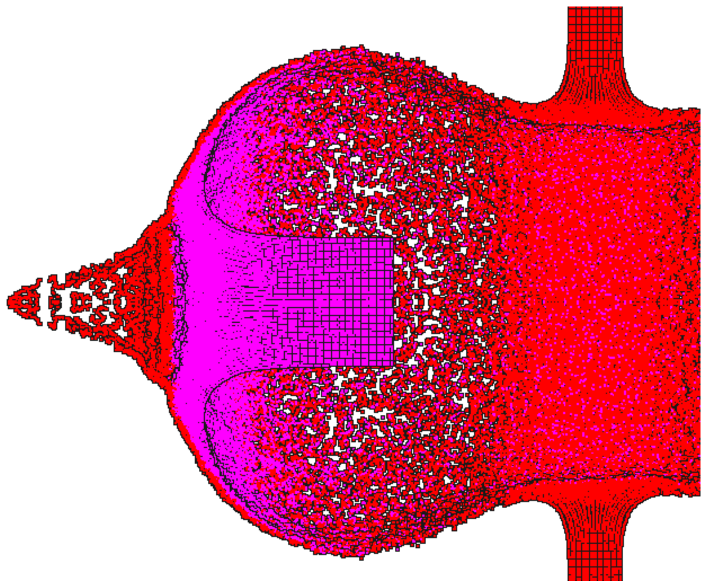

Figure 21. Debris cloud and the unfragmented portion produced by L/D=3 impacting bumper at 7km/s.

5.4.2 Crater Depth

The objective of using the crater depth model was to obtain an evaluation of the threat of a particular projectile with regards to its ability to cause failure in spacecraft shielding. The largest crater depth produced on a semi-infinite rear wall was used to represent the threat. Therefore, a simulation was performed for the various projectile shapes and standoff distances and the depth of the largest crater produced by the debris clouds were recorded. An example of the crater produced is shown in Figure 22, for L/D=2/3 at S=15 mm. The simulation was run until the depth of the large central stopped increasing in size. The debris cloud at this point in time after HVI was not at rest, however, the effect of the peripheral and distant portions of the cloud was considered negligible towards the formation of the large central crater. The depth of the crater was measured from the deepest point farthest away from the surface of the rear wall, in a straight line towards the surface location of the rear wall. The crater depth results for all the cylindrical projectiles are shown in Figure 23. The results clearly show that the craters for S=100 and S=150 mm are similar, suggesting that the extra 50 mm distance has a diminished effect on the threat of the cylinder projectile.

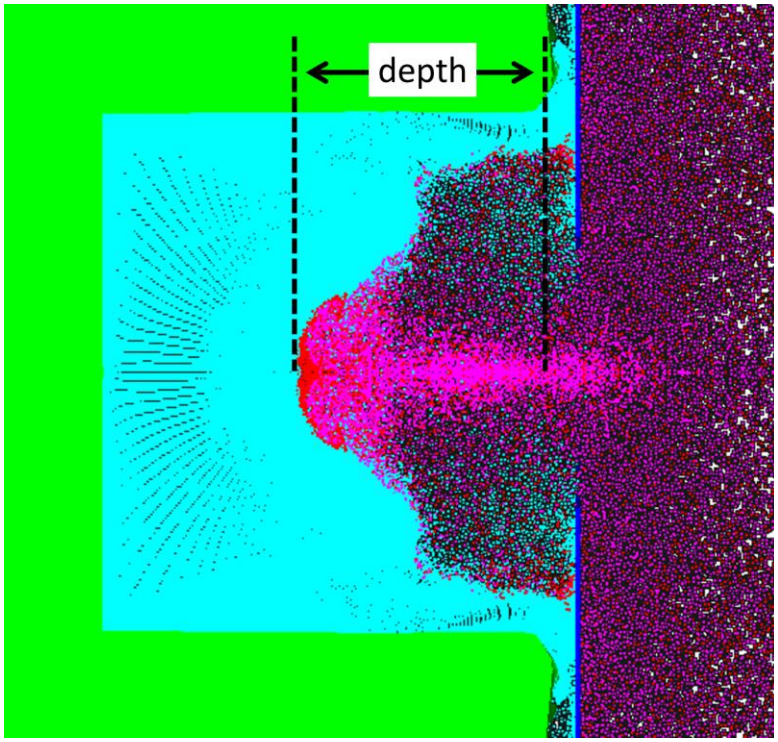

Figure 22. Measurement of crater depth for L/D=2/3 at S=15 mm. Rear wall defined using FEM is shown in green, rear wall defined by SPH in blue, bumper SPH particles in red, and projectile SPH particles in pink.

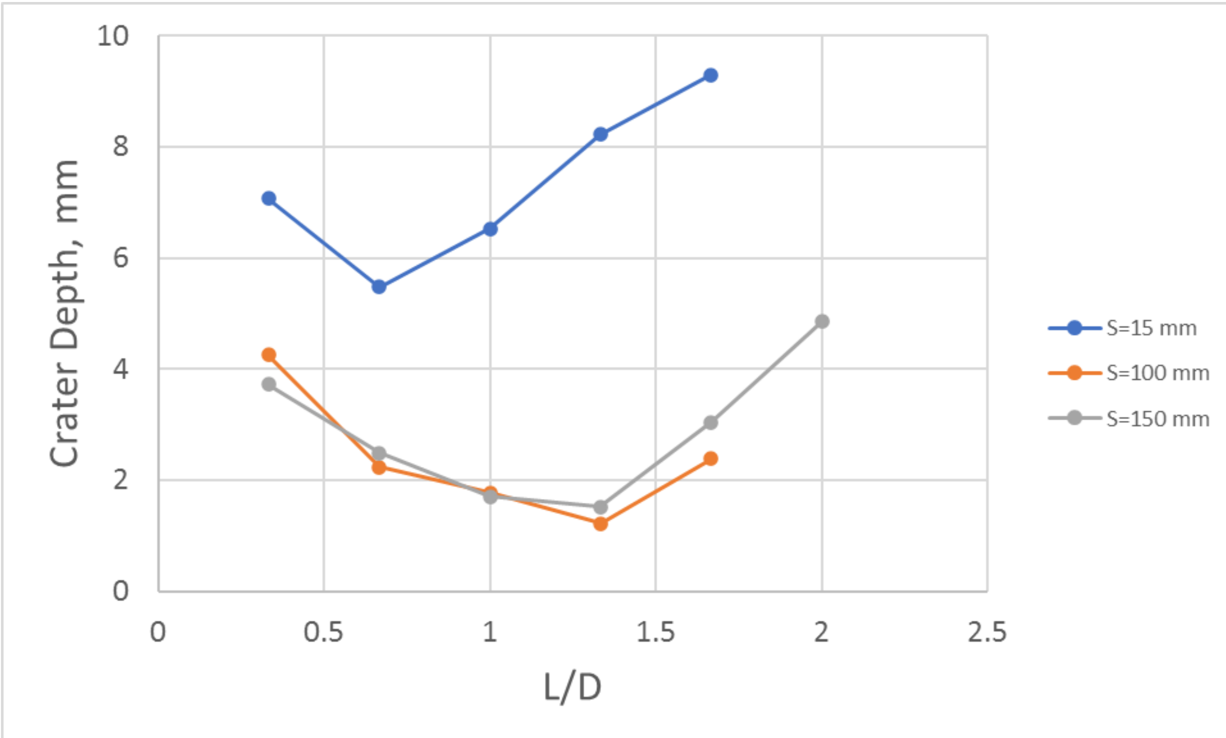

Figure 23. Crater depth results for cylindrical projectiles.

The procedure used to measure the craters produced by cylinders was repeated with spherical projectiles of increasing size for each of the standoff distances. Consequently, comparisons in the threat of cylinders with the mass of a 6 mm sphere were made with more massive spheres. An important distinction in the crater results for spheres was that the largest crater was located slightly off-centre, at approximately 4.5 mm diagonally from the center of the cloud for S=150 mm, and approximately 4 mm diagonally from the center for S=100 mm. In contrast, the largest craters for cylindrical projectiles were located at the center of the rear wall. The observations for off-centre spherical craters were found to be consistent with the debris cloud fragment analyses described later in section 6.3. At S=15 mm, the standoff was short enough that the distinctions in the location of largest crater were negligible. An example for the off-centre location of the largest crater for spheres is shown in Figure 24. The crater depth results for spherical projectiles for different standoff distances is shown in Figure 25.

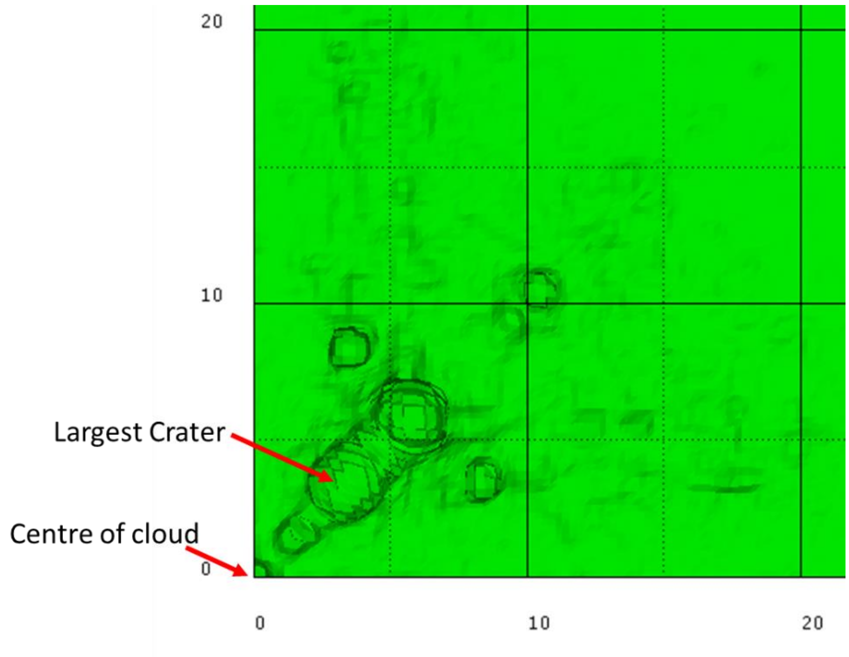

Figure 24. Frontal-view of craters produced on one-quarter of semi-infinite rear wall by debris cloud of 9 mm sphere at S=150 mm. Bottom left corner represents the center of the rear wall and where center of the debris cloud impacts. The direction of the debris cloud is into the page.

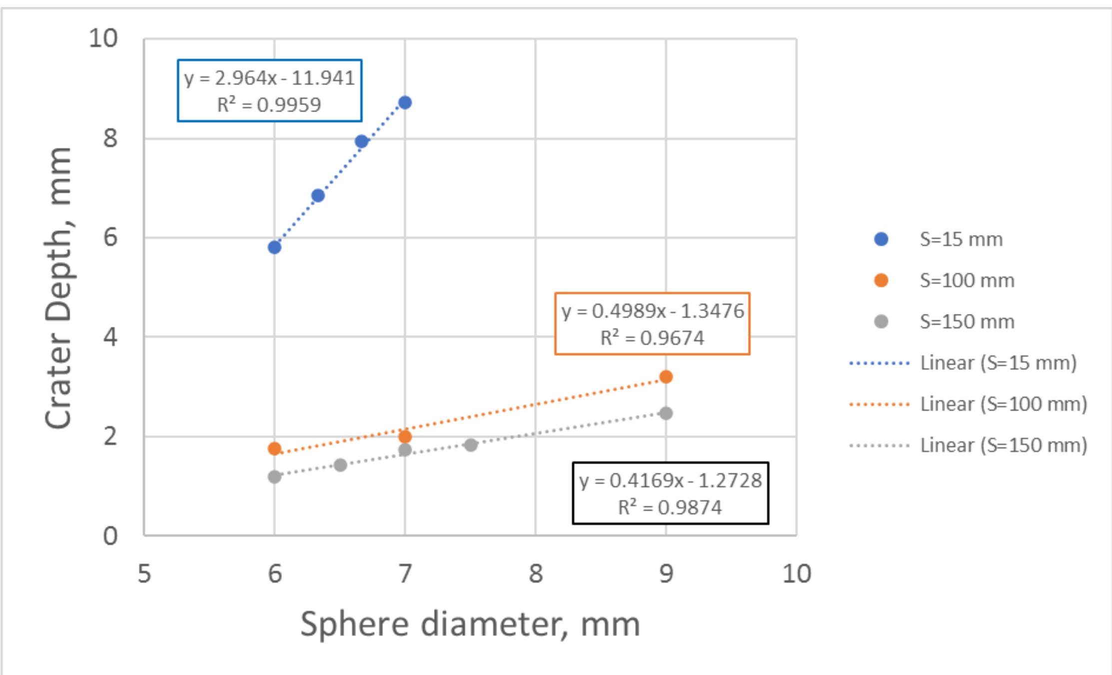

Figure 25. Depths of the largest craters produced by the debris clouds of increasingly larger spherical projectiles.

5.4.3 Threat-equivalence for sphere and cylinder projectile

In the evaluation of the threat of many differently shaped projectiles, comparisons and relationships were made. From a linear regression of the spherical results, the crater depths were compared with the results for the cylindrical projectiles. The primary working hypothesis is that crater depths approximate a projectile's ability to perforate a finite wall, therefore, projectiles that produce the same crater depths are considered threat-equivalent. Threat-equivalent results are shown in Figure 26 for the various standoff distances. The usefulness of the creation of the threat-equivalence relationship between cylinders and spheres is that the spacecraft shielding configuration designed for spherical debris could also be used to protect against a threat-equivalent cylindrical projectile. For example, at S=150 mm, the L/D=2/3 was found to be threat-equivalent to a 9 mm sphere. Therefore, spacecraft shielding designed to protect against 9 mm spheres could potentially also protect against the L/D=2/3 cylinder weighing the same as a 6 mm sphere. Thus, developing spacecraft shielding to protect against cylindrical projectiles would not necessitate a unique methodology, as the task could be accomplished by simply accommodating a sphere with equivalent projectile threat.

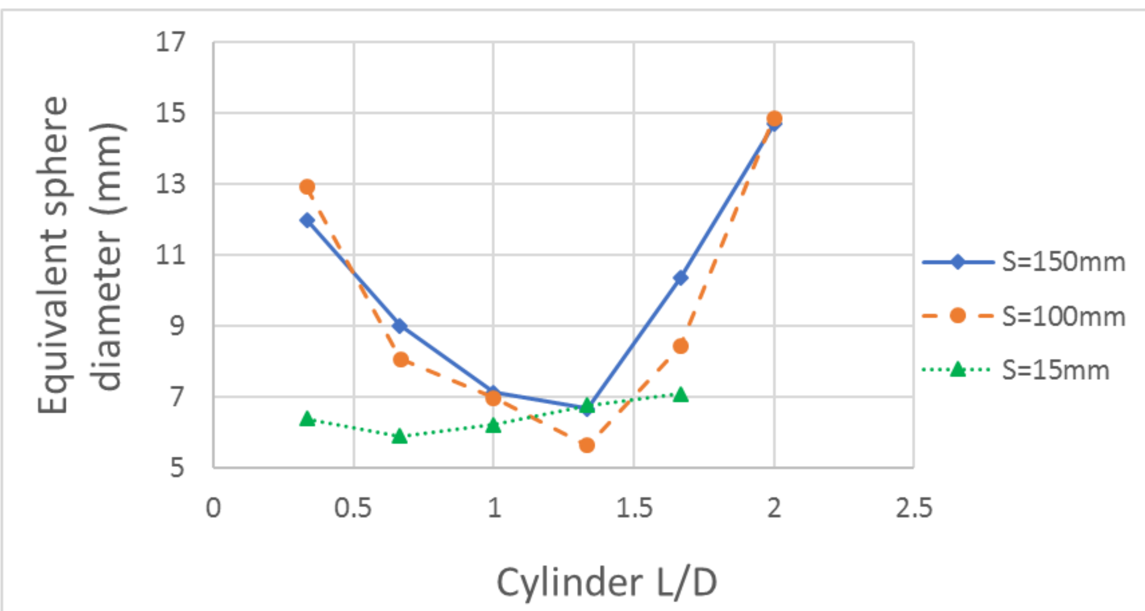

Figure 26. Threat-equivalence between cylinder and spherical projectiles based on crater depths produced on semi-infinite rear wall.

Since all the cylinders are of the same mass as a 6mm sphere, the conclusion from the threat-equivalent results is that there is a significantly increased threat from the difference in shape alone. A notable observation was that the threat of the cylindrical projectile increased as the shape deviated from L/D=1 nugget shape, which was considered to be the cylinder shape most similar to a sphere.

Another interesting observation from Figure 26 were the differences between the shorter (S=15 mm) and longer (S=100mm, S=150mm) standoff distances. These results suggested that increased standoff distance had a more pronounced effect on the threat of the debris clouds produced by spherical projectiles but less so for the debris clouds produced by cylinders. Closer investigation of the debris clouds and the positions of the fragments from cylinders confirm that the largest fragments were located near the center the debris cloud and on the leading edge, moving on the same axis as the projectile before impact. The analysis of the debris cloud fragments is described in more detail in section 6. The increased distance, intended to project the cloud over a larger surface area, has reduced effectiveness for cylinder projectiles at normal impact and zero inclination. This difference in the spread is visualized in Figure 27, showing that cylinders have increased concentration of the most dangerous fragments at or near the central axis of the debris cloud.

Conversely, at small distances (S=15mm), the results showed that there was significantly less variation in threat-equivalence for the different shapes. At these short distances, there was less distinction between the various fragments and features of the debris cloud therefore the bulk of the debris cloud contributed to the central large crater. Therefore, the cylinder projectiles were found to be of higher threat relative to spherical projectiles with increased standoff distances.

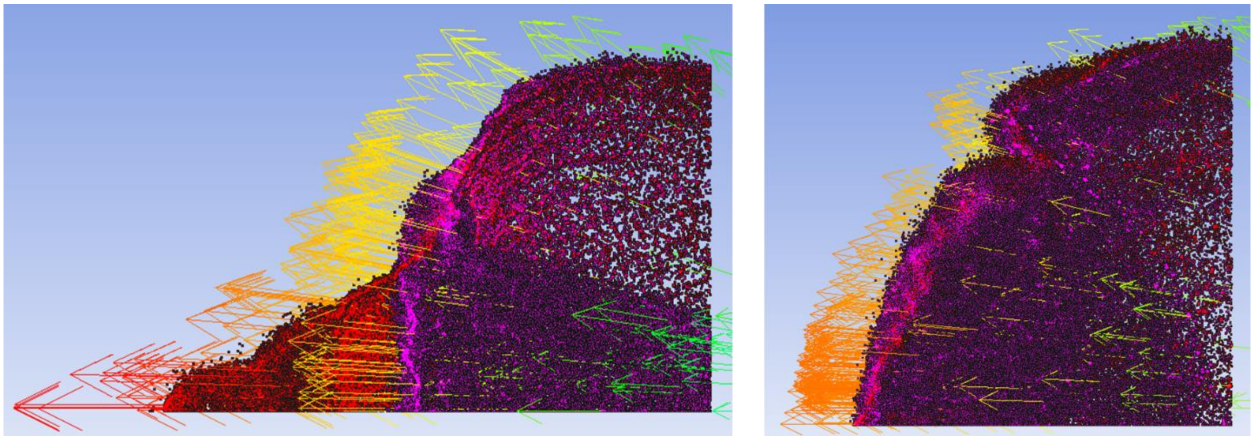

Figure 27. Quarter-view of spread of debris cloud for L/D=1/3 thin-plate (left) and 6 mm sphere (right). Arrows indicate velocity vectors, where red arrows correspond to the highest velocities at approximately 8 km/s and green arrows at approximately 3 km/s.

At approximately L/D=2, a portion of the debris cloud was not fully fragmented, which originated from the rear of the projectile farthest away from the bumper at the moment of impact. This large unfragmented portion was the main cause of the high threat-equivalence result for $L/D \geq 2$. The size of this unfragmented portion increased with L/D as the cylinder became more slender. The unfragmented portion can be visualized in an extreme example shown previously in Figure 21 of section 5.4.1.

A limitation of the threat-equivalency shown in Figure 26 is that values above 9mm equivalent sphere size are extrapolated from the linear regression of the limited spherical data shown in Figure 25. The threat-equivalency assumed that the relationship between crater depth and the size of the sphere remained approximately linear. Furthermore, another limitation of the results is that the cylinder experiments used a consistent t =1.5 mm. This decision was made to provide a consistent comparison among the various cylinder projectiles. However, spherical projectiles have increased bumper thickness requirements with increasing diameter in order to ensure full fragmentation in the projectile [1]. Therefore, the results shown previously were incomplete because of the disparity in the constant thickness used for cylinders. A study was performed to investigate the effect of bumper thickness, described later in the following sections.

5.5 Conclusion

The conclusions drawn from the crater depth metric-based analysis are as follows:

- The use of the intermediary metric method allowed for the simplification of the model optimized only for the output crater depth result.
- The developed crater depth model allowed for creation of threat-equivalence between various cylinder and spherical projectile shapes. Results required constant bumper thickness.
- The threat of the projectile at 7 km/s was found to depend significantly on the shape of the projectile and the standoff distance. The threat increases as the shape changes to be less like the nugget or ellipsoid.
- The study demonstrated that non-spherical projectiles pose a greater threat to the majority of spacecraft shielding than spherical ones. This implies that many spacecraft may be at higher risk from MMOD impacts than previously estimated. Consequently, the design of current and future spacecraft shielding must consider the effects of projectile shape to ensure that the spacecraft is adequately protected.

6. **Bumper Thickness Study**[3]

This section describes the study performed on bumper thickness: the motivation, the classification of the "representative fragment," the results of the study, and how the study was used to improve the crater depth results.

6.1 Effect of Bumper Thickness on Threat-Equivalence

The effect of the thickness of the bumper on spherical projectiles in HVI was studied in the past by Piekutowki in 1993 [27]. This experimental study showed the significance of bumper thickness

[3] Some parts of this section are modified excerpts from "NUMERICAL STUDY ON THREAT-EQUIVALENCY OF CYLINDRICAL AND SPHERICAL PROJECTILES IMPACTING DOUBLE-PLATE HYPERVELOCITY SHIELD," by Patrick Domingo and Igor Telichev, for the 2022 Hypervelocity Impact Symposium in September 2022.

and its effect on the spherical debris cloud, showing that the distribution of fragments changed with increasing thickness of bumper while keeping the diameter of the spherical projectile the same. From these results, a minimum ratio of thickness-to-diameter (t/D) was found to ensure full fragmentation in the projectile such that any further increase in thickness had diminished effect. This minimum is visualized in Figure 28, where the right images show the physical experiment debris cloud for t/D ratio of 0.234 and 0.424, where t is the bumper thickness and D is the diameter of the projectile[4]. The literature results showed that beyond approximately t/D=0.25, there was minimal increase in protection with any further increase in bumper thickness. Bumper and rear-wall (Whipple) shielding design equations as previously described in section 2.4.1, which used for preliminary design, have incorporated this behaviour to minimize the weight and cost of bumpers.

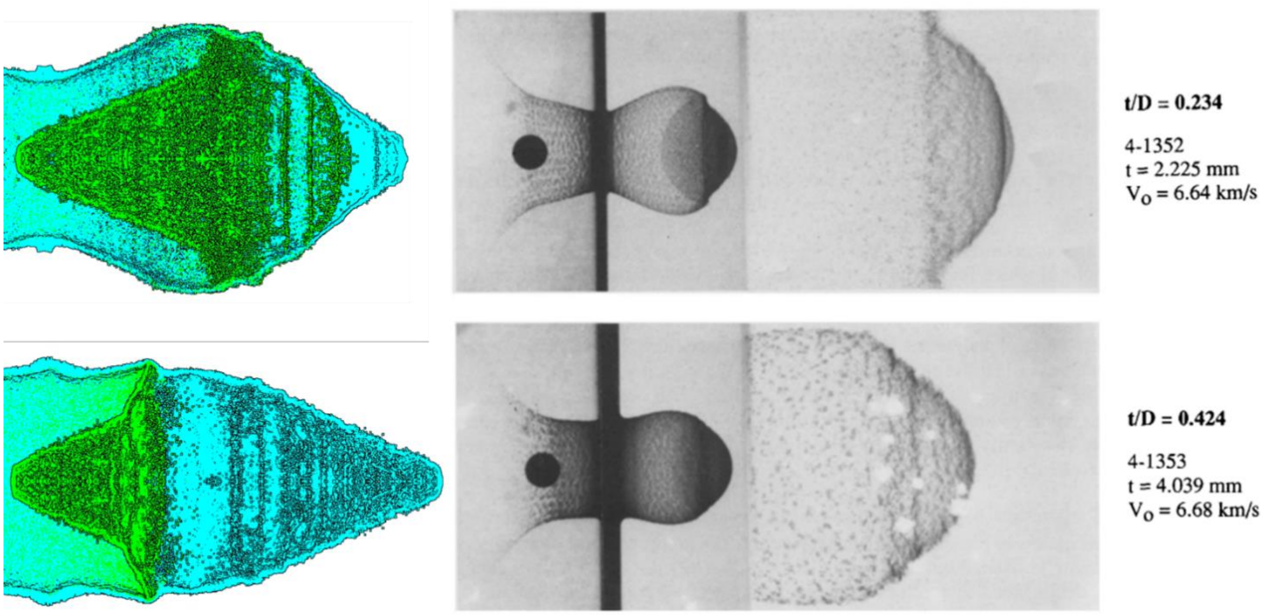

Figure 28. Debris cloud for aluminum L/D=1/3 cylinder in simulation (left) and equal-mass 9.53 mm aluminum sphere in physical experiment (right) impacting aluminum plate [27]. Green material (left) correspond to the projectile and blue material correspond to the bumper.

In contrast to the sphere, the behaviour of the cylindrical projectile was found to be different. The aluminum material model described previously in section 4.1 was used to replicate the two t/D

[4] Permission for reuse of experimental figures obtained from CCC's RightsLink® on Mar. 8, 2023.

experimental scenarios as shown in Figure 28. The mass of the cylinder was kept equal to the mass of the 9.53 mm aluminum sphere and the bumper was increased. The results of this material model for the cylinder showed that the diminished effect present for the spheres was not present for the cylinder. The cylindrical debris cloud exhibited noticeable difference in the distribution of the fragments as well as the leading edge velocity. It was hypothesized that the minimum threshold to achieve diminished further effect was simply different for the cylindrical projectiles. However, further study described later in section 6.5 and 6.6 showed no sign of the same diminished behaviour exhibited by the spherical projectile.

6.2 Examination of Crater Depth Results

In the crater depth metric analysis, the bumper thickness was kept constant in order to create a reasonable basis for the comparison of differently shaped cylinders. The results of the crater depth model led to the creation of threat-equivalence between cylinder and sphere projectiles, resulting in certain cylinders of a mass with a 6 mm sphere that are threat-equivalent with significantly more massive spheres. However, this conclusion was obtained only for t=1.5 mm. According to the design equations outlined in section 2.4.1, an increase in the projectile diameter requires an increase in the minimum bumper thickness for achieving full fragmentation. For a projectile and bumper of the same material at the standoffs considered, bumper thickness was equal to a quarter of the projectile diameter. For example, t=1.5 mm corresponded to a 6 mm sphere. The threat-equivalence results from section 5.4.3 were intended to allow existing spacecraft shielding to accommodate cylindrical projectiles by representing the cylinders with an equivalent sphere instead. Therefore, the threat-equivalence results must be modified to account for bumper thickness as well.

The most straightforward procedure to incorporate a variable bumper thickness, t_b, into the threat-equivalence is outlined in Figure 29. For each cylinder shape, the crater depth and the resulting equivalent sphere are dependent on the bumper thickness. However, the correct bumper thickness is, itself, dependent on the equivalent sphere. Therefore, an iterative procedure was required. However, this process required the crater depth simulation to be run many times for each projectile shape. This requirement nullified the efficiency advantage of using the crater depth intermediary metric over the traditional ballistic limit testing, described previously in section 3. Therefore, an alternate method using the "representative fragment" was developed.

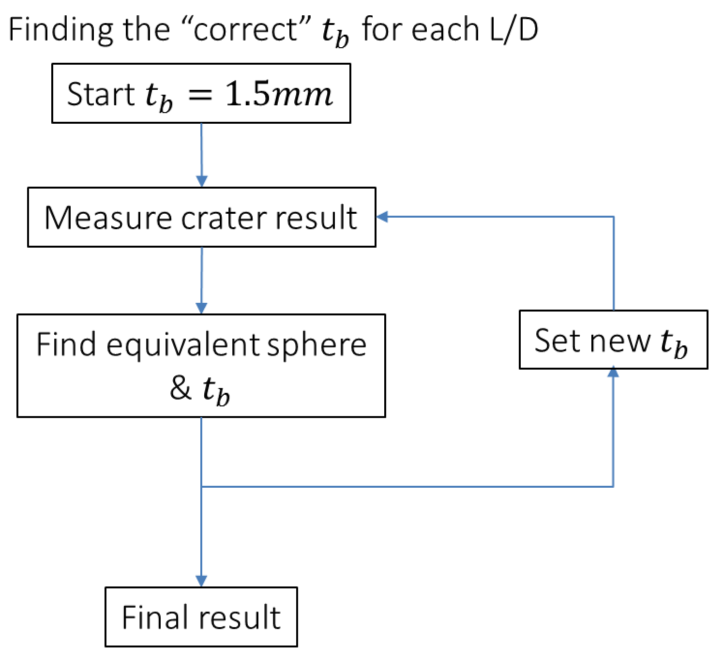

Figure 29. Iterative method for determining the appropriate bumper thickness for each L/D cylinder.

6.3 Representative Fragment

The applicability of the threat-equivalence shown previously in Figure 26 in section 5.4 was limited in usefulness due to its requirement of a fixed bumper size. However, the iterative method outlined previously in Figure 29 was found to be too time-consuming to fit into the scope of the thesis work. The value of the threat-equivalence relationship was the ability to represent the threat of a cylindrical projectile with an equivalent sphere thereby allowing existing shielding designs based on spheres to more easily accommodate potential cylinder projectiles. Therefore, a more practical and cost-effective method was developed as an alternative to the iterative approach.

The simplifications of the crater depth model were founded on the assumption that the largest and most significant crater was caused primarily by a critical region in the debris cloud. The critical region was assumed to be near the central axis and inside the frontal cone of the debris cloud. This assumption was considered reasonable because the highest velocities were also located at the central axis on the leading edge of the frontal cone. As a result, the crater depth model employed simplifications such as the rigid body to focus only on the critical central region at the expense of neglecting the peripheral and non-central majority of the debris cloud. This idea of focusing only on the most important part of the cloud was taken further to focus only on the largest fragment or group of fragments in the debris cloud, which was referred to as the "representative fragment."

A function of the Ansys Autodyn software was the ability to output the individual data of all the fragments in the debris cloud. The data included information such as location, mass, or velocity. Investigation into the data has found that, in nearly all clouds of the various cylinder shapes, there existed a fragment that had considerably larger momentum than all the other fragments in the cloud that were involved in the contact with the rear wall. This single large fragment was considered the representative fragment of the debris cloud. A clear example of such a representative fragment is shown in Figure 30 for L/D=1/3 thin-plate cylinder. The figure shows the scale of the representative fragment in relation to the whole of the debris cloud. Despite the size, the representative fragment had a momentum two magnitudes greater than the other fragments located at the center and at the leading edge of the debris cloud. The top twenty fragments with the highest momentum are shown in Table 9 for L/D=1/3. For the cylindrical projectiles, the representative fragments were also located at the center of the debris cloud. However, the difference in momentum of the representative fragment relative to the other fragments decreases as the projectile became more rod-like. As shown later in the results of section 6.7, the representative fragment of rod-like projectiles was still found sufficient for the estimation of the crater depth for rod-like projectiles' debris cloud.

For comparison, the fragment data for the 6 mm sphere is shown in Table 10. The sphere data showed sets of four identical fragments because these fragments were located slightly off-centre and were mirrored four times from the double-plane symmetry of the model. The off-centred nature of the largest fragments were found consistent with the observation of the largest craters produced on semi-infinite plates described previously in section 5.4.

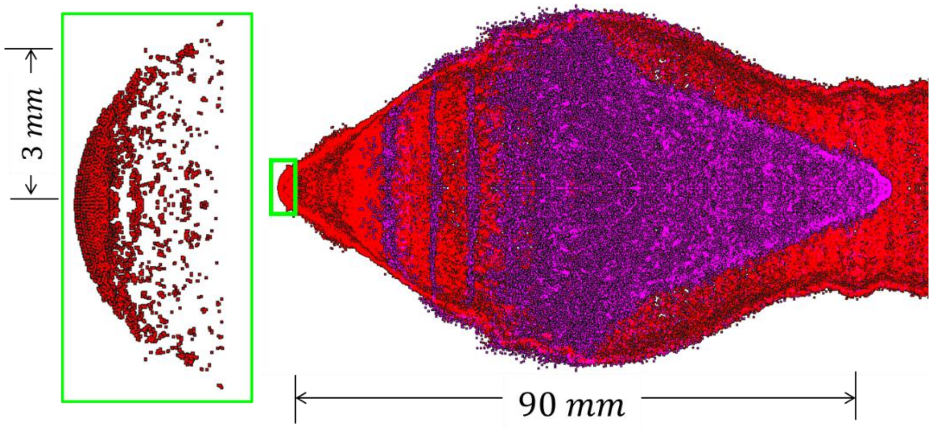

Figure 30. Location of the representative fragment (left) of L/D=1/3 debris cloud (right) 13 microseconds after HVI with bumper.

Table 9. The twenty fragments of L/D=1/3 projectile with the highest axial-momentum, t=0.013 ms after HVI with bumper 1.5 mm thick.

Mass (mg)	Volume (mm^3)	Characteristic Length (mm)	Kinetic Energy (J)	Average Speed (m/s)	X-Wise Momentum (mg*m/s)
12.5	5.01	8.31	325.0	7203	90200
0.3090	0.1360	2.79	1.030	2582	798
0.1490	0.0642	1.66	0.328	2101	312
0.0861	0.0387	1.15	0.380	2969	256
0.0393	0.0162	1.12	0.660	5791	225
0.0393	0.0162	1.12	0.660	5791	225
0.0393	0.0162	1.12	0.660	5791	225
0.0393	0.0162	1.12	0.660	5791	225
0.0401	0.0167	0.82	0.582	5388	210
0.0401	0.0167	0.82	0.582	5388	210
0.0401	0.0167	0.82	0.582	5388	210
0.0401	0.0167	0.82	0.582	5388	210
0.0535	0.0238	0.73	0.398	3859	206
0.0475	0.0212	0.55	0.404	4124	196
0.0334	0.0138	1.04	0.551	5745	191
0.0334	0.0138	1.04	0.551	5745	191
0.0334	0.0138	1.04	0.551	5745	191
0.0334	0.0138	1.04	0.551	5745	191
0.0356	0.0149	0.68	0.517	5386	187
0.0356	0.0149	0.68	0.517	5386	187
0.0356	0.0149	0.68	0.517	5386	187

Table 10. The twenty fragments of 6mm spherical projectile with the highest axial-momentum, t=0.013 ms after HVI with bumper 1.5 mm thick.

Mass (mg)	Volume (mm^3)	Characteristic Length (mm)	Kinetic Energy (J)	Average Speed (m/s)	X-Wise Momentum (mg*m/s)
0.1810	0.0686	1.28	3.01	5773	1000
0.1810	0.0686	1.28	3.01	5773	1000
0.1810	0.0686	1.28	3.01	5773	1000
0.1810	0.0686	1.28	3.01	5773	1000
0.1780	0.0677	1.25	2.97	5771	988
0.1780	0.0677	1.25	2.97	5771	988
0.1780	0.0677	1.25	2.97	5771	988
0.1780	0.0677	1.25	2.97	5771	988
0.1060	0.0404	1.03	1.76	5749	587
0.1060	0.0404	1.03	1.76	5749	587
0.1060	0.0404	1.03	1.76	5749	587
0.1060	0.0404	1.03	1.76	5749	587
0.1010	0.0384	1.24	1.67	5756	558
0.1010	0.0384	1.24	1.67	5756	558
0.1010	0.0384	1.24	1.67	5756	558
0.1010	0.0384	1.24	1.67	5756	558
0.0892	0.0350	0.75	1.69	6147	548
0.0993	0.0377	0.92	1.64	5749	548
0.0993	0.0377	0.92	1.64	5749	548
0.0993	0.0377	0.92	1.64	5749	548

The fragment data for the 6 mm sphere clearly shows that the largest sphere cloud fragment has lower momentum compared to the L/D=1/3 shown previously. However, the momentum and characteristic size of the other non-representative fragments between the two shapes' debris clouds are comparable and not too dissimilar. Since the crater depth metric analysis results indicate that the plate-like cylinder produces a much larger crater than the 6 mm sphere, one of the main contributors to this much larger crater must be the single largest fragment present for the plate-like cylinder in Table 9.

Therefore, the most dangerous fragment with the highest momentum was identified as the main contributor in the formation the largest crater on the semi-infinite rear wall in the crater depth model. This large fragment was therefore considered the representative fragment and was considered representative of the overall threat of the projectile with regards to the projectile's ability to cause failure in spacecraft shielding. Consequently, the momentum of the representative fragment was considered an additional intermediary metric in the relationship between projectile shape and bumper thickness. Measurement of fragment data was found to be significantly less expensive in terms of computational cost compared to the measurement of the crater depth directly.

6.4 Model Setup and Verification

The representative fragments analysis used a simplified model consisting of a projectile and a bumper. The projectile utilized in this model was consistent with the cylinders and spheres previously employed in the crater depth model discussed in section 5.4. The impact parameters remained constant throughout the study, with only normal impact at a speed of 7 km/s being considered. The projectile and bumper were both modelled using SPH method. The convergence of the model was performed in a manner similar to what was used for the crater depth model, described previously in section 5.3. However, the primary output of the bumper thickness study was axial momentum rather than crater depth. Therefore, the momentum was used as the metric to gauge the convergence of the numerical result. After HVI of the projectile and bumper, the debris cloud freely propagated until reaching a distance of 150 mm away from the original location of the bumper. This distance was chosen to ensure that the debris cloud was sufficiently spread out and the individual fragments was more easily identified. An example of the convergence study is shown in Figure 31. In rare cases, such as with the L/D=5/3 example shown in the figure, the location of the representative fragment inside the debris cloud changed with increasing number of SPH particles. Despite the successful convergence of the numerical value of the momentum of the representative fragment, the location of this particular L/D=5/3 fragment remained inconsistent, indicating that the debris cloud as a whole has not fully converged. However, the primary output, the momentum was considered sufficiently consistent in value, therefore, the model was considered acceptable as partially-converged.

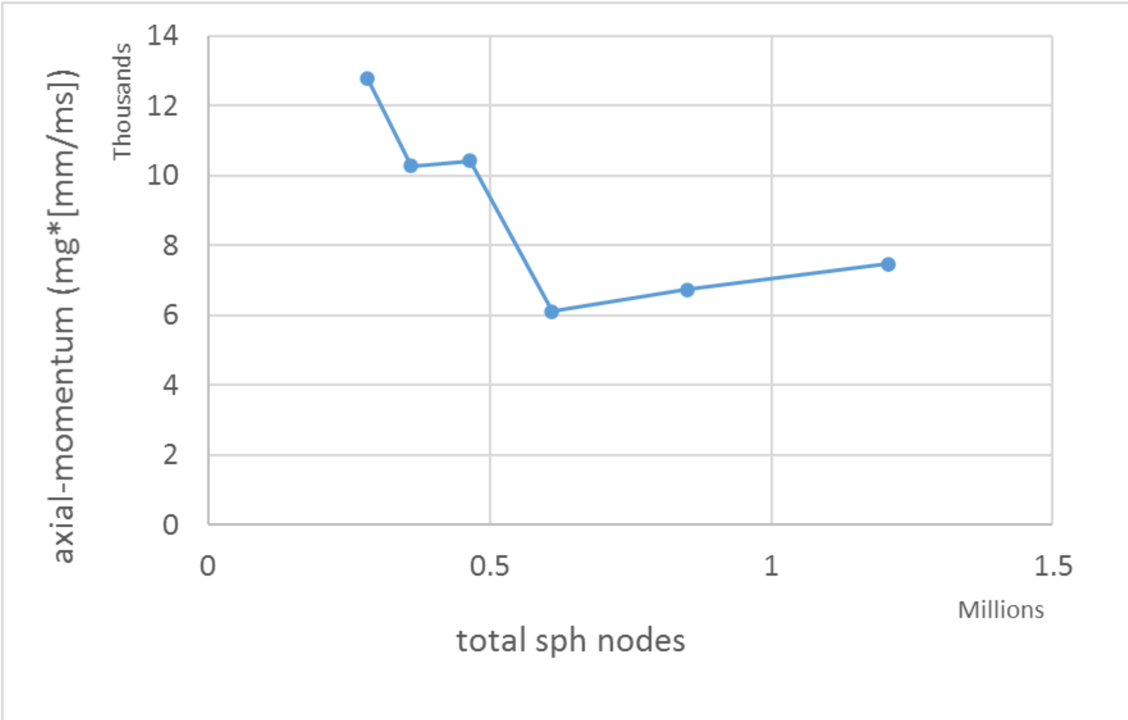

Figure 31. Example of convergence representative fragment's momentum for L/D=5/3.

6.5 Results: plate-like projectiles

Crater depths and representative fragment momentum were investigated for a single projectile shape. This investigation was performed to verify the assumption that the representative fragment could be used to estimate the crater depth result. The relationship between the momentum of the representative fragment and the crater depth produced by the debris cloud of a L/D=1/3 cylinder is shown in Figure 32, where the values are normalized to the value at t =2 mm. As the bumper thickness increased, the crater depth on the rear wall proportionally decreased at nearly half the rate that the representative fragment's momentum decreased. It was assumed that the ratio of the proportional decrease between crater depth and momentum was the consistent among the plate-like projectiles ($1/3 \leq L/D \leq 1$). This assumption was considered reasonable due to the similarities in the physical shape and location of the representative fragments. Furthermore, Figure 33 shows the similarities in the approximately linear nature in the change of the representative fragment's momentum for the various plate-like shapes. These results show that the momentum of the representative fragments could be used to estimate the crater depth of the largest crater when the debris cloud impacts the semi-infinite plate.

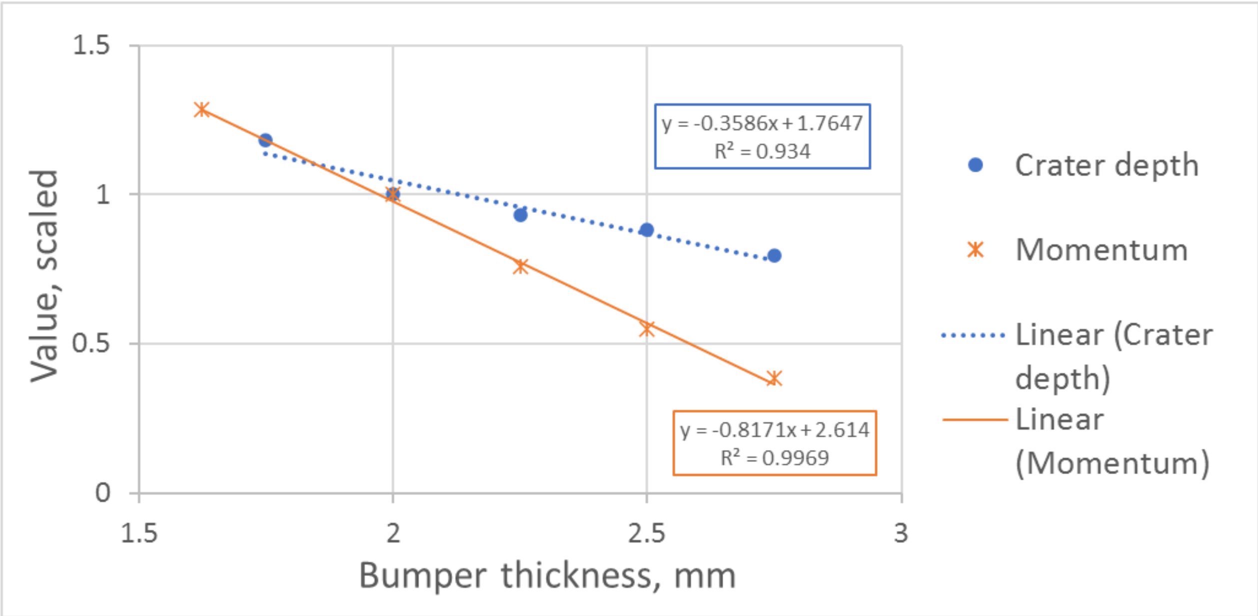

Figure 32. Crater depth and momentum of representative fragment of L/D=1/3 at S=100mm as bumper thickness increased; values are normalized at t=2mm.

From the assumption that the momentum of representative fragment approximated the crater depth, this relationship was further applied to spherical crater data previously from Figure 25 to determine how the threat-equivalent sphere of a cylinder changed with increased bumper thickness. An example of the results is shown in Figure 34. The threat-equivalencies in Figure 34 were determined from the momentum of the representative fragments, which were used to approximate crater depths, which were in turn used to approximate the equivalent sphere. The second layer of approximation from the representative fragments introduced more error in the results. However, this step was necessary because directly determining crater depths for at different bumper thicknesses was considered too computationally expensive. Conversely, the fragment momentum study was less computationally costly and served as a convenient estimate that was justified based on the nature of the representative fragment and its contribution to the largest crater's formation.

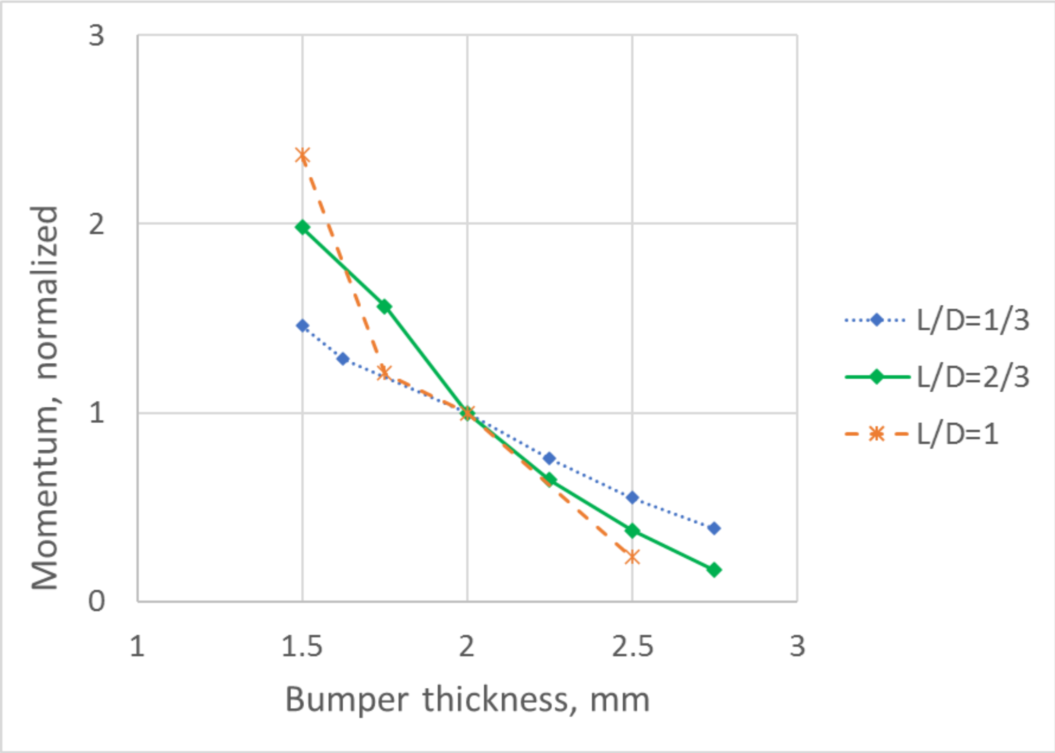

Figure 33. The proportional change in momentum of representative fragment of the plate-like projectiles as bumper thickness increased. Values normalized at t=2mm.

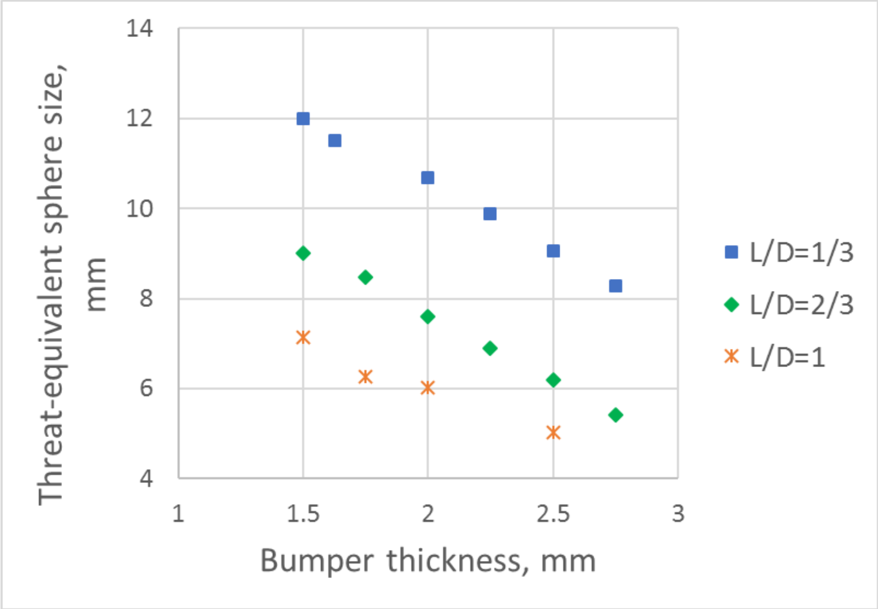

Figure 34. Approximation of threat-equivalent sphere diameter of plate-like cylinders as bumper thickness increased at S=150mm.

6.6 Results: rod-like projectiles

The behaviour of the rod-like projectiles ($L/D \geq 4/3$) as bumper thickness increased was found to be different from the plate-like projectiles. The momentum representative fragments of rod-like projectiles were only one order of magnitude greater than all other fragments. The reduced magnitude in momentum indicated that the rod-like representative fragment had a reduced individual contribution to the crater depth compared to plate-like projectiles. In addition, the relationship between representative fragment momentum and bumper thickness was found to be nonlinear. Similar to what was performed for the plate-like projectiles in Figure 32, another investigation was performed to find the relationship between rod-like crater depths and its representative fragments' momentum. The results of this investigation is shown in Figure 35, where the values are normalized to the value at t =1.5mm.

Generally, an increase in bumper thickness resulted in a decrease in both crater depth and momentum for both spherical and plate-like projectiles. In contrast, the rod-like results suggested that there were certain combinations of cylinder shape and bumper size that produced larger debris cloud fragments, despite increased bumper sizes. Analysis of the rod-like debris cloud fragments showed that the largest fragments were located not directly in the leading edge of the debris cloud and in a location of the cloud that originated in the rear of the projectile before impact.

Despite the nonlinearity, there was still a relationship between the momentum of the rod-like representative fragment and the crater depth produced in the crater-depth model. To achieve a conservative estimate, the proportional change in crater depth with bumper thickness was assumed to be equal to the proportional change in momentum of the fragment data.

In a procedure similar to the plate-like projectiles, the momentum data of the rod-like representative fragments were used to estimate the crater depths for various bumper thicknesses. These results were, in turn, applied to the spherical crater depth data for the particular standoff distance, such as in Figure 25 in section 5.4. An example of these results for S=150 is shown in Figure 36. The approximation procedure for the rod-like projectiles share the same limitations described previously in section 6.5 for plate-like projectiles, which described the potential error as a result of using momentum data.

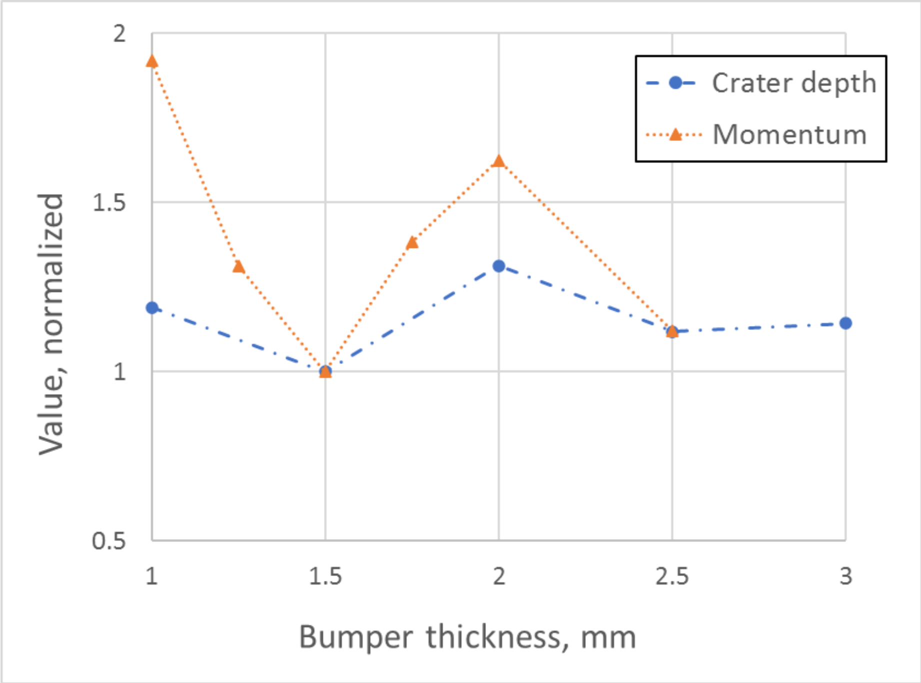

Figure 35. Crater depth and representative fragment momentum of L/D=5/3 at S=100, showing the relative increase and decrease of the values as bumper thickness was increased. Values normalized at t =1.5mm.

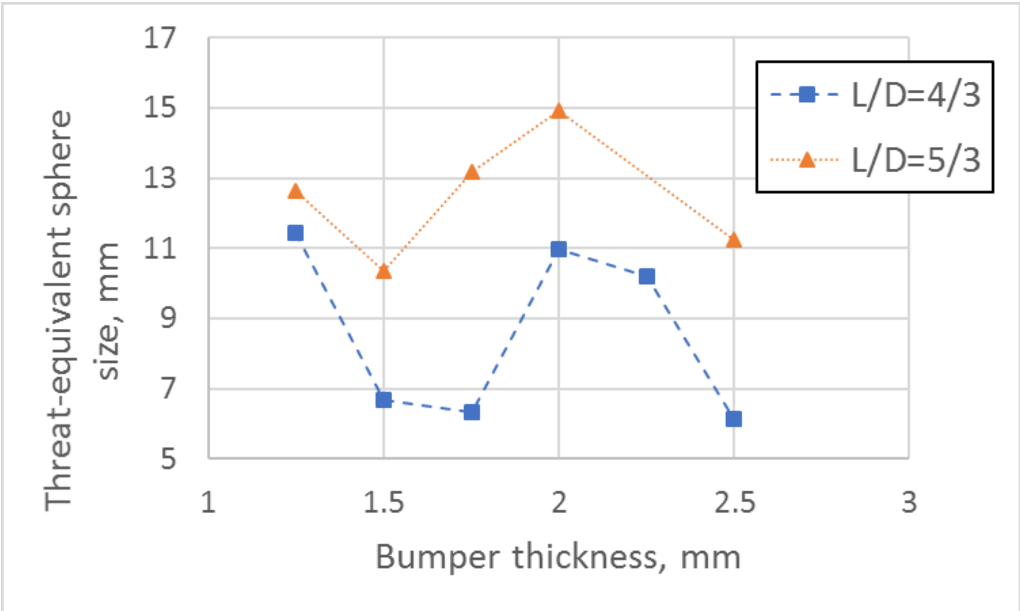

Figure 36. Approximation of threat-equivalent sphere diameter of rod-like cylinder projectiles as bumper thickness increased at S=150mm.

6.7 Adjusted threat-equivalence results

In section 5.4 for the results of the crater depth model, the threat-equivalency between spherical and cylindrical projectiles were obtained. The crater depths obtained for the spherical projectiles implemented the minimum bumper thickness required, which was a quarter of the diameter. However, for cylinders, the crater depths obtained were for a fixed thickness t=1.5 mm. To account for the relationship between projectile shape and bumper thickness, representative fragments were studied in the previous sections separately for plate-like and rod-like projectiles. The combined results of both sets of data are shown in Figure 37. The overall trends as L/D changes were found to remain the same prior to the bumper thickness adjustments. The effect of the bumper thickness adjustments are shown more clearly in Figure 38. Generally, the bumper thickness adjustment reduced the threat of plate-like projectiles. Conversely, the threat of rod-like projectiles stayed the same (S=150mm) or increased (S=100mm) as a result of the adjustments.

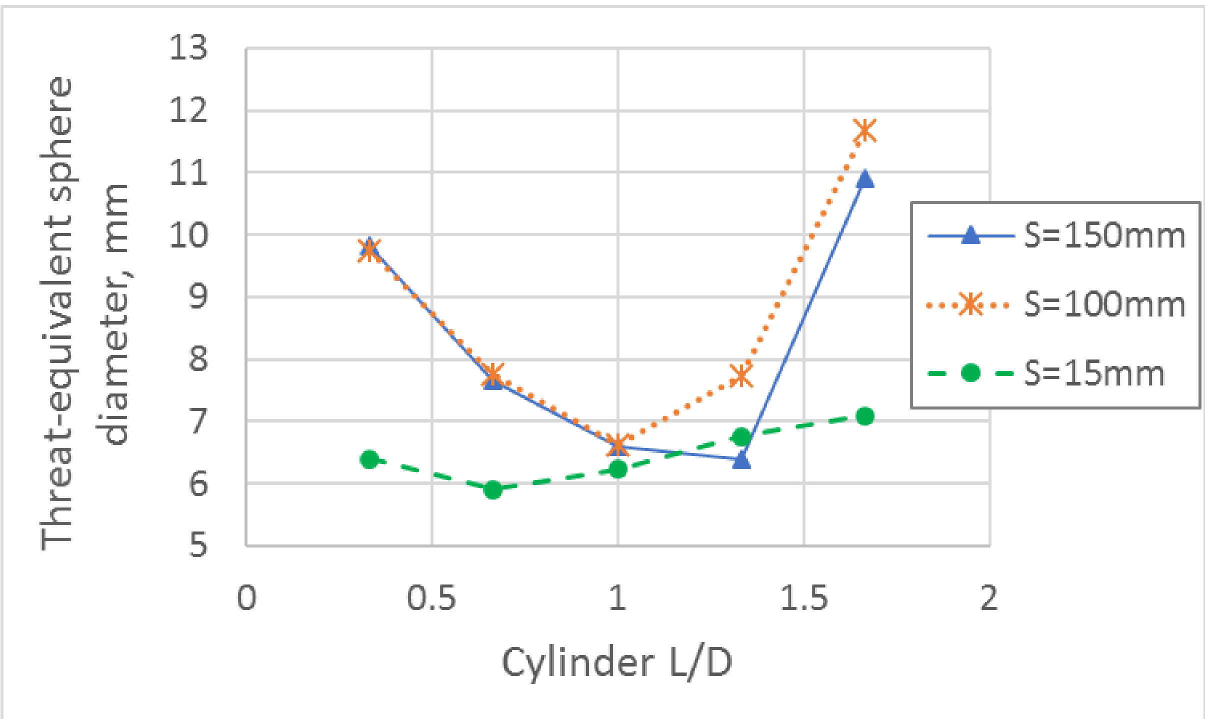

Figure 37. Cylinder L/D and their threat-equivalent sphere size, adjusted for bumper thickness

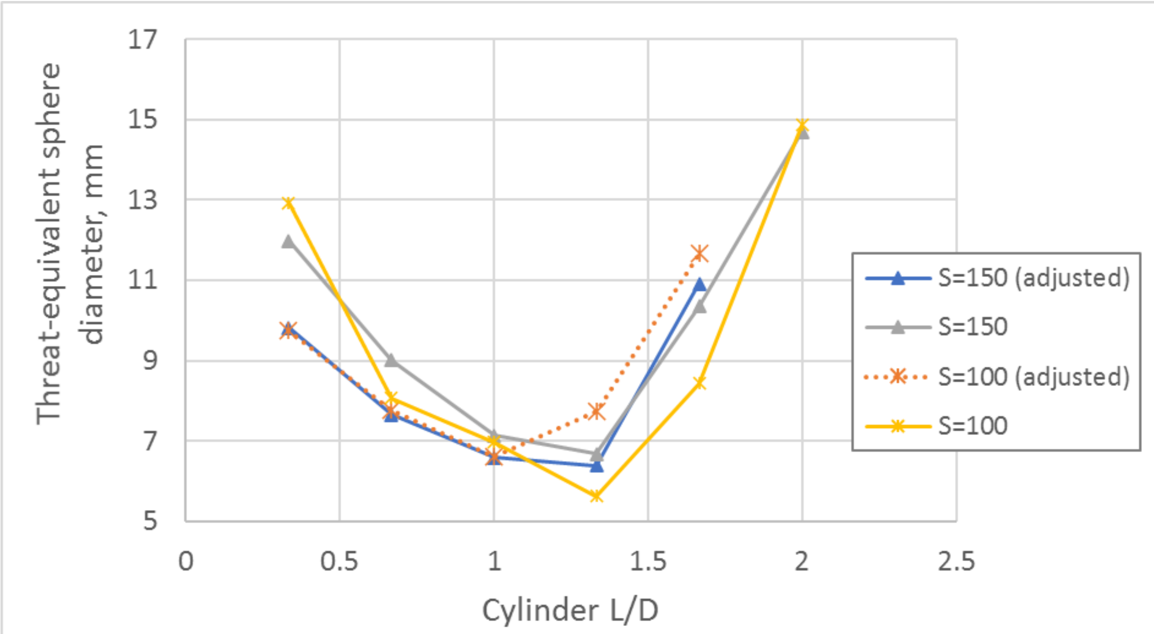

Figure 38. The difference in threat-equivalence before and after the adjustment from bumper thickness.

For plate-like projectiles, the results in Figure 37 were obtained from the linear regression of the results shown in Figure 34. An initial bumper thickness was obtained from the initial non-adjusted equivalent sphere estimate from Figure 26. This new bumper thickness was then input to the linear regression to receive another equivalent sphere estimate. The average of the two equivalent sphere results were used as a final value. The procedure was similar for the rod-like projectiles, however a fourth order polynomial was used to fit the data from Figure 36. The results for slender rod-like projectiles $L/D \geq 2$ were omitted due to the issues mentioned regarding incomplete fragmentation, previously visualized in Figure 21 in the results of the crater depth model. Lastly, the crater depth metric results for S=15mm were kept unchanged from the original results shown in previously in Figure 26 because the effects were considered negligible relative to the larger threat-equivalent values for S=100mm and S=150mm.

6.8 Verification of Crater Depth Metric

Following the results of the adjusted threat-equivalence between cylinders and spheres, a series of separate simulations were performed to test the effectiveness of the crater depth metric as a representation of projectile threat, which is the ability of projectiles to cause shielding failure.

Failure was defined as either perforation by the debris cloud or spallation of the rear wall. The tests consisted of a series of pass-or-fail simulations with a standard finite-thickness Whipple Shield setup. The tests performed were similar to the conventional procedure in the determination of the ballistic limit for a particular projectile and shielding configuration, previously described in section 3.1. To investigate the effectiveness of the crater-depth intermediary metric, the conventional ballistic limit tests were performed to find the ballistic limit of a sphere and cylinder projectile that were equivalent in threat. Therefore, a similar ballistic limit result for both the cylinder and the threat-equivalent sphere suggests that the crater depth is useful at representing the potential threat of projectiles.

The ballistic limit numerical simulations consisted of only the projectile, the bumper and the finite-thickness rear wall. Only a single cylinder-sphere pair was tested: the L/D=2/3 plate-like cylinder projectile, and its threat-equivalent sphere with diameter of 7.66 mm at S=150 mm, taken from the adjusted threat-equivalence results of section 6.7. The material model used was the same Al6061-T6 described previously in section 4. The setup was similar to the S=150 mm variant of the crater depth model, where the projectile and bumper were defined using SPH particles, the rear wall defined with finite elements, and the inclusion of two planes of symmetry. The numerically converged SPH particle size and finite element size for the S=150 mm crater depth model were used, which were listed previously in section 5.2. Similarly, the same contact definition and initial conditions from the crater depth model was used, with the projectile moving normal to the bumper at 7 km/s. Zero-velocity boundary condition was applied to the surface finite element nodes on the outer edges of the rear wall.

The projectile size and bumper thickness were kept constant, and the thickness of the rear wall was incrementally changed until the ballistic limit was determined. For a hypothetical Whipple shield designed for protection against a 7.66 mm diameter sphere, a bumper thickness of t_b=1.92 mm was used. The adjusted results of the crater depth metric analysis suggests that this hypothetical shielding also protects against normal impact of a L/D=2/3 cylindrical projectile with mass equal to a 6 mm sphere.

The determination of ballistic limit required several trials for each projectile and the results of the ballistic limit tests are summarized in Table 11. At rear wall thickness t_w =2.87 mm, the plate-like cylinder projectile was found to produce small amount of spallation at the rear of the rear wall, shown in Figure 39 as the geometric erosion of two elements in the quarter-display. For the plate-like cylinder, this was considered near the ballistic limit. At the same rear wall thickness, there was no perforation or spallation observed for the spherical debris cloud. However, as shown in Figure 40, a considerable bulging of the wall was visible, which indicated a nearly failed state for at least spallation. The 7.66 mm diameter sphere ballistic limit was approximated at t_w=2.67 mm, and the L/D=2/3 cylinder was approximated at t_w=2.87 mm. The relative difference in ballistic limit defined by rear wall thickness is 7.5%. The difference in ballistic limits implied that the threat-equivalent results slightly underestimated the threat of the plate-like projectile.

The results of the ballistic limit tests for the cylinder-sphere favourably suggested that the crater depth intermediary metric sufficiently represented the threat of a projectile under the test conditions. Furthermore, the results of ballistic limit tests indicated the necessity of the adjustment of the bumper thickness with the usage of the representative fragment because, otherwise, the L/D=2/3 cylinder would have been greatly overestimated by the crater depth results to have threat equal to a 9 mm sphere. The limitation of this conclusion is that they are the result of only a single sphere-cylinder pair due to the high computational cost of performing many trials.

Table 11. Summary of results of ballistic limit tests used to verify the crater depth intermediary metric. NP = No perforation; NS = No spallation.

Rear wall thickness, mm	L/D=2/3 cylinder	7.66mm diameter sphere
5.01	NP, NS	NP, NS
4.3	NP, NS	NP, NS
3.58	NP, NS	NP, NS
3.04	NP, NS	NP, NS
2.87	Spallation, NP	NP, NS
2.67	Perforation	Spallation, NP
2.15	Perforation	Perforation
1.43	Perforation	Perforation

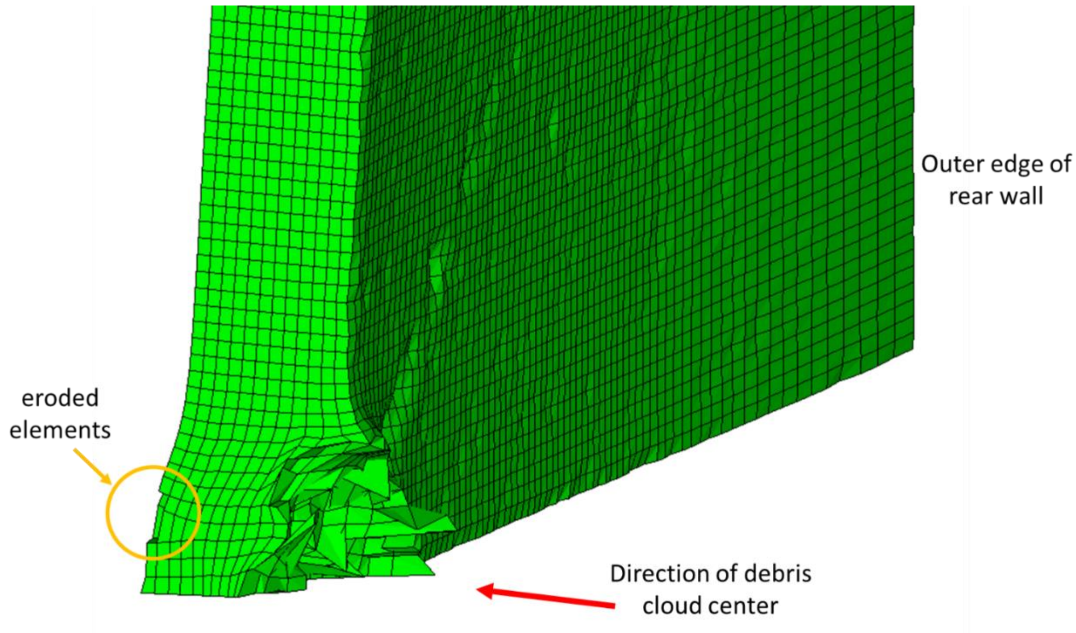

Figure 39. Rear wall with t=2.87mm after impact with cylinder debris cloud displaying the eroded elements at the rear of the rear wall, which was considered as a small amount of spallation.

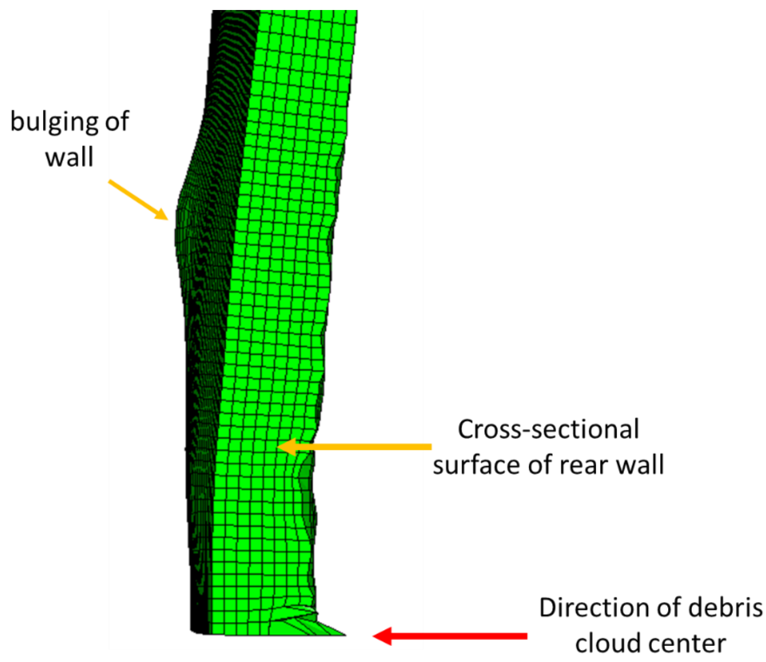

Figure 40. Rear wall with t=2.87mm after impact with spherical debris cloud displaying the bulging of the rear wall, indicating a nearly failed state.

6.9 Improvements in Computational Efficiency

Following the ballistic limit tests, a comparison between the computational costs of the various tests performed were made. The single-core computational costs for the crater-depth model, representative fragment momentum tests, and the ballistic limit tests are summarized in Table 12, with computational cost represented by time spent in calculation. The computational cost summary shows the improvement in computational efficiency with the use of the representative fragment for estimating the crater-depth results for varying bumper thickness over directly applying the crater-depth model to obtain the same results. An individual trial for the ballistic limit tests required less time than one simulation of the crater-depth model. However, ballistic limit tests require several trials to obtain a conclusion, therefore, the effective computational time for ballistic limit testing is several times that of a single trial. The exact number of trials required for the ballistic limit are dependent on various factors. A minimum of two trials is necessary, however, five or six trials are a more realistic estimate.

Table 12. Computational time comparison between the various numerical tests performed in Ansys Autodyn using CPU: 8-core 16-thread Intel Xeon E5-2470 @ 2.3Ghz.

	Approx. single-core computational time
S=15 mm Crater-depth, 6mm	5.8 days
S=100 mm Crater-depth, 6mm	4.8 days
S=150 mm Crater-depth, 6mm	5.5 days
Momentum Test	1.4 days
Ballistic Limit Test	3.9 days per trial 19.6 days per five trials

6.10 Conclusion

The conclusions for this section are as follows:

- The threat of the cylindrical projectiles was found to be dependent on bumper thickness. A minimum thickness for full fragmentation as was found for spherical projectiles was absent for cylindrical projectiles.
- The representative fragment of the debris cloud was considered the primary contributor to the depth of the largest crater. Furthermore, the representative fragment was used to estimate the threat of projectile.
- Using the representative fragment's momentum, the threat of plate-like projectiles were found to linearly decrease with increasing bumper thickness. The threat of rod-like projectiles were found to follow a polynomial-like trend as bumper thickness was increased.
- Using ballistic limits determined numerically, the crater depth metric was found to sufficiently represent the threat of differently shaped projectiles.
- The developed procedure makes it possible to obtain computationally efficient estimates for the equivalent spherical projectile that addresses the requirement for the bumper thickness.
- Method enables the incorporation of MMOD shape variability into the design framework and facilitates the development of MMOD protection that meets the maximum allowable MMOD risk requirement.

7. Rear-Plates Metric Analysis

This section describes the model that used the rear plates intermediary metric. As described previously in section 3.2, the rear plate metric used the discrete number of thin plates perforated as a measure of the threat of a particular projectile. The threat of the projectile was defined as the ability of the projectile to cause failure in the spacecraft shielding. The rear plates model was developed prior to the development of the crater depth model and was used as a preliminary study into the evaluation of projectile threat.

7.1 Model Geometry

Similar to the crater depth model, the rear plates model is based on the Whipple shield previously described in literature review section 2.4. The model consists of the bumper and rear wall followed by a series of thin rear plates (RP) as shown in Figure 41. In the figure, there are only five RP shown but in the simulation there was as many RP as required until the debris cloud could no longer perforate through. The standoff distance between bumper and rear wall was set at S=100 mm, which was found to be common among the ballistic limit tests shown in the MMOD handbook by NASA [1].

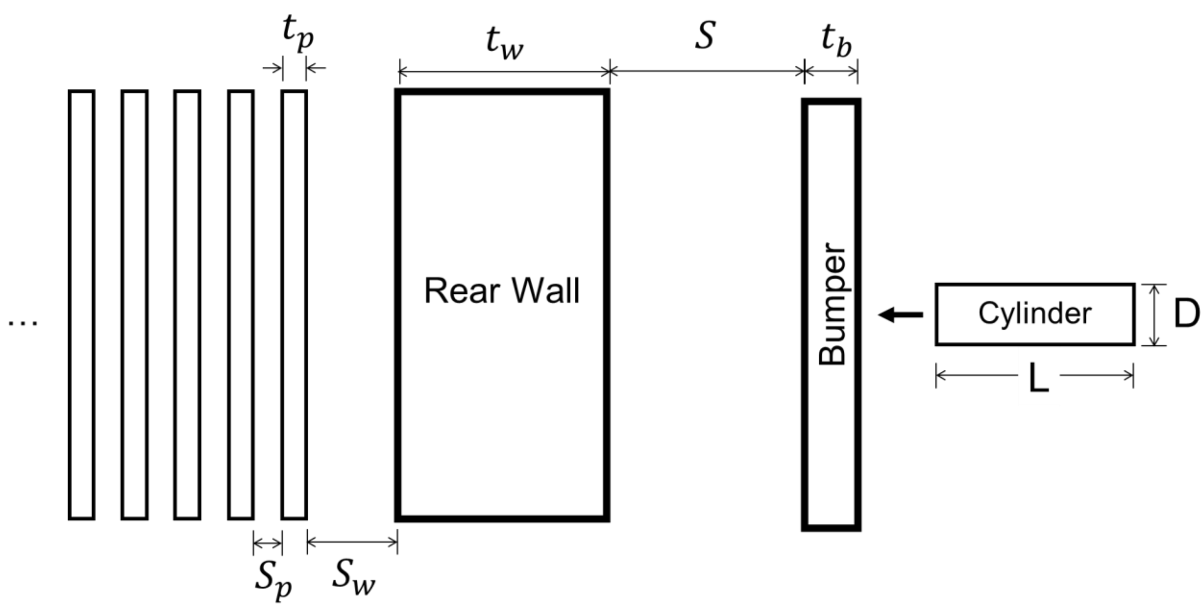

Figure 41. Basic schematic of the rear plates model.

The sizes of the various parts of the model are listed in Table 13. The thickness of the rear wall, t_w, was chosen to sufficiently stop the perforation and spallation caused by a 6 mm spherical projectile moving at 7 km/s. This rear wall thickness was obtained from the NASA design equations previously described in the Whipple Shield literature review of section 2.4. As a result, the number of RP perforated for the 6 mm sphere was set at zero, which was reflected by the results shown in the following subsections. The 6 mm ballistic limit was chosen as the dimensions partly for convenience but also to address the fragmentation issues that were discovered and described in the following results subsection. The distances between the rear wall and the RP, as well as the distances between the RP was arbitrarily set.

Table 13. Geometry of the rear plates model.

L/D	1/3, 2/3, … 6/3
t_b	1.5 mm
S	100 mm
t_w	3.142 mm
S_w	5 mm
t_p	0.5 mm
S_p	5 mm

Similar to the crater depth model for S=15 mm, the rear plates model also incorporated rigid bodies to avoid the contact of the peripheral and non-central regions of the debris cloud. Two rigid bodies were placed just before the rear wall and the first RP, as shown Figure 42. The justification for the implementation of these rigid bodies was identical to their implementation in the crater depth model in section 5.3.3. It was assumed that the perforation through the rear wall and following thin plates were caused primarily by the critical region of the debris cloud located near the central axis of the cloud. This assumption was considered reasonable due to the fragment analysis described previously in section 6.3, which identified the representative fragment as located close to or at the central axis of the debris cloud.

The rear plates model used the same cylindrical projectile shapes as was used in the crater depth metric analysis, which were L/D=1/3, 2/3, … 6/3. Similarly, all projectiles were of mass equal to the 6 mm aluminum sphere, which corresponded to the 6 mm characteristic size chosen due to the fragment distribution literature data, described in more detail in section 3.4.

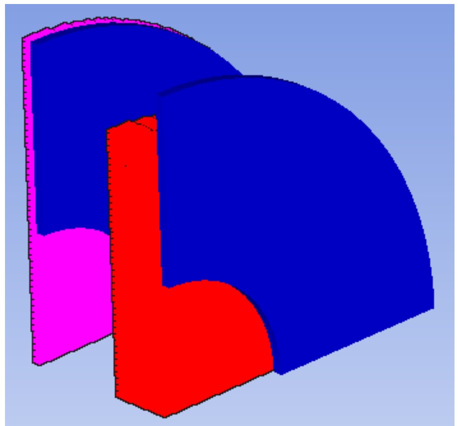

Figure 42. Visualization of the rigid bodies (blue) in front of the rear wall (red) and the first rear plate (pink).

7.2 Model Configuration

All bodies in the rear plates model were defined using the SPH method. The projectile and bumper were SPH, which was the same as with the crater depth model, due to the fragmentation process. For the rear plates model, the rear wall and the following thin rear plates were also fully defined with SPH because they were of finite thickness and were expected to experience a high degree deformation from the perforation process. All bodies were made of Aluminum 6061-T6 and the material model was described previously in section 4. Similar with the crater depth model, the rear plates model used two planes of symmetry.

All bodies used a uniform SPH particle size of 0.125 mm, which corresponded to four particles across the thickness of the RP. No boundary conditions were applied. The initial conditions of the model consisted of the projectile given a velocity of 7 km/s directed normal to the bumper, rear wall and rear plates.

7.3 Consistency in Model Output

The SPH particle size, set at 0.125 mm, was larger than what was used for the crater depth model because the partial-convergence requirements for the rear plates model was considerably less strict. The primary output of the rear plates model was the discrete number of rear plates perforated through. Therefore, the result of model was considered acceptable if the quantity of RP perforated remained consistent as the number of total SPH particles were incrementally increased. The numerical convergence of the whole model was considered unnecessary. As a result, the rigid bodies shown previously in Figure 42 in section 7.1 were included near the rear wall and rear plates to exclude non-central region of the debris cloud.

The testing of the consistency in the output of the rear plates model was performed for two projectile shapes. The first was the 6 mm sphere. Since the geometry of the rear plates model was based on the design equation of the WS for 6 mm sphere, the model was expected to sufficiently stop the perforation and spallation of the projectile. Therefore, the number of SPH was increased until the ballistic limit was reached. Secondly, the consistency in the output was tested using the HVI of cylinder L/D=2/3, where the number of SPH was increased by approximately 30% at each iteration until the output remained constant four times (at four RP perforated). The SPH particle size of 0.125 mm was obtained from the first of the four iterations with the consistent output. Due to the preliminary nature of the development of the rear plates model, this result was considered acceptable. Further study into the proper numerical convergence of the model was neglected due to the inherent issues found from the results of the rear plates model, described in the following sections.

7.4 Results

The rear plates model was used to run several simulations, at least once for each for the cylinders $1/3 \leq L/D \leq 6/3$. The various projectiles were impacted normal against the thin and constant t=1.5 mm thick bumper at 7 km/s. Due to the higher threat expected, all the cylindrical the debris clouds perforated through the rear wall, which was designed for the ballistic limit of the 6 mm sphere according to the WS design equations. The number of RP perforated was counted until the debris cloud was unable to perforate further. The termination of the simulation was determined after 20 microseconds have passed after impact with one of the RP without perforation. Any spallation on the RP was considered the same as one final RP perforated through.

The number of RP perforated through for each cylindrical projectile is shown in Figure 43. As was the case with the results of the crater depth model, the threat of the various cylinders was found to increase as the cylinder shape was changed away from L/D=1 nugget shape. Thus, the trend in cylinder threat was consistent between the two models developed. That is, the result was consistent with the conclusion that the threat of the projectile decreased as the shape became closer to a sphere-like shape, and vice versa. In order to compare the threat between cylinders and projectiles, simulations were also performed with incrementally larger spherical projectiles starting with 6 mm diameter, which was previously determined to stop at the rear wall (zero RP). The results for the spheres are shown in Figure 44. The spherical results displayed a linear relationship between the size of the sphere and the number of RP perforated. This behaviour was consistent with the results of the crater depth metric analysis.

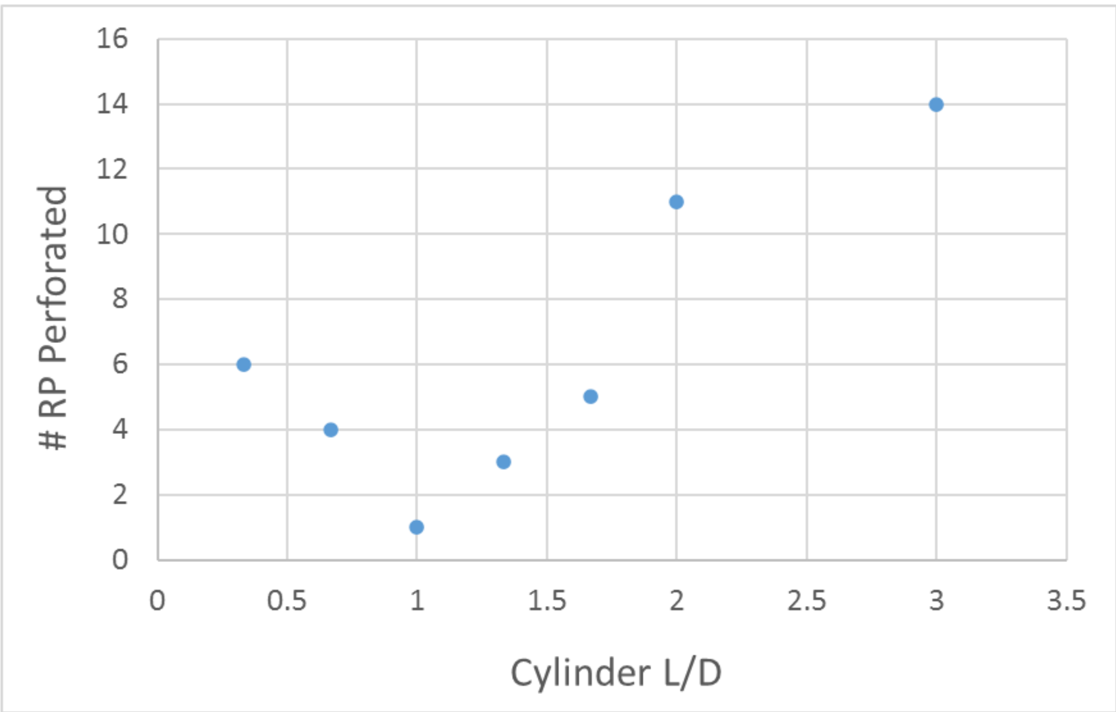

Figure 43. Number of rear plates perforated for various cylinder projectiles.

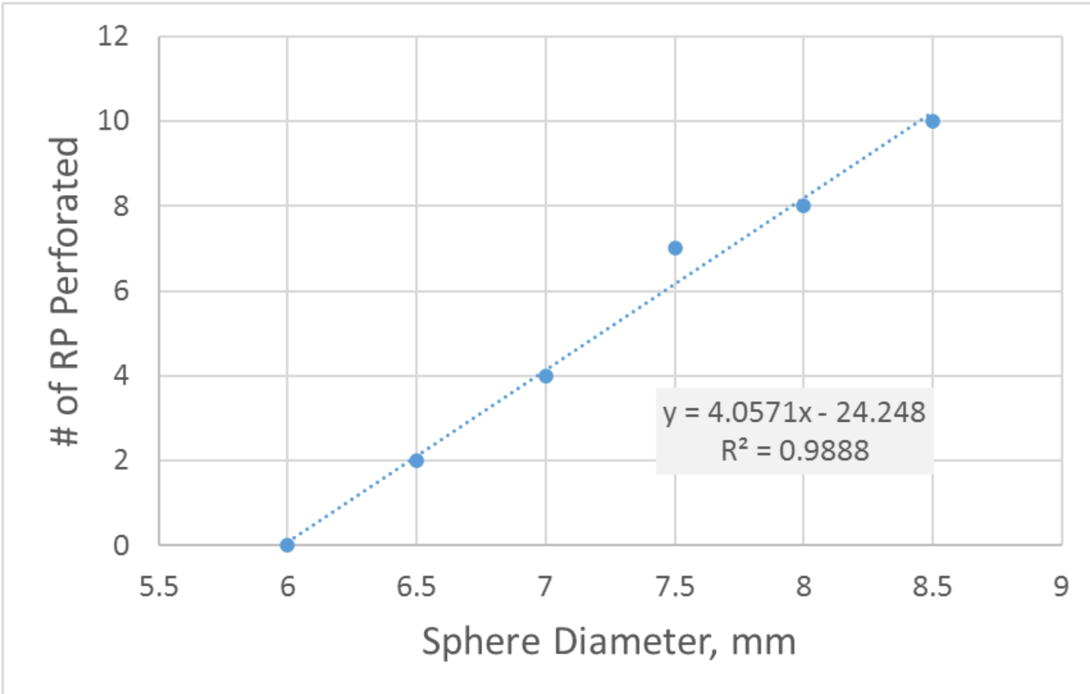

Figure 44. Number of rear plates perforated for increasingly larger spherical projectiles

A linear regression of the spherical results from Figure 44 was used with the cylindrical results of Figure 43 for the creation of the threat-equivalence between the two shapes. The result for the threat-equivalence from the number of rear plates perforated is shown in Figure 45. This relationship was developed to allow cylindrical projectiles to be represented by a sphere of equivalent threat. In this way, spacecraft shielding approaches originally developed for spherical debris can be modified to include protection against cylinder-shaped debris.

A limitation of the threat-equivalence results from Figure 45 was that the number of RP for cylinders was obtained with a constant bumper thickness at t=1.5 mm. However, as previously described in section 6.2 for the crater depth metric results, the threat-equivalence obtained with a constant bumper thickness can be further adjusted to meet the requirements related to bumper thickness. This was because larger spherical projectiles required larger bumper thickness according to literature described previously in section 6.1.

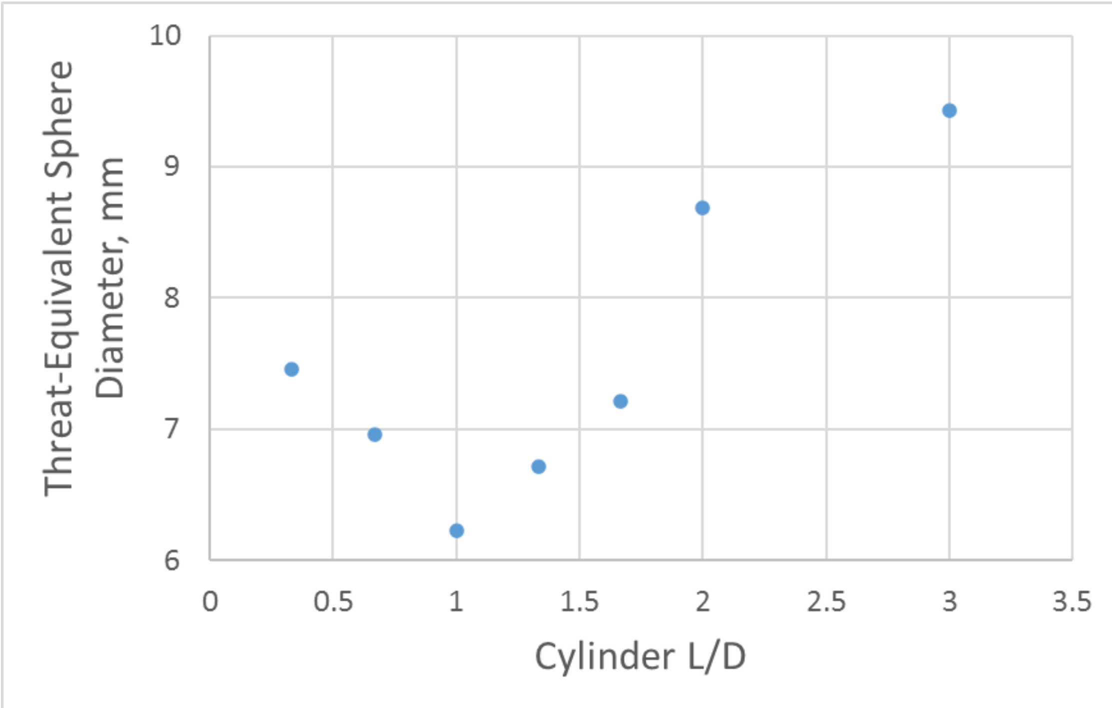

Figure 45. Threat-equivalence between cylinder and spherical projectiles based on number of rear plates perforated.

In the testing of slender rod-like projectiles, an issue was found inherent to the rear plates model. With the testing of cylinder L/D=2 in the rear plates model, the debris cloud was found to contain an unfragmented portion of the projectile located at the rear of the debris cloud. The velocity of the unfragmented portion was not as high as the cloud leading edge, but the mass was several magnitudes greater than what was expected of normal cloud's representative fragment. It was expected that the debris cloud would produce a high threat result and, indeed, the number of RP perforated was nearly double (11) of the second largest result (6). A test was also performed for L/D=3, which resulted in a debris cloud that clearly contained a massive unfragmented portion that corresponded to the rear one-third section of the original projectile. A visualization of the debris cloud for the L/D=3 was shown previously in Figure 21 in section 5.4.1 for the crater depth model. The unexpected result was that the number of RP perforated (14) was not much larger than for the L/D=2 cylinder (11). This observation and the subsequent analysis of the simulation led to the conclusion that the series of thin rear plates was producing additional unintentional fragmentation in the debris cloud, similar to the phenomenon caused by the bumper but reduced in magnitude. The additional fragmentation reduced the danger posed by the debris cloud from the further break-up of the fragments into individually less dangerous and smaller fragments. As a result, the number of RP perforated for the L/D=3 underestimated the actual threat the same projectile posed to a rear wall unobstructed by a series of thin plates, such as the WS.

The conclusion for the L/D=3 was hypothesized to apply also to the other cylinder shapes to a lesser degree. The excess energy and velocity of the debris cloud after perforating the relatively thick rear wall was sufficient for additional fragmentation despite the rear wall designed for the ballistic limit of the 6 mm sphere. It was concluded that the setup of the rear plates model underestimated the amount the amount of energy in the debris cloud after HVI with the rear wall. Therefore, as a consequence of the additional fragmentation, the rear plates model was thought to underestimate the threat of higher threat projectiles. That is, the more dangerous the projectile, the more error in the output of the rear plates model. With the development of the crater depth (CD) model, the threat-equivalence of the two models were compared and shown in Figure 46. Contrasted to the crater depth results, it was clear that the rear plates model underestimated the threat of nearly all the cylinder projectiles.

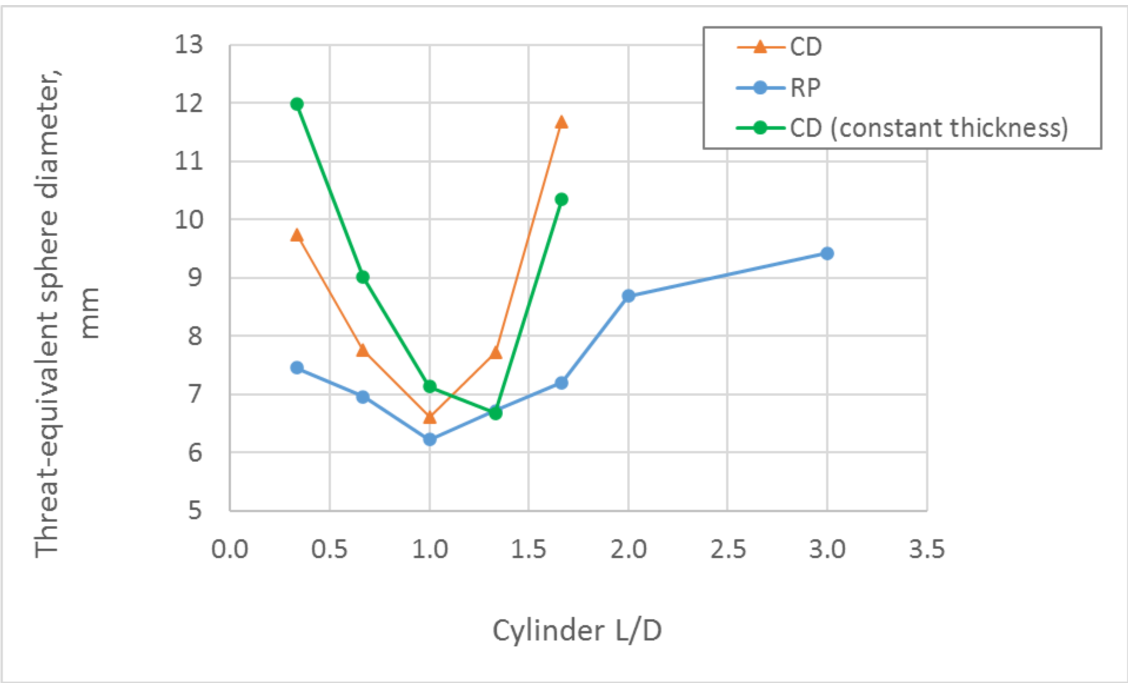

Figure 46. Threat-equivalence results for the crater depth model (orange and green) and the rear plates model (blue) for S=100 mm.

7.5 Conclusion

The conclusion from the rear plates model are as follows:

- From the rear plates model, the overall trend in the threat of cylinder projectiles as the shape was changed was found to be similar to the trend observed for the crater depth model: the threat increased as the shape was changed further from L/D=1.
- The rear plates model significantly underestimated the threat of projectiles due to additional fragmentation as a consequence of the series of thin rear plates. Future work is required in the adjustment of the model.

8. Thesis Conclusions

8.1 Conclusions

1. Spacecraft shielding is necessary to protect against non-trackable debris, however, most current shielding designs are based only on spherical projectiles. Traditional methods for investigating projectile shape in HVI are resource intensive, therefore study of a large range of different projectiles is difficult.
2. The use of an intermediary metric to represent the threat of projectile expedites the process in evaluating the potential for the differently shaped projectiles to cause failure in spacecraft shielding. This was demonstrated with a numerical method developed to measure only the depth of the largest crater produced by the debris cloud of differently shaped cylindrical projectiles. Using ballistic limits determined numerically, the crater depth intermediary metric was found to sufficiently represent the ability of projectiles to perforate the rear wall of Whipple Shields.
3. A relationship between the threat-equivalence of spherical and cylindrical projectiles was established, which represented the potential of the particular projectile to cause failure in spacecraft shielding. The threat of a cylinder projectile in normal impact increased as the projectile became more like a flat thin-plate or as the projectile became more like a slender straight-rod.

4. The threat of the cylindrical projectile relative to the spherical projectile was found to increase with increasing standoff distance, up to a distance of 100 mm for a cylinder of a mass equal to a 6 mm sphere impacting normal at 7 km/s.
5. The threat of plate-like cylindrical projectiles was found to decrease linearly with an increase in bumper thickness. In contrast, the threat of rod-like projectiles was found to change in a polynomial-like fashion, increasing or decreasing depending on the thickness of the bumper.

8.2 Contribution to Knowledge

1. Introduced a different type of methodology in the evaluation of the danger posed by differently shaped projectiles on spacecraft equipped with an MMOD bumper.
2. Demonstrated the methodology toward the creation of relationships between cylinder projectiles and their threat-equivalent spherical projectiles.
3. Investigated the effect of bumper thickness and standoff distance on the threat of differently shaped cylinder projectiles in HVI, which have not yet been performed in detail.
4. The developed methodology enables the incorporation of MMOD shape variability and facilitates the development of MMOD protection that adheres to the requirement for maximum permissible risk.

8.3 Limitations and Future Work

The main limitation of thesis is that all results were obtained entirely with numerical simulation. The aluminum material model was obtained and validated by an external author and the debris clouds produced by the cylindrical projectiles were partially validated with experimental literature data. However, the exact conditions and configuration of the numerical models presented in the thesis have not been replicated in physical experiment, therefore, the results themselves have not been validated and cannot be guaranteed. The validation of the results with physical experimental is a potential avenue for future work and is a necessary step to ensure the reliability of the results and conclusions.

Another main limitation of the thesis work is in the narrowness of the scope with regards to the impact parameters. Literature review into the distribution of debris have shown that debris fragment exists in large variety of shapes beyond what can be possibly modelled with a cylinder, which was the only non-spherical shape investigated in the thesis. Previous literature attempts with the ellipsoids by Hiermaier et al. are similar in nature to the cylinders allowing for the contraction of the shape into a thin flat object or the elongation to a long slender object [21]. However, irregular shapes, such as the "bent rod," were found to be common and are more difficult to model. In addition, the impact angle and the inclination of the projectile in the thesis was limited to normal impact with zero yaw or pitch, which is an unrealistic set of impact conditions in the majority of cases. Zero inclination was chosen primarily because this condition provided the closest match between the numerical model and the literature data for debris clouds, shown previously in section 4.2. Conversely, the normal impact was used primarily for practicality because implementation of non-normal impact removed one plane of symmetry, doubling the computational costs. As potential future work, the extension of the results obtained in the thesis for various other impact parameters such as different shapes and different impact angles in would provide a more complete understanding of the threat of non-spherical projectiles and allow for the easier adjustment of spacecraft protection against more realistic debris shapes.

9. References

[1] Handbook for limiting orbital debris, NASA, 2008.

[2] H. Klinkrad, "Space Debris Models and Risk Analysis," 2006.

[3] E. S. Agency, "Space debris by the numbers," 2022.

[4] Committee for the Assessment of NASA's Orbital Debris Programs, "Limiting Future Collision Risk to Spacecraft: An Assessment of NASA's Meteoroid and Orbital Debris Programs", 2011.

[5] N. JS, *Chinese Anti-satellite Test Creates Most Severe Orbital Debris Cloud in History*, The Orbital Debris Quarterly News, 2007.

[6] N. Johnson, "Monitoring and Controlling Debris in Space," Scientific American, 1998.

[7] NASA, "The intentional destruction of Cosmos 1408," *Orbital Debris Quarterly News,* vol. 26, no. 1, p. 2, 2022.

[8] Liou, J.C. and N.L. Johnson, "Risks in Space from Orbiting Debris," Science, Volume 311, pp. 340-341, 20 January 2006..

[9] J.E. Williamsen, W.P. Schonberg, and A.B. Jenkin, "On the effect of considering more realistic particle shape and mass parameters in MMOD risk assessments," Advances in Space in Research 47:1006-1019, 2011.

[10] R.H. Morrisson, "Investigation of Projectile Shape Effects in Hypervelocity Impact of a Double-Sheet Structure", NASA TN D-6944, NASA, Washington, D.C., 1972.

[11] Piekutowski, "Debris clouds generated by hypervelocity impact of cylindrical projectiles with thin aluminum plates," *Journal of Impact Engineering,* vol. 5, pp. 509-518, 1987.

[12] A. Jones, "Modelling of Hypervelocity Impact on Foam-Core Sandwich Panel with Enhanced Capability for Orbital Debris Protection" M.Sc thesis, University of Manitoba, Canada, 2018..

[13] A. Tate, "Further results in the theory of long rod penetration," *Journal of mechanics and physic of solids,* vol. 17, pp. 141-150, 1969.

[14] V. Holer and A. J. Stilp, "Hypervelocity impact of rod projectiles with L/D from 1 to 32," *International journal of impact engineering,* vol. 5, pp. 323-331, 1987.

[15] E. Christiansen, K. Nagy, D. Lear, T. Prior, "Space Station MMOD Shielding," Acta Astronautica 65, 921-929, 2009.

[16] S. Ryan, E. Christiansen, "Hypervelocity impact testing of advanced materials and structures for micrometeoroid and orbital debris shielding," Acta Astronautica 83, 213-231, 2012.

[17] P. H. Krisko, M. Horstman and M. L. Fudge, "SOCIT4 Collisional-breakup test data analysis: with shape and materials characterization," *Advances in space research,* vol. 41, no. 7, pp. 1138-1146, 2007.

[18] H. Cowardin, J. Mostetler, J. Murray, J. Reyes and C. Cruz, "Optical characterization of debrisat fragments in support of orbital debris environmental models," *Journal of the astronautical sciences,* vol. 68, pp. 1186-1205, 2021.

[19] A. Piekutowski, "A simple dynamic model for the formation of debris clouds," *International journal of impact engineering,* vol. 10, pp. 453-471, 1990.

[20] A. Piekutowski, "Debris clouds produced by the hypervelocity impact of nonspherical projectiles," *International journal of impact engineering,* vol. 26, pp. 613-624, 2001.

[21] S. Hiermaier and F. Schafer, "Simulation of ellipsoidal projectile impact on whipple shield," *International journal of impact engineering,* vol. 29, pp. 333-343, 2003.

[22] M. Carrasquilla and J. Miller, "Shape effect analysis of aluminum projectile impact on whipple shields," *Procedia Engineering,* pp. 308-314, 2017.

[23] B. Corbett, "Numerical simulations of target hole diameters for hypervelocity impacts into elevated and room temperature bumpers," *International journal of impact engineering,* vol. 33, p. 431440, 2006.

[24] A. Cherniaev, *Design and analysis of orbital debris protection for spacecraft composite pressure vessels,* Winnipeg: University of Manitoba, 2016.

[25] G. Kay, "Failure modeling of Titanium 6Al-4V and Aluminum 2024-T3 with the Johnson-Cook Material Model," *Scientific and technical aerospace reports, vol. 42,* 2004.

[26] E. Christiansen, "Handbook for designing MMOD protection," NASA, 2009.

[27] A. Piekutowski, "Characteristics of debris clouds produced by hypervelocity impact of aluminum spheres with thin aluminum plates," *International journal of impact engineering,* vol. 14, pp. 573-586, 1993.

[28] E. Christiansen, "Enhanced meteoroid and orbitaldebris shielding," International Journal of Impact Engineering, Vol. 17, pg. 217-228, 1995.

[29] A. Cherniaev and I. Telichev, "Weight-Efficiency of Conventional Shielding Systems in Protecting Unmanned Spacecraft from Orbital Debris," *Journal of Spacecraft and Rockets,* vol. 54, pp. pg 75-89, , 2017.

[30] S. Ryan, E. Christiansen, D. Lear, “Development of the Next Generation of Meteoroid and Orbital Debris Shields,” NASA, 2019.

[31] B. Cour-Palais and J. Crews, “A Multi-Shock Concept for Spacecraft Shielding,” International Journal of Impact Engineering, no. 10, pp. 95-106, 1993.

[32] S. Ryan, T. Hedman, E. Christiansen, "Honeycomb vs foam: evaluating potential upgrades to ISS module shielding," Acta Astronautica 67, pg 818-825, 2010.

[33] D.W. Jex, A.M. Miller, C.A. MacKay, The characteristics of penetration for a double-sheet structure with honeycomb, NASA Marshall Space Flight Center, Huntsville, NASA TM X-53974, 1970.

[34] S. Ryan, F.K. Schaefer, R. Destefanis, M. Lambert, A ballistic limit equation for hypervelocity impacts on CFRP/Al HC satellite structures, Advances in Space Research 41, pg 1152–1166, 2008.

[35] S. Ryan, E. Ordonez, E. Christiansen, D. Lear, "Hypervelocity Impact Performance of Open Cell Foam Core", NASA, 2010.

[36] J. Yasensky, E.L. Christiansen, T. Prior, "Hypervelocity impact evaluation of metal foam core sandwich structures," GeoControl Systems, Houston, NASA TP-2008-214776, 2008.

10. Appendix: Advanced Spacecraft Shielding Types

10.1 Stuffed Whipple shield

Volume requirements for spacecraft imposed limits on standoffs of WS. Sub-optimum standoff distances resulted in significant reductions in protection performance. Therefore, the WS was improved by including an additional bumper to further fragment the projectile and raise the temperature causing further melting or vaporization [2] [28]. The 1995 NASA SWS, shown in Figure 47, uses a combination of materials for the inner bumper: Kevlar™ and Nextel ™ with multi-layer insulation (MLI).

The combination of materials in the intermediate layer provides greater HVI protection than an alternative monolithic second-bumper. Normally, a metal second-bumper would also contribute to the debris cloud. However, the fabrics in SWS provide fragments that are much less damaging. Compared to a solid aluminum second-bumper, the Nextel™ ceramic cloth provides better fragmentation of the projectile and the Kevlar™ is better at slowing expansion speed of debris cloud. In general, the SWS provides protection against 50% to 300% (depending on impact parameters) heavier projectiles compared to an all-aluminum double-bumper WS of equivalent mass. Furthermore, compared to regular WS, a SWS is 2.5 times lighter for short 11cm standoff, 1.35g Al projectile at 7km/s (normal) [28].

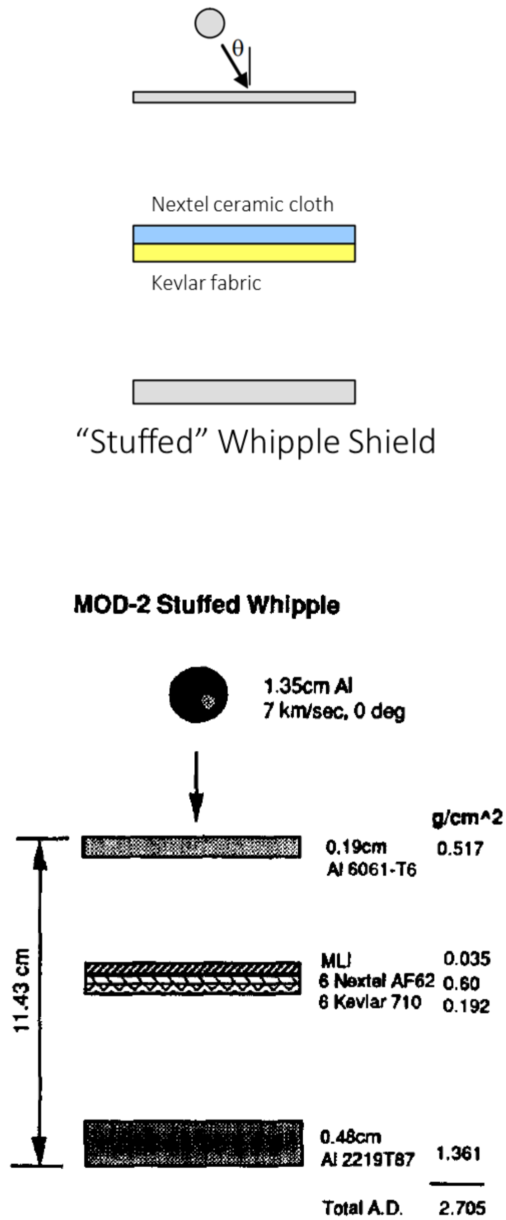

Figure 47. Example of 1995 NASA SWS configuration [28].

When standoff is not limited, WS still provides a slightly higher mass-efficiency. A study by A. Cherniaev and I. Telichev in 2017 compared areal densities of equivalent WS, SWS and two multifunctional panels described in later sections [29]. The results of the study are shown in Figure 48.

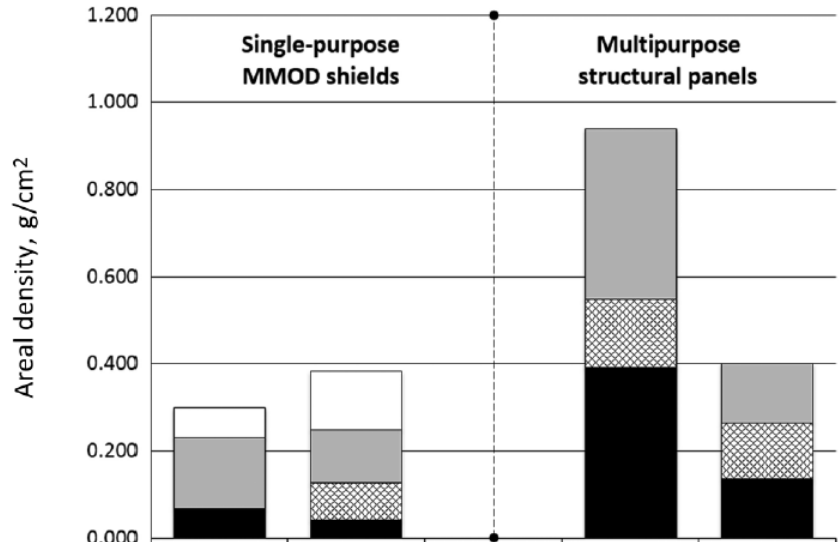

	WS	SWS		HCSP	FCSP
□ Nonballistic.weight	0.069	0.134		0.000	0.000
▒ Rear wall	0.162	0.122		0.392	0.135
⊠ Core or stuffing	0.000	0.087		0.156	0.130
■ Front wall	0.068	0.041		0.392	0.135

Figure 48. Areal densities of different equivalent shielding types [29].

10.2 Multi-Shock shield

Multi-shock shields (MSS) are similar to SWS in that they use intermediate layers. However, the MSS uses many more intermediate layers than the SWS. The MSS example shown in Figure 5 use Nextel™ fabrics but the material to use for the layers can be different depending on the design requirements. The MSS offers significant mass-efficiency compared to the SWS or WS, as much as 30% over equivalent WS [30]. However, the MSS has large standoff requirements and may not be suitable for some spacecraft [31]. One additional benefit of MSS is, when using fabrics, there are significantly less ejecta (or ricochet) fragments, which greatly reduce generation of extra debris with MMOD collision [26].

10.3 Honeycomb Sandwich Panel

Some spacecraft may not spend too much time in orbit, therefore the shielding requirements may not be as high compared to the ISS. In these situations, multifunctional shielding is used as an alternative to single-purpose shields like WS. These shields are part of the spacecraft structure and consist of two facesheets that “sandwich” a specific type of inner structure. An early design is the honeycomb sandwich panel (HCSP), which uses honeycomb-shaped cells between the facesheets that are oriented normal to the surface of the sheets. Multifunctional HCSP are in use as MMOD shielding for some ISS modules [32].

Studies in 1970 by D. Jex et al. in [33] found that HCSP were a good alternative to conventional single-purpose shields under strict size and weight constraints. However, it was also found that the honeycomb cells acted to restrict the passage of the debris cloud, a phenomena referred to as “channeling,” shown more clearly in Figure 49. The studies concluded that channeling detrimental effects were overcompensated by secondary impacts with the debris cloud and the honeycomb. However, the presence of honeycomb reduced shielding performance, compared to same-standoff WS, by as much as 46% for normal impacts, with less reduction as impact obliquity increased [34]. This degradation of performance can be more clearly seen in Figure 50.

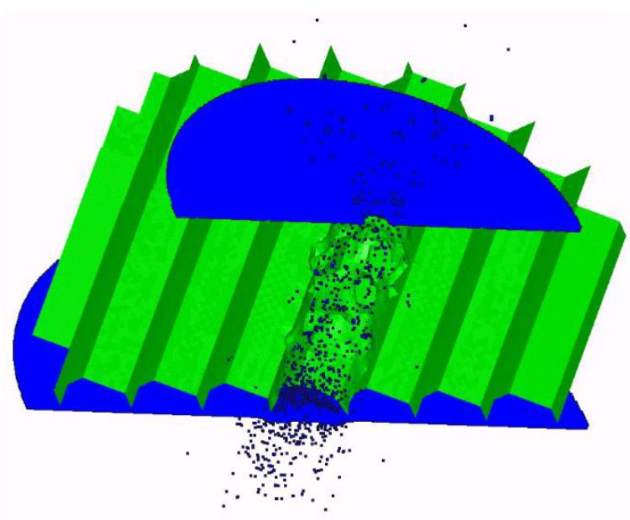

Figure 49. Channeling of fragments between honeycomb cells (green) [12].

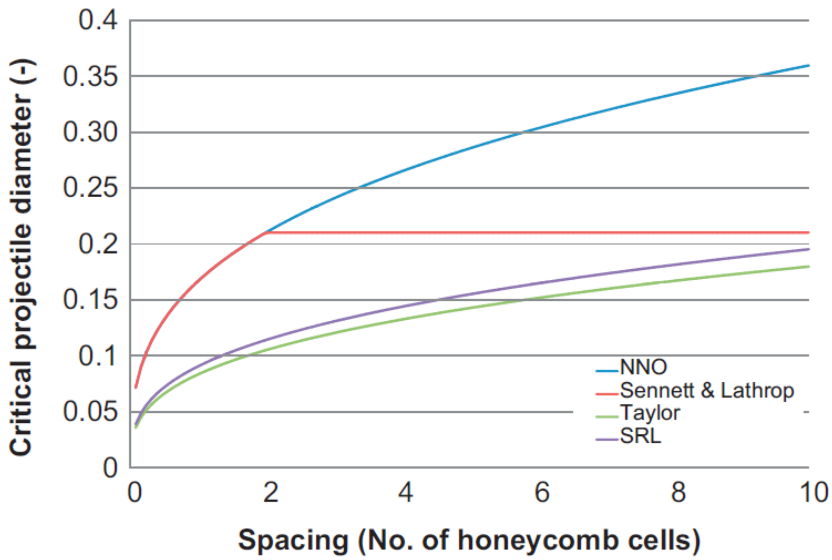

Figure 50. Critical (penetrating) projectile diameter for HCSP performed by different sources; new non-optimum (NNO) refers to a WS configuration for sandwich panel (no honeycomb) [32].

10.4 Open-cell Foam Core Sandwich Panel

Foam core sandwich panels (FCSP) are multifunctional shielding that serve as an alternative to HCSP. Instead of honeycomb between the front and rear facesheets, the FCSP uses a metallic foam to reduce projectile penetrative ability. However, FCSP cannot provide the same level of protection as single-purpose shields for a given weight, they still provide improved protection compared to HCSP when there are strict size requirements [35].

A study in 2012 by S. Ryan et al. in [16] found that metallic foam was the most effective type material for use as an inner bumper in a double-bumper WS using a combination of criteria (weight, damage resistance, and BLE). This effectiveness translates into sandwich panel configuration. A beneficial aspect of the foam are its thermal effects on debris cloud fragments. For WS, complete melting of fragments are predicted at approximately 8km/s. However, FCSP produce complete fragment melting by velocities as low as 4km/s [30]. As described previously, liquid fragments produce less damage onto the rear wall (or facesheet).

The shielding performance of FCSP were studied by [32], [36] and [35]. The BLE for a specific configuration of FCSP compared to other shielding is shown in Figure 51. Furthermore, weight efficiencies of FCSP compared to the HCSP was shown previously in Figure 48 [29].

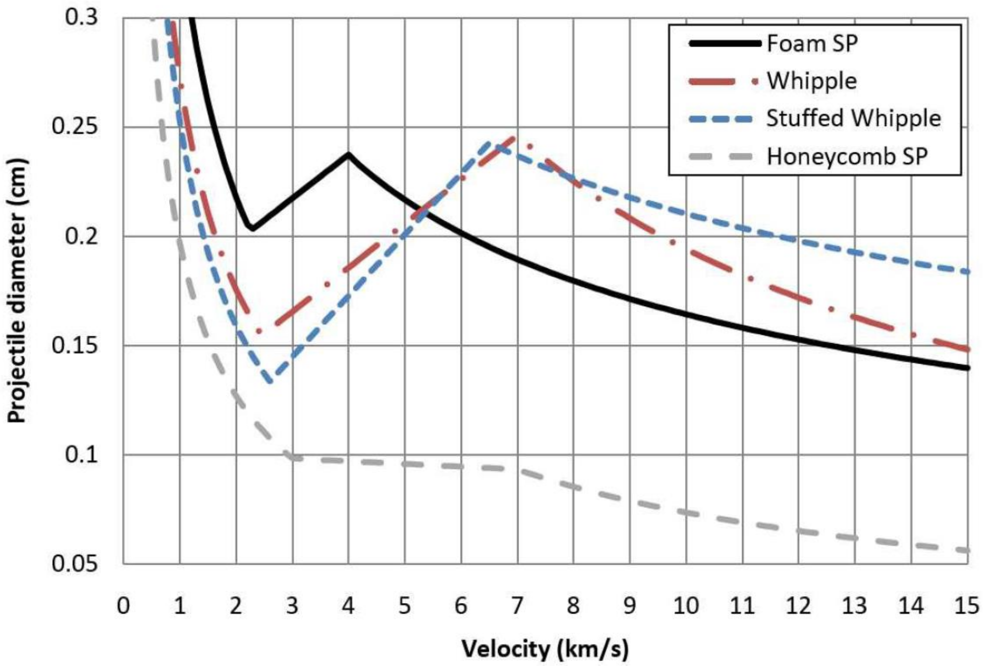

Figure 51. Performance of FCSP compared to other shielding types [35].